Computer Vision Methods for Urinary Tract Infection Diagnostics

by

Rafael Iriya

A Thesis Presented in Partial Fulfillment
of the Requirements for the Degree
Doctor of Philosophy

Approved April 2020 by the
Graduate Supervisory Committee:

Pavan Turaga, Chair
Thomas Grys
Yanchao Zhang
Shaopeng Wang

ARIZONA STATE UNIVERSITY

May 2020

ABSTRACT

Antibiotic resistance is a very important issue that threatens mankind. As bacteria are becoming resistant to multiple antibiotics, many common antibiotics will soon become ineffective. The inefficiency of current methods for diagnostics is an important cause of antibiotic resistance, since due to their relative slowness, treatment plans are often based on physician's experience rather than on test results, having a high chance of being inaccurate or not optimal. This leads to a need of faster, point-of-care (POC) methods, which can provide results in a few hours. Motivated by recent advances on computer vision methods, three projects have been developed for bacteria identification and antibiotic susceptibility tests (AST), with the goal of speeding up the diagnostics process. The first two projects focus on obtaining features from optical microscopy such as bacteria shape and motion patterns to distinguish active and inactive cells. The results show their potential as novel methods for AST, being able to obtain results within a window of 30 min to 3 hours, a much faster time frame than the gold standard approach based on cell culture, which takes at least half a day to be completed. The last project focus on the identification task, combining large volume light scattering microscopy (LVM) and deep learning to distinguish bacteria from urine particles. The developed setup is suitable for point-of-care applications, as a large volume can be viewed at a time, avoiding the need for cell culturing or enrichment. This is a significant gain compared to cell culturing methods. The accuracy performance of the deep learning system is higher than chance and outperforms a traditional machine learning system by up to 20%.

DEDICATION

This dissertation is dedicated to my family, Decio Iriya, Edna Iriya and Daniel Iriya, and my partner Ratrapee Techawitthayachinda for moral and financial support throughout six years of hard work. This could never have been done without any of them. Above all, these work was only possible thanks to my mentor Dr. Nongjian Tao, who unfortunately has had his mission terminated early. Dr Tao was a brilliant person, a true leader, and besides all the technical insights, guidance and shaping my way of thinking, has taught me a lot about what it means to be a PhD and what technical and soft skills are necessary for it. Thank you Dr. Tao, you will be forever remembered.

ACKNOWLEDGMENTS

I'd like to thank the help of Dr. Shaopeng Wang, Dr. Shelley Haydel, all members of the committee (Thomas Grys, Pavan Turaga, Yanchao Zhang), current and past student employees and post-doctoral researchers of the Biodesign Institute who contributed with intelligent discussions. I also acknowledge the Gordon and Betty Moore Foundation and the National Institutes of Health R01AI138993 for financial support.

TABLE OF CONTENTS

Page

LIST OF TABLES vii

LIST OF FIGURES ix

LIST OF ABBREVIATIONS xvii

LIST OF SYMBOLS xix

CHAPTER

1 INTRODUCTION 1

1.1 Background 1

1.1.1 Relevance 1

1.1.2 Diagnostics Inefficiency 4

1.2 Current Methods 6

1.2.1 Identification Methods 6

1.2.2 *AST* Methods 10

1.3 Purpose of This Work 13

2 BACTERIAL MEMBRANE MORPHOLOGICAL DEFORMATIONS ASSESSMENT 15

2.1 Introduction 15

2.2 Method Description 16

2.2.1 Overview 16

2.2.2 Differential Detection Algorithm 17

2.2.3 Materials 20

2.3 Discussion and Results 23

2.3.1 Detection Limit 23

2.3.2 Polymyxin B Results 25

2.3.3 Ampicillin Results 29

CHAPTER Page

2.4 Conclusion 32
3 ANTIBIOTICS SUSCEPTIBILITY TESTS BASED ON BACTERIAL MOTION PATTERNS 33
3.1 Introduction 33
3.2 Discussion and Results 35
3.2.1 Image Processing and Deep Learning Algorithms 35
3.2.2 Image Segmentation and Cell Motion Pattern Determination 37
3.2.3 Overview of $LSTM$ Algorithm and Experimental Setup 37
3.2.4 Optical $LSTM$ AST 41
3.3 Experimental Setup 42
3.4 Materials and Methods 44
3.4.1 Materials 44
3.4.2 Antibiotics Preparation 45
3.4.3 Bacteria Cultivation and Preparation 45
3.4.4 Optical $LSTM$ AST 46
3.4.5 Modified Broth Macrodilution AST 46
3.4.6 Growth Curves and MIC Determination 47
3.5 ALGORITHMS 47
3.5.1 Segmentation 47
3.5.2 Cell Tracking 54
3.5.3 Machine Learning 58
3.6 Conclusion 60
4 DEEP LEARNING LARGE VOLUME MICROSCOPY BACTERIAL IDENTIFICATION 62

CHAPTER Page

4.1 Introduction 62
4.2 Discussion 64
4.2.1 LVM 64
4.2.2 Algorithm 65
4.2.3 Results 75
4.3 Materials and Methods 84
4.3.1 LVM Imaging 84
4.3.2 Sample Preparation 86
4.3.3 Data Processing 87
4.3.4 Deep Learning 87
4.4 Conclusion 87
5 CONCLUSION 89
REFERENCES 90
APPENDIX
A STATISTICAL ANALYSIS OF PMB RESULTS FOR THE BACTERIAL MEMBRANE MORPHOLOGICAL DEFORMATIONS ASSESSMENT 99
B PERMISSION TO USE PREVIOUSLY PUBLISHED CONTENT 102
BIOGRAPHICAL SKETCH 104

LIST OF TABLES

Table Page

3.1 Comparison of the Optical $LSTM$ Experimental AST with Modified Broth Macrodilution AST and $CLSI$ AST Interpretive Standards..... 37

3.2 $LSTM$ Learning Results for Different Antibiotics..... 42

3.3 Comparison of Different Methods for Estimating the Next Cell Position From a Sequence of Previous Positions, Showing the Mean Squared Error (MSE) and Maximum Error. Results Show Better Results for $LSTM$ with Independent X and Y with Different Distributions..... 61

4.2 Hand-engineered Features Tested for the Traditional Machine Learning Approach..... 73

4.3 Dataset for E. coli vs. Beads Classification, Containing Data from 4 Days, Where Each Day Was Once Left Out of Training and Used as Validation (in This Example Day 1 Was Used for Validation). Day 4 Was Used as Test..... 76

4.4 Datasets for E. coli vs. Urine Classification. a) Dataset 1 Containing Data from a Single Day Where One Replicate Was Used for Validation and a Different Sample Was Used for Test. b) Dataset 2 Containing Data from a Single day Where Sample 1 Was Used for Validation and a Different Day Was Used for Test. c) Dataset 3 Containing Data from 7 Days, Where Sample 1 from Each Day Was Used for Validation and a Different Day Was Used for Test..... 78

4.5 Accuracy Performance of E. coli vs. 1 µm Polystyrene Beads Classification. The $CNNFA$ Method Shows a 20% Validation Accuracy Increase Compared to the SVM Method..... 79

Table Page

4.6 Accuracy Performance of E. coli vs. Urine Classification Using the $CNNFA$ Method for the 3 Datasets. For Dataset 3, the Numbers Marked with "*" Show the Results Using the Same Validation Data from Dataset 2, for Comparison. 79

4.7 Comparison of SVM, $CNN\text{-}LSTM$ and $CNNFA$ on Dataset 3. The $CNNFA$ Method Shows a 13% Validation Accuracy Increase Compared to the SVM Method, and Both are Much More Accurate than the $CNN\text{-}LSTM$ Method. 80

4.8 Results of Training the Model with a Default Setup Configuration and Testing Using Different Configurations. Changing the Camera Position on the X Plane (Focus) and the Digital Field of View Significantly Affect the Results. 85

LIST OF FIGURES

Figure Page

1.1 Expected Number of Deaths per Year Around the World by 2050. Source - (CDC (2013)) 2

1.2 Example of Resistance Spread. Source - (CDC (2013)) 3

1.3 a) Current Workflow Typically Taking 3 Days to Complete. b) Desired Workflow, Where Results Are Given Right Away at *POC*. 5

2.1 Nanometer-scale Optical Tracking of Bacterial Cell Deformation. a) Bacterial Cells (E. coli O157:H7) Are Imaged by an Optical Microscope and Their Responses to Antibiotics Are Recorded and Analyzed. Scale Bar: 2 µm. b) Antibiotic-induced Bacterial Membrane Deformation (Shape, Length and Width) Described by Displacement Vectors (Black Arrows). Scale Bar: 200 nm. Source - (Iriya et al. (2017)) 16

2.2 Principle and Calibration of the Nanometer-scale Optical Tracking Method. a) A *ROI* at the Cell Edge Is Selected (Blue-red Rectangle) and Divided into Two Halves (Blue and Red) with Optical Intensities Denoted by I_1 and I_2, Respectively. To Calibrate the Method, the *ROI* Is Shifted (Orthogonal to the Cell Edge) by Known Number of Pixels, and Differential Intensity Is Determined. Scale Bar: 200 nm. b) Differential Intensity vs. Pixel Shift. 1 Pixel (Without Interpolation) = 75 nm. Source - (Iriya et al. (2017)). 19

2.3 Schematic for the Drug Perfusion System. As *PBS* or *PMB* Was Injected into The Well, the Suction Pump Concomitantly Removed Excess Liquid from the Well, Thereby Maintaining a Constant Solution Volume. Source - (Iriya et al. (2017)). 22

2.4 Length Change Results for Noise Analysis. a) A Dust Spot in the Camera Was Selected to Assess the Noise of the Algorithm Without External Factors. The Signal Was Pure Noise with Standard Deviation $\sigma = 1.66$ nm. b) A Silicon Bead of 1 µm Was Placed on the Chip Surface. The Silicon Bead Showed Some Small Fluctuations and Long-term Noise, Caused by External Factors, such as Small Focus Changes due to Instabilities of the Microscope Stage. The Short-term Noise for a Window of 10 s Showed $\sigma = 3$ nm. The Limit of Detection Was Approximately $3\sigma = 9$ nm. Scale Bar: 200 nm. Source - (Iriya et al. (2017)). 24

2.5 Length Change for a Silicon Bead when Submitted to a 50 mHz and 500 nm Peak-to-Peak Modulation of the Stage Position in the Z Direction (Vertical), Creating Controlled Focus Changes. Source - (Iriya et al. (2017)). 25

2.6 a) Cell Length Change of E. coli O157:H7 Exposed to PMB (0.5 µg / mL) (Red Line) Compared to PBS (Blue Line) over Time. The Arrow Indicates the Initial Expansion Shortly After Antibiotic Introduction. b) Examples of ROIs and the Corresponding Displacement Vectors for the ROIs. Length Changes Were Determined by Summing the Two Opposite Vectors of the Red/Blue ROIs, and Width Changes Were Determined by Summing the Opposite Vectors of the Green/Yellow ROIs. Scale Bar: 200 nm. Source - (Iriya et al. (2017)). 26

Figure Page

2.7 Cell Length (Blue) and Width (Red) Changes for Three E. coli O157:H7 Cells. a-c) Three Different Cells Incubated in PBS Buffer Only. d-f) Three Different Cells Exposed to PMB (0.5 µg / mL). The Vertical Line in Each Plot at 2 Min Marked the Introduction of PMB. The Optical Images of Each Cell at the End of the Experiment Are Shown at the Bottom of Each Response Plot (Scale Bar: 500 nm). Source - (Iriya et al. (2017)). 28

2.8 Membrane Deformation of a $UPEC$ Cell Exposed to Ampicillin (1 mg / mL). Scale Bar: 200 nm. Source - (Iriya et al. (2017)). 29

2.9 Displacement Measurements of $UPEC$ Cells Exposed to Ampicillin (1 mg / mL). Displacement Vectors (a, c, e) and Corresponding Cell Plots (b, d, f) Are Shown for Different Regions of Different Cells. The Bulge Region is Shown with Magenta Vectors. The Circled Regions (b, d, f) Indicate the Bulge Membrane Deformation While the Arrows Indicate Cell Lysis. Scale Bar 200: nm. Source - (Iriya et al. (2017)). 31

Figure Page

3.1 a) Single Bacterial Cells Are Imaged in Urine in a Microfluidic Channel Using Phase Contrast Microscopy. The Cells are Revealed Either as Bright or Dark Spots, Depending on Their Relative Positions in the Focal Plane (Each Cell is Marked with a Red Circle). b) Image Sequence Over Time (2 s) Shown in Panel (a) Is Fed into an Algorithm Comprising Two Parts: Image Processing and Deep Learning. The Former Includes Segmentation and Tracking Algorithms to Obtain Individual Bacterial Cell Trajectories (Motion Pattern). The Latter Processes the Trajectories with a Deep Learning Algorithm to Determine if a Cell is Active and Inactive and Records the Number of Active and Inactive Cells. c) *AST* Results Are Generated From the Number of Active Cells Obtained Using the Deep Learning Algorithm, Thereby Extrapolating the (MIC) for Each Tested Antibiotic. Source - (Iriya et al. (2020)). . 35

3.2 Image Processing Algorithm Segments Bacterial Cells From the Optical Images and Extracts the Trajectory of Each Bacterial Cell. a) Phase Contrast Optical Images over Time, Where Bright or Dark Elongated Spots Are Single E. coli Cells. b) After Segmentation, the Optical Images Are Transformed Into Binary Images. c) Centroids (Marked by Red Dots) of the Bacterial Cells in the Binary Are Extracted. d) Tracking Algorithm Connects the Centroid of Each Bacterial Cell over Time to Generate Cell Trajectories (Red Lines). Source - (Iriya et al. (2020)). 38

Figure Page

3.3 E. coli Growth Curves and Determination of Optical $LSTM\ MIC$ Values for a) Polymyxin B, b) Ampicillin, c) Gentamicin, d) Streptomycin, and e) Ciprofloxacin. The Dashed Line for Each Antibiotic Marks the Threshold (1.5×) for Obtaining the Optical $LSTM\ MIC$ Values. E. coli Cells Incubated in Healthy Human Urine Without Antibiotics Were Included as Controls (Blue Line). Replicates for Each Time Point Were Obtained by Recording Non-overlapping, 2 s Windows Throughout a Set of Three 30 s Videos. Source - (Iriya et al. (2020)). 40

3.4 Schematic Illustrations of Designed Microfluidic Chip. This Microfluidic Chip Has Six Parallel Detection Channels, Which Allows AST Detection with Different Concentration of Antibiotics Simultaneously. Source - (Iriya et al. (2020)). 43

3.5 a) Original Grayscale Image I. b) Background Subtracted Image I_s. c) Binary Image for Light-colored Cells I_{bright}. d) Binary Image for Dark-colored Cells I_{dark}. e) Final Segmentation Image I_{seg}. Scale Bar: 5 µm. Source - (Iriya et al. (2020)). 48

3.6 a) Original Grayscale Bounding Box Image I_{C1}. b) Segmentation Image I_{C2} with Global Threshold T_{dark}. c) Segmentation with 3 Levels in OTSU Method, I_{C3}. d) Segmentation Image I_{C4} After Selecting Middle Threshold as the Final Threshold. Scale Bar: 200 nm. Source - (Iriya et al. (2020)). 49

Figure Page

3.7 a) Original Segmentation. b) Segmentation After Radon Transform Watershed. c) Thinning Operation. d) Length Plot for Different Angles. Peaks Correspond to Watershed Markers. e) Markers Obtained Using the Radon Transform. Scale Bar: 500 nm. Source - (Iriya et al. (2020)). 50

3.8 a) Radon Transform Watershed. b) Distance Transform Watershed. c) Fast Radial Symmetry Transform Watershed. d) Conditional Erosion Watershed. Scale Bar: 500 nm. Source - (Iriya et al. (2020)). 52

3.9 Binary Image Containing Real Cells and Artifacts (Circled Objects). Artifact Objects Typically Have Lower solidity, Spurs and Holes. Scale Bar: 5 µm. Source - (Iriya et al. (2020)). 54

3.10 $LSTM$ Neural Network Structure. Source - (Iriya et al. (2020)). 59

4.1 Overview of the LVM Setup. A Laser Illuminates the Sample While Side Scattering Images Are Recorded. Source - Modified From (Mo et al. (2019)). 64

4.2 Examples of Samples Under the LVM Setup. 65

4.3 Particle Intensity Plot Revealing the Blinking Effect. 66

4.4 Example of Drift Making Particles Move Along Curves. Only a Few Trajectories Are Shown to Avoid Overcrowding the Image. 66

Figure Page

4.5 a) Block Diagram of the Algorithm Used for Bacterial Identification. After a Localization and Tracking Algorithm, the Original LVM Video Is Transformed and Broken Into Hundreds of Single Particle Videos. The Single Particle Videos Are Used as Inputs for a Machine Learning Classification Model, Which Identifies Particles as Bacteria / Not Bacteria. b) Sequence of Transformations Going from the Original LVM Video to a Single Particle Video. 67

4.6 Drift Vectors in a Frame Calculated Along a 10 x 10 Grid. Longer Arrows Represent Higher Drift. 70

4.7 Structure of the $CNNFA$ Network. 74

4.8 Learning Curves for the Trained Datasets. a) Beads Dataset. b) Urine Dataset 1. c) Urine Dataset 2. d) Urine Dataset 3. 81

4.9 Learning Curves for CNN-$LSTM$ and $CNNFA$ on Dataset 3. 82

4.10 Comparison of the Effect of Different Intensity Caps on the Accuracy. Higher Caps Result in an Unstable Validation Accuracy over the Epochs. 82

4.11 Comparison of the Effect of the Video Duration. A Longer Duration Results in a Better Validation Loss Convergence. Minimum and Maximum values are Circled and Shown in Red. 83

4.12 LVM Setup and Its Components. The Lens in the Photo Has Been Substituted (See LVM Imaging Description). 86

Figure Page

A.1 Histogram Analyses of Length Changes for 40 Cells in PBS Control (a) and PMB (b) Experiments at Different Time Points (After Introduction of Antibiotics for PMB Plots). After Antibiotic Addition, Cell Shrinkage Increased over Time. Comparison of Average Values Between the Control and Antibiotic Experiments for All Time Points Revealed Statistically Significant Differences ($\rho = 3.43 \times 10^{-8}$; Student T-Test). Source - (Iriya et al. (2017)) 100

A.2 Histogram Analyses of Width Changes for 40 cells in PBS Control (a) and PMB (b) Experiments at Different Time Points (After Introduction of Antibiotics for PMB Plots). After Antibiotic Addition, Cell Width Did Not Significantly Change over Time. Comparison of Average Values Between the Control and Antibiotic Experiments for All Time Points Revealed no Statistical Differences ($\rho = 0.75$; Student T-Test). Source - (Iriya et al. (2017)) 101

LIST OF ABBREVIATIONS

Abbreviation	Definition
POC	Point-of-care
AST	Antibiotic Susceptibility Test
LVM	Large Volume Microscopy
UTI	Urinary Tract Infection
HPF	High Power Field
CFU	Colony Forming Unit
ELISA	Enzyme-linked Immunosorbent Assay
MALDI TOF MS	Matrix Assisted Laser Desorption Ionization Time-of-flight Mass Spectrometry
PCR	Polymerase Chain Reaction
FLLS	Forward Laser Light Scattering
FTIR	Fourier Transform Infrared Spectroscopy
MIC	Minimum Inhibitory Concentration
OD	Optical Density
SPR	Surface Plasmon Resonance
CNN	Convolutional Neural Network
AFM	Atomic Force Microscope
LAMP	Loop-Mediated Isothermal Amplification
PMB	Polymyxin B
UPEC	Uropathogenic E. coli

Abbreviation	Definition
LB	Lysogeny Broth
PBS	Phosphate-buffered Saline
MBM	Modified Broth Macrodilution
fps	Frames per Second
ROI	Region of Interest
RNN	Recurrent Neural Network
LSTM	Long Short-term Memory (Neural Network)
CLSI	Clinical and Laboratory Standards Institute
PDMS	Polydimethylsiloxane
CAMHB	Cation-adjusted Mueller Hinton Broth
MSE	Mean Squared Error
SIFT	Scale Invariant Feature Transformation
SFS	Sequential Forward Selection
SVM	Support Vector Machine
RBF	Radial Basis Function
CNNFA	Convolutional Neural Network With Feature Average

LIST OF SYMBOLS

Symbol	Definition
I_1	Intensity of First Half ROI (Differential Detection Algorithm)
I_2	Intensity of Second Half ROI (Differential Detection Algorithm)
k_{dda}	Calibration Slope (Differential Detection Algorithm)
σ	Standard Deviation
T_{bright}	Initial Threshold for Bright Cells (Segmentation Algorithm)
T_{dark}	Initial Threshold for Dark Cells (Segmentation Algorithm)
S_F	Smooth Factor for Length Plot (Watershed Algorithm)
M_{ph}	Minimum Peak Height (Watershed Algorithm)
M_{pw}	Minimum Peak Width (Watershed Algorithm)
M_{pp}	Minimum Peak Prominence (Watershed Algorithm)
M_{pd}	Merging Peak Distance (Watershed Algorithm)
N_p	Maximum Number of Peaks (Watershed Algorithm)
N_{st}	Spur Pixels Threshold (Artifact Removal Algorithm)
E_t	Euler Number Threshold (Artifact Removal Algorithm)
S_t	Solidity Threshold (Artifact Removal Algorithm)
O_t	Bounding Box Area Threshold (Artifact Removal Algorithm)
B_t	Bounding Box Border Threshold (Artifact Removal Algorithm)
A_t	Area Threshold (Artifact Removal Algorithm)
N_{spur}	Number of Spur Pixels (Artifact Removal Algorithm)

Symbol	Definition
E_n	Euler Number (Artifact Removal Algorithm)
Sol	Solidity (Artifact Removal Algorithm)
S_r	Search Radius (Kalman Filter)
M_t	Missed Frames Threshold (Kalman Filter)
C_t	Common Points Threshold (Kalman Filter)
W_{len}	Window Length (Particle Localization Algorithm)
R_{pl}	Search Radius (Particle Localization Algorithm)
Q_t	Quality Threshold (Particle Localization Algorithm)
g_s	Grid Size (Drift Estimation Algorithm)
d_v	Drift Estimate over Different Frames (Drift Estimation Algorithm)
d_{avg}	Drift Regional Estimate (Drift Estimation Algorithm)
α	Drift Moving Average Weight (Drift Estimation Algorithm)
β	Velocity Moving Average Weight (Drift Estimation Algorithm)
M_{dur}	Minimum Track Duration (Single Particle Video Generation)
T_{FWHM}	FWHM Threshold (Single Particle Video Generation)
c_s	Crop Size (Single Particle Video Generation)

Chapter 1

INTRODUCTION

1.1 Background

1.1.1 Relevance

Antibiotic Resistance has become a huge threat to mankind, as many bacteria, commonly known as "superbugs", have developed resistance to several types of antibiotics. Every year, over 2.8 million people are infected by such bacteria in the United States, leading to approximately 223,900 hospital admissions and 35,000 deaths (CDC (2019)). At the current rate, by 2050 the number of deaths in North America is expected to increase to 317,000 a year, while other continents like Africa and Asia are expected to have over 4 millions deaths a year (CDC (2013)) (Fig. 1.1) . Accute infections such as sepsis have a mortality rate of 28-50% (Angus et al. (2001), Sands et al. (1997), Zeni et al. (1997)), what could represent 20,000 deaths per day, worldwide (Daniels (2011)). The spread of multi-resistant bacteria could mean that antibiotic treatments, which for decades have been our only weapon against bacterial infections, are becoming invalid (Hancock (2007)). Recently, it was discovered an E. coli strain that causes urinary tract infections (UTI) resistant to all known antibiotics, including colistin which is used only as a last resort after all other antibiotics have failed. UTI infections are the third most common type of bacterial infection, after respiratory and gastrointestinal infections (Najar et al. (2009)) and they are very common among women, affecting half of them during their lifetime. UTI's can be very dangerous as it is common for the infection to spread and turn into life-threatening infections such as sepsis.

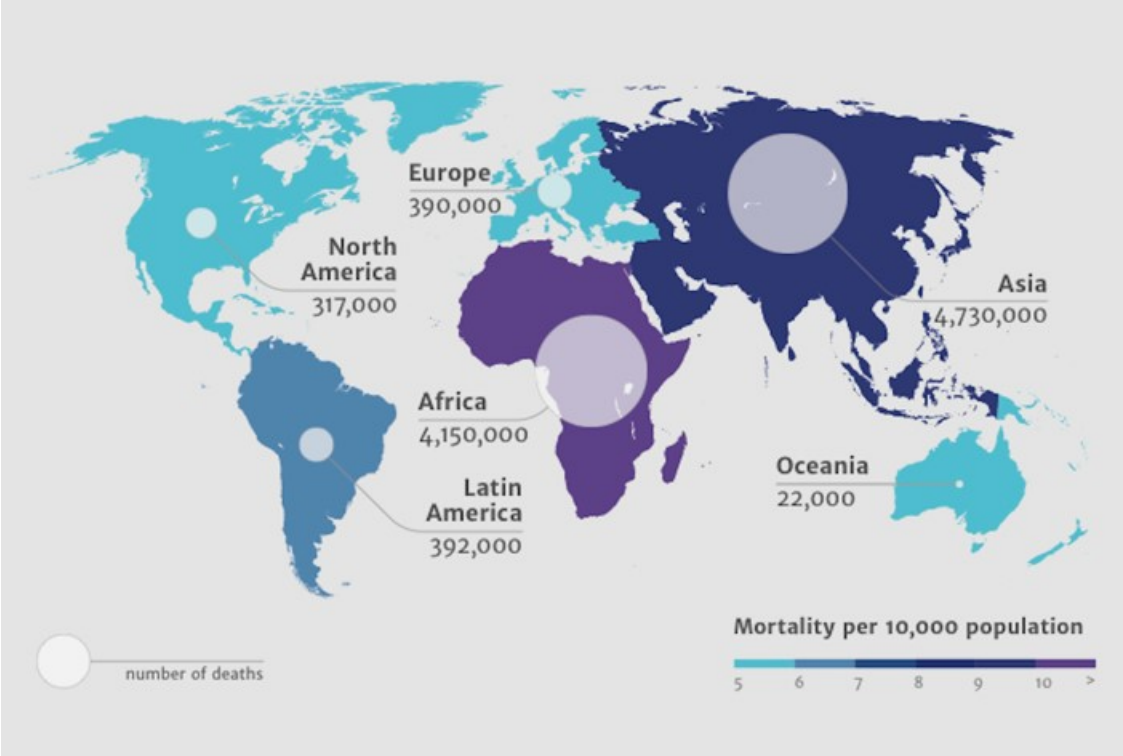


Figure 1.1: Expected Number of Deaths per Year Around the World by 2050. Source - (CDC (2013))

The use of antibiotics itself is the single most important cause of antibiotic resistance (CDC (2013)), as it naturally selects the resistant cells. Figure 1.2 exemplifies the process, showing how resistant bacteria are spread among animals and humans.

Several factors contribute for antibiotics misuse:

- Antbiotics are a major source of profit for drug companies.
- Over the counter sales in several countries.
- Overuse in animal feeds.
- Over-prescription by doctors due to the inefficiency of current diagnostics methods.

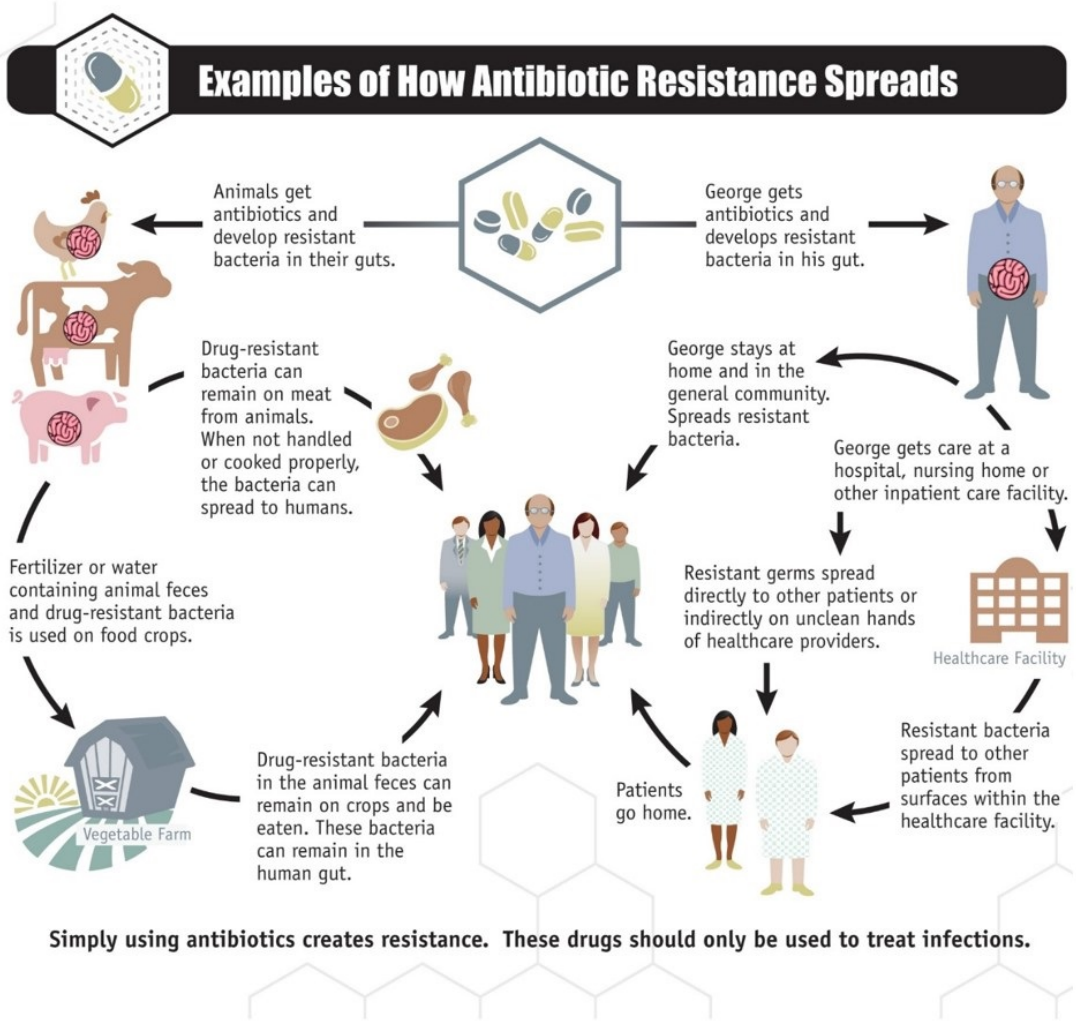


Figure 1.2: Example of Resistance Spread. Source - (CDC (2013))

The next section introduces the diagnostics inefficiency problem, explains why the are methods inefficient and the consequences this brings to patients and to the resistance epidemic.

1.1.2 Diagnostics Inefficiency

Infection diagnostics is comprised of bacterial identification and antibiotic susceptibility tests (*AST*), which select the most appropriate antibiotic for each infected patient. However, current diagnostic methods are slow, typically taking 2-4 days (Muscedere et al. (2008), Liu et al. (2011)) to become ready for the patient. The established techniques for both identification and *AST* involve several time-consuming steps like isolation of pathogens from patient samples, pre-culturing bacteria to enhance the cell density and culturing bacteria with antibiotics (Lazcka et al. (2007), White et al. (1996)), processes which might sum up to several days. These methods rely on cell-culturing which is a slow process that itself usually takes up to several hours to be completed (Muscedere et al. (2008), Liu et al. (2011), Wiegand et al. (2008)). For very slow growing bacteria, (e.g. Mycobacterium tuberculosis) the whole process might take weeks to complete. The current workflow is represented in figure 1.3a: On the first day, the sample is collected and basic identification is performed, in order to validate if there is in fact a bacterial infection. However, in many cases, it is not possible to have this validation without a pure bacteria culture due to the possibility of contamination, multiple infections or insufficient bacteria concentration. Thus, a pure culture is only available on the second day. The pure culture (with a single bacteria type) is also used to initiate the final identification (determining the bacterial strain) and perform *AST* to determine the correct drug for the treatment. Those results are only available on the third day when they are finally reported back to the doctor, and then to the patient. Since the results take so long to become available, many times doctors are forced to prescribe broad-spectrum treatments in the first day, based solely on the patient symptoms. Frequently this treatment is non optimal, since the infection might not be bacterial or resistant bacteria might not be

affected by the chosen antibiotic, naturally selecting them. This inefficient treatment affects patients, doctors and contributes to increase the resistance problem. If a fast culture-independent technique was available, capable of performing analysis directly on biological samples, the results could be made available in the first day, and reported back to the patient at point-of-care (*POC*) or after a couple of hours, what makes for a much better workflow (Fig. 1.3b).

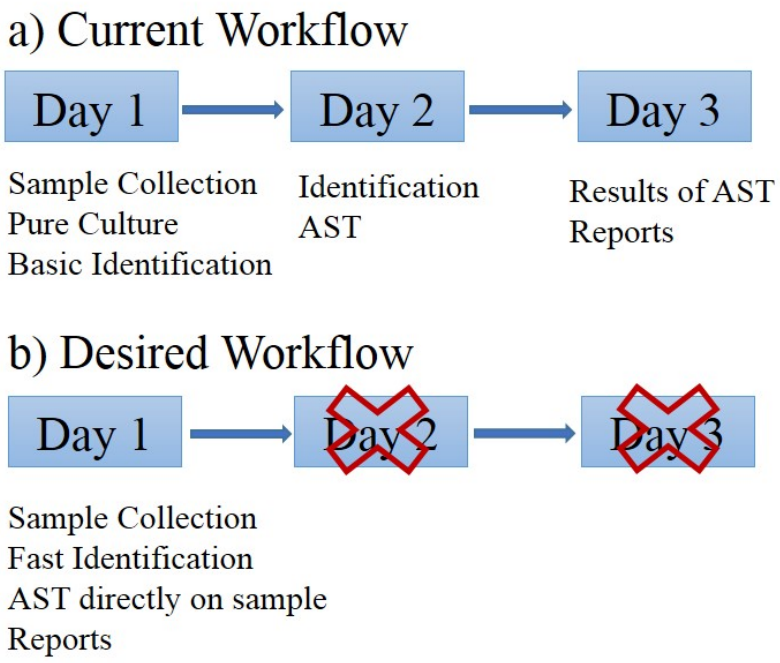


Figure 1.3: a) Current Workflow Typically Taking 3 Days to Complete. b) Desired Workflow, Where Results Are Given Right Away at *POC*.

1.2 Current Methods

1.2.1 Identification Methods

Bacterial infection identification is composed of two parts:

1. Determining if a bacterial infection is present.
2. Determining the agent, the specific bacterial species or strain causing the infection.

In the case of urine samples, the first part is done by urinalysis.

Urinalysis

Urinalysis is a very common test that can be performed in many healthcare settings including doctors' offices, urgent care facilities, laboratories, and hospitals. It is performed by collecting a urine sample from the patient in a specimen cup and can be evaluated by many features:

- Urine's physical appearance (color, cloudiness, odor, clarity) or macroscopic analysis chemical and molecular properties.
- Microscopy.
- Combined with clinical information such as symptons, (dysuria, frequency, urgency, hematuria, suprapubic or back pain), sexual activity, immune status, prior UTI, and patient's past experience.

Urinalysis is performed to identify urinary tract infections, kidney and liver diseases and diabetes. Diagnoses are obtained by reviewing all components of the test, which might include several steps and can be performed in many ways.

The dipstick test is usually the first screening process performed, since it is simple, fast and can be performed at any POC facility. Dipsticks are strips containing several chemical pads that react in contact with urine and test for specific biomarkers such as the presence of blood cells and nitrites . The dipstick test give indications of the presence of an UTI, however the analysis is complicated, full of variables and subjective. For this reason, if abnormalities are found in the dipstick test, further analysis is performed by microscopy and urine culture. Microscopy analysis is performed after the dipstick test to identify abnormal particles in urine. Examples of abnormal particles that can be found in urine include epithelial cells, crystals, casts, white blood cells, red blood cells and bacteria. All abnormal particles suggest the presence of an UTI, but they might also originate from other parts of the body and contamination during the sample collection. The presence of any bacteria is considered to be abnormal, and more than 5 bacteria per high power fields (HPF) - the field of view under the maximum magnification power of the microscope's objective lens - corresponds to 10^5 colony forming units (CFU) per mL, which represents a classic case of UTI. However, in most cases it is difficult to locate the bacteria, and it is necessary to go through several HPF's to count enough bacteria. That makes the process exhaustive if done manually and repeatedly.

In order to automate microscopy and generate faster results, some automatic devices have been developed by combining flow cytometry and light scattering analysis (Sysmex UF1000i) or particle imaging recognition (Iris IQ200). Several attempts have been made to evaluate the performance of those systems (Noyan et al. (2014), van den Broek et al. (2008), Shayanfar et al. (2007)). According to those studies, these devices are very accurate for the identification of blood cells with accuracy higher than 90%, however present lower sensitivity rates for the identification of bacteria when compared to manual microscopy and urine cultures, ranging from 30-

70%. The microscopy results are also improved by combining the dipstick results with an automatic strip reader. All automated systems also have the limitation of not being able to differentiate live and dead cells. Furthermore, these systems do not substitute manual microscopy, and they still require manual reclassification of some particles. Due to the limitations of other alternative approaches, currently culture is still the gold standard, capable of acknowledging all living bacteria present in the sample. As a general rule, an infection is detected if the culture grows into 10^6 - 10^7 CFU / mL.

Species / Strain identification

To identify bacteria down to the species and strain level, other tests must be performed. As different strains of bacteria present characteristic colony morphology (Kshikhundo and Itumhelo (2016)), visual inspection of colonies can be used to identify strains. Besides, biochemical assays test for specific biomarkers by using differential media to culture bacteria and watching for the result of different chemical reactions, where the combination of the test results can distinguish some bacterial strains. As these two methods have limited capabilities on the identified strains, serological tests like the Enzyme-Linked Immunosorbent Assay ($ELISA$) are capable of identifying bacteria down to the serotype level, by testing for specific antigens through correspondent antibody binding. Although it is a fast test, which does not require culturing, it is only a validation method, which becomes costly when too many antigens are tested. Newer methods for identification include Matrix Assisted Laser Desorption Ionization Time-Of-Flight Mass Spectrometry ($MALDI\,TOF\,MS$) and Polymerase Chain Reaction (PCR). $MALDI\,TOF\,MS$ works by ionizing the samples and obtaining the charge to mass spectrum distribution while PCR sequences the DNA to obtain the 16S rDNA. This two competing technologies are able to identify

several strains of bacteria but require destroying the cells and sufficient homogeneous content for a correct identification. For this reason it is usually necessary to have a pure culture prior to the experiment and it is difficult to guarantee single cell detection.

Alternative Approaches

Real-time PCR allows the identification to be performed directly on clinical samples (Dark et al. (2009), Niemz et al. (2011)), however it is an expensive procedure and the results still take a few hours to become available. Raman scattering (Rösch et al. (2005), Xie et al. (2005)) presents enough sensitivity to perform identification at single cell level and avoid culturing but the signals are too weak for a high-throughput analysis. Forward laser light scattering ($FLLS$) (Cline et al. (2017)) can determine the number and size of bacterial cells for concentrations as low as 10^3 CFU/mL, enabling point-of-care applications. However it presents an inability to differentiate bacteria from cell sedimentation, a lack of single cell resolution (as only the total intensity is measured) and an inability to differentiate bacterial strains. Research on imaging methods to identify bacteria at a colony level based on their morphology has been done by several groups (Andreini et al. (2016), Sousa et al. (2013), Zhang et al. (2008)). This approach is simpler than single cell identification, with the disadvantage of requiring culturing. A variation of this approach is the use of Fourier transform infrared spectroscopy ($FTIR$) on bacterial colonies (Helm et al. (1991)). On the other hand, single-cell identification based on morphology has also been attempted (Mohamad et al. (2014)), however most research is limited to differentiating bacteria with different shapes. (He et al. (2018)) and (Jo et al. (2015)) attempt to distinguish different strains of rod-shaped bacteria, by using structured illumination microscopy and quantitative phase imaging, respectively, with the help of traditional

machine learning and principal component analysis (PCA). This is a much more difficult problem than classifying bacteria with different shapes, therefore these works are limited to a few strains. A few groups have also attempted deep learning algorithms for bacteria identification (Liang et al. (2018), Hay and Parthasarathy (2018), Quinn et al. (2016)), with potential for *POC* applications. Deep learning systems have been getting increased popularity due to a superior classification accuracy, however they present a drawback of working as "black-boxes" and requiring extensive datasets to ensure their generalization robustness (Cho et al. (2015)).

1.2.2 AST Methods

Standard methods

Standard *AST* methods rely on culturing bacteria with antibiotics and determining if the drugs can stop the bacteria growth. The disk diffusion (or Kirby - Bauer) method uses antibiotic-impregnated wafers diffused into agar to incubate bacteria for 24 hours. It determines effective antibiotic action by the presence of zones of inhibition, areas with low concentration of bacteria around the antibiotic wafers. Although it is a simple and low-cost method, the results are only qualitative and the exact minimum inhibitory concentration (MIC) - the minimum concentration where bacteria visible growth is prevented - cannot be determined. The gradient diffusion method is a similar method that uses strips with antibiotics on one side and concentration level marks on the other, where the MIC can be obtained from the intersection of the inhibition zone and the concentration marks. This method provides flexibility of the drug choice however it is very expensive if several antibiotics are tested. Also the MIC might not be reliable for certain drug-microbial combinations (Reller et al. (2009)).The most common method employed in most labs is the broth

dilution method. It is a very complete test that uses two-fold dilutions of antibiotics (1, 2, 4, 8, 16,... μg/mL) in a liquid growth medium inside test tubes. Standard practice tests for 12 antibiotic and 8 different concentrations, totaling 96 tubes at a time, being able to generate MIC curves for all different antibiotics and select the best antibiotic for the treatment. This test measure the turbidity, determined by the optical density (OD) - the attenuation of light as it passes through the material - of the cultured bacteria, which can only be correctly measured after several hours (Dalgaard et al. (1994)). More recent developed commercial applications (e.g. BD Phoenix, Vitek2) automatize several steps of the process and employ sensitive optical detection systems, capable of measuring subtle changes in OD, generating AST results after 10 hours, as evaluated by several studies (Mittman et al. (2009), Chatzigeorgiou et al. (2011), Gherardi et al. (2012)). However 10 hours is still a considerable amount of time and unfeasible for POC diagnostics, even if no pre-culturing is necessary.

Alternative Approaches

Several other studies have tried to reduce the test time further, by using different methods (Syal et al. (2017)). One approach uses a magnetic bead rotation sensor to indirectly measure bacteria growth which is proportional to the period of the rotational system (Sinn et al. (2012)). Electrochemical sensors have also been studied for susceptibility detection by measuring small changes in the growth of cells (Karasinski et al. (2007)). Another example is the use of surface plasmon resonance (SPR) to detect changes in optical properties when bacteria are subjected to antibiotics (Chiang et al. (2009)). Although these methods provide innovative faster ways to measure susceptibility, most of them cannot perform AST at an individual cell level and require special equipment, only available at certain laboratories, making it difficult to transform it into a point-of-care technique. On the other hand, image processing

techniques provide simpler approaches based on traditional microscopy, and are more suitable for single cell analysis. Several studies have attempted to measure bacteria growth by measuring area and other features using image analysis (Fredborg et al. (2013), Price et al. (2014), Choi et al. (2013)). In these approaches, microscopy bright field images are analyzed over time, where cells are segmented and the image is transformed into a binary images, so that features like area, length and number of cells can be extracted from the bacterial cells. However, all of these methods still rely on culturing, which depends on cell division cycles and therefore adds time to the process, specially for slow-growing bacteria. Some bacteria strains might require special conditions to culture, or might even be completely uncultivatable (King (2001)). Moreover, these approaches have some limitations since a change in area might occur due to swelling and other events linked to the antibiotic action (Choi et al. (2014)). They also rely in total, large area changes, and therefore requires that a large portion of the population grows. As the popularity of deep learning research grows, it has also been used for AST systems (Yu et al. (2018)). This approach condenses videos into images and uses Convolutional Neural Networks (CNN) (Krizhevsky et al. (2012)) to classify each bacterium as active or inactive. The advantage of deep learning algorithms is that they do not require manually selected and extracted features, such as size and shape of bacterial cells. However, the "black-box" nature of the algorithm makes it challenging to determine which specific features are detected for rapid AST. The algorithm also requires a large data set to account for different bacterial strains and antibiotics (Cho et al. (2015)). Another very interesting approach is the use of Atomic Force Microscope (AFM) cantilevers to detect cantilever deflections caused by bacterial micro-motions, reflecting the metabolic state of the cells (Longo et al. (2013)). This is a non conventional approach which does not rely on cell culturing and instead tries to identify dead cells after antibiotics are introduced to the sam-

ples. (Syal et al. (2016)) also employs a similar concept by measuring bacteria motion from SPR images. Although these methods seem promising, few show feasibility to be adopted in POC without the need of culturing or enrichment. Two approaches stand out in that sense, using loop-mediated isothermal amplification ($LAMP$) (Schoepp et al. (2017)) and large volume microscopy (LVM) (Mo et al. (2019)) to perform AST directly on clinical samples. The LVM system is also used in the current work for bacteria identification (Chapter 3), and we believe these two methods combined offer a practical POC solution for both identification and AST.

1.3 Purpose of This Work

Everything mentioned so far reveals the urgent need for new findings on both antibiotics and methods for diagnostics, to stop or at least slow down the resistance problem. Current methods for bacterial identification and AST have major shortcomings described in the previous section, which impede them to be fast and efficient. This work is part of a larger framework being developed to tackle $POC\ UTI$ diagnostics, while this study focus on computer vision innovations presenting novel methods for AST and identification. The developed methods make use of valuable information present in microscopy image sequences (videos) such as shape, size, texture and other features and should be fast, simple and convenient to implement in any diagnostics facility, including POC. The proposed approaches enable studying bacteria at the single cell level, which can provide results even in the case of multiple infections or contaminations, avoiding the need for a pure culture. This work could lead to a deeper understanding of the interaction between bacteria and antibiotics and should ultimately converge to new tools for UTI diagnostics and test and development of new drugs. This could save costs, lives, and prevent the resistance spread.

The rest of this dissertation is organized as follows:

- Chapter 1 introduces a novel method for detecting membrane deformations on bacteria affected by antibiotics. This method could be used to determine cell viability and to perform AST.
- Chapter 2 details a strategy for imaging-based AST which utilizes bacteria motion patterns and growth information combined with a deep learning algorithm.
- Chapter 3 tackles the bacteria identification problem, using our developed (LVM) system and a deep learning algorithm. The proposed system is suitable for POC applications as it is able to perform directly on clinical samples.
- The last chapter presents the final conclusion, converging all the developed projects and discusses future work.

Chapter 2

BACTERIAL MEMBRANE MORPHOLOGICAL DEFORMATIONS ASSESSMENT

2.1 Introduction

As stated before, there is an emergent need for robust and faster methods to perform AST. In this context, imaging methods appear as great alternatives, as morphological changes between active and inactive bacteria can be observed under a microscope. While live-dead staining kits detect viability by exploring different cell membrane properties between live and dead bacterial cells (Boulos et al. (1999)), it's also known that some antibiotics induce morphological changes on bacteria (Choi et al. (2014)). However if a AST method is to be designed by exploring such properties, it's important to know: 1) How small a change can be detected. 2) How early can this change be detected. In this study, published in 2017 in the Journal of Biomedical Optics (Iriya et al. (2017)), we report an optical method that tackles these two questions by tracking nm-scale membrane deformations in individual bacterial cells with the goal to detect antibiotic action at the earliest possible stage. With sub-pixel precision, the method detects and quantifies subtle bacterial membrane deformations that are difficult to detect using traditional optical imaging analysis methods (Choi et al. (2014); Price et al. (2014)). We study the membrane deformations of two different Escherichia coli strains, E. coli O157:H7 and uropathogenic E. coli CFT073 (Höltje (1995)), associated with antibiotics polymyxin B (PMB) and ampicillin, respectively.

2.2 Method Description

2.2.1 Overview

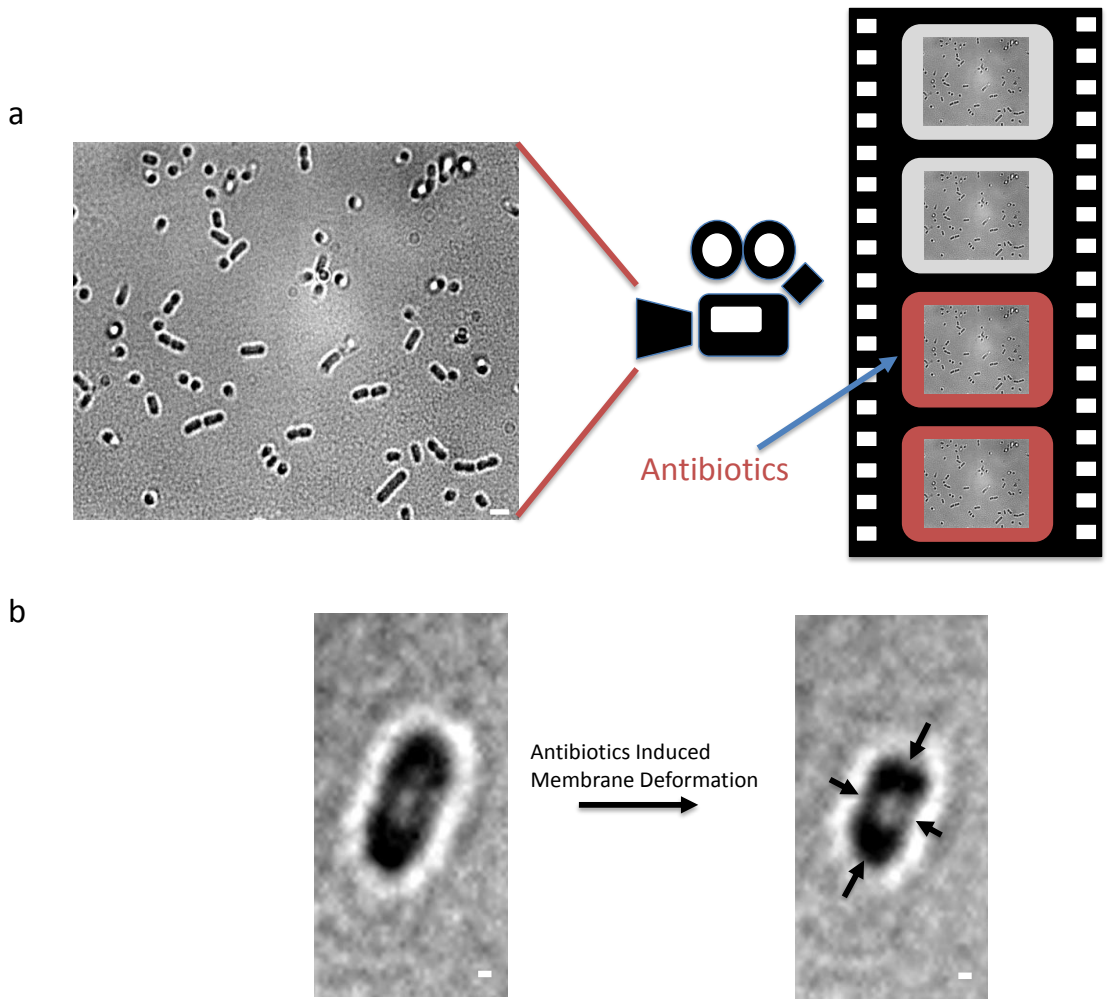


Figure 2.1: Nanometer-scale Optical Tracking of Bacterial Cell Deformation. a) Bacterial Cells (E. coli O157:H7) Are Imaged by an Optical Microscope and Their Responses to Antibiotics Are Recorded and Analyzed. Scale Bar: 2 µm. b) Antibiotic-induced Bacterial Membrane Deformation (Shape, Length and Width) Described by Displacement Vectors (Black Arrows). Scale Bar: 200 nm. Source - (Iriya et al. (2017))

E. coli O157:H7 and uropathogenic E. coli ($UPEC$) strain CFT073 cultures were prepared by diluting overnight cultures into fresh Lysogeny broth (LB) and continuing growth for 2 h at 37°C with gentle rotary mixing until the cells reached the mid-exponential growth phase. The individual bacterial cells were tethered on a glass slide via antibody coupling. For antibiotic testing, bacterial cells were incubated in LB or phosphate-buffered saline (PBS) prior to the addition of ampicillin or PMB, respectively. Optical images of the antibiotic effects on the bacteria were obtained with an inverted optical microscope with a 100× objective (numerical aperture of 1.49) and recorded with a CCD camera (Fig. 3.1a). A key task of our method is to track local cellular membrane deformation, including expansion and contraction, associated with antibiotic action. We describe the local membrane deformation with displacement vectors (Fig. 3.1b). A displacement vector points in the direction normal to the local cell edge with magnitude representing the amount of deformation.

2.2.2 Differential Detection Algorithm

To track subtle cellular deformation, we used a differential detection method (Guan et al. (2014)), which can track deformations as small as ∼9 nm (described in the results section). The method establishes a linear relation between cell deformation and the intensity profile of a region of interest (ROI) that includes the cell edge. The ROI is divided into two halves with one half inside and the other half outside of the cell. The total pixel intensities of these two halves are denoted by I_1 and I_2, respectively (Fig. 3.3a). When the cell expands, I_1 decreases and I_2 increases. In contrast, when the cell shrinks, I_1 increases and I_2 decreases. The edge displacement, d, is given by:

$$d = k_{dda}\frac{I_1 - I_2}{I_1 + I_2} \tag{2.1}$$

, where k_{dda} is a constant obtained through a calibration process. The calibration is performed in the first image frame by moving the ROI normal to the cell edge (Fig. 3.3b). The differential intensity change vs. the ROI movement in terms of pixels reveals a linear relation within a certain range of pixel shift (magnified region of Fig. 3.3b). To obtain a smooth curve and achieve sub-pixel sensitivity, the images are interpolated by 5 pixels (i.e., 4 pixels inserted in between 2 adjacent pixels in both x and y directions). The linear regime is typically within 10 pixels, which corresponds to an actual cellular deformation range of 750 nm.

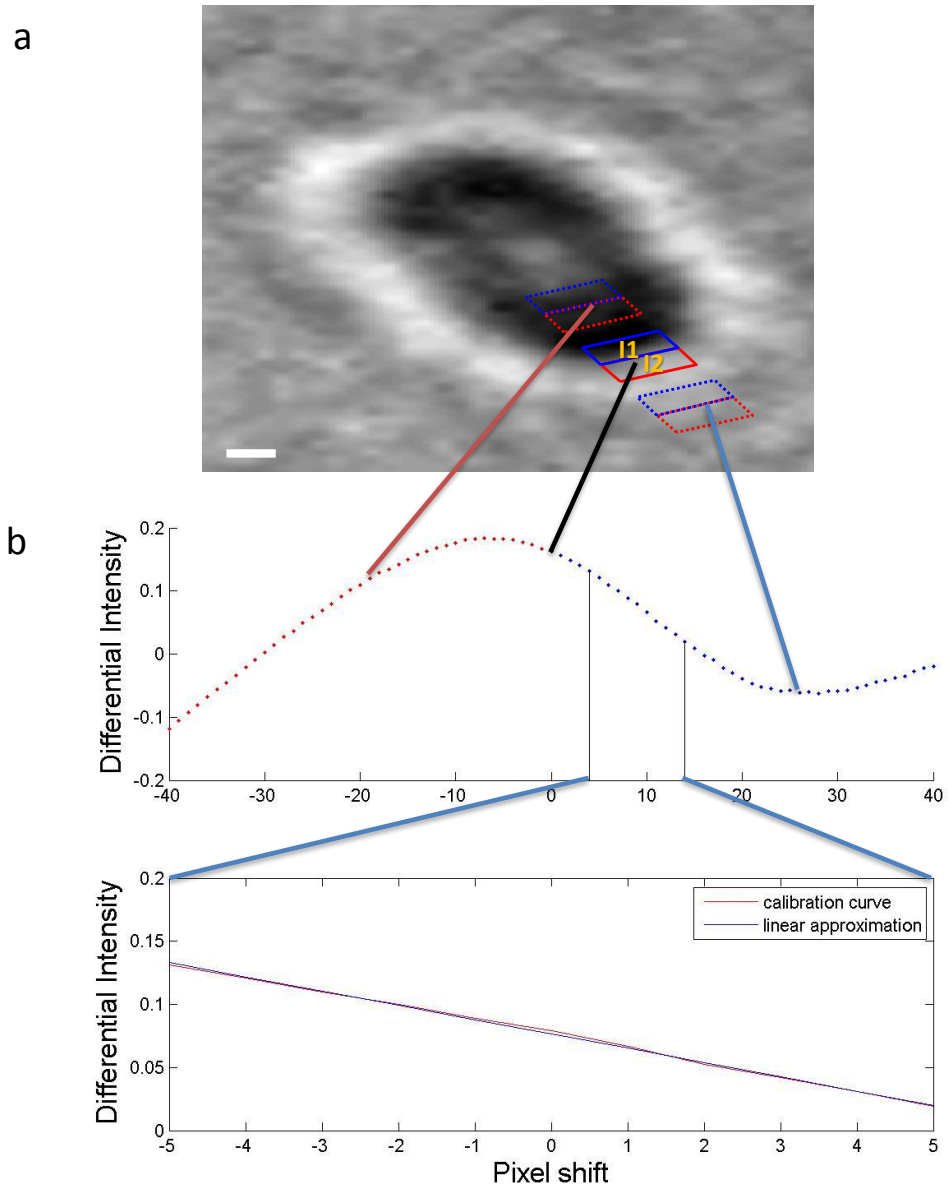


Figure 2.2: Principle and Calibration of the Nanometer-scale Optical Tracking Method. a) A *ROI* at the Cell Edge Is Selected (Blue-red Rectangle) and Divided into Two Halves (Blue and Red) with Optical Intensities Denoted by I_1 and I_2, Respectively. To Calibrate the Method, the *ROI* Is Shifted (Orthogonal to the Cell Edge) by Known Number of Pixels, and Differential Intensity Is Determined. Scale Bar: 200 nm. b) Differential Intensity vs. Pixel Shift. 1 Pixel (Without Interpolation) = 75 nm. Source - (Iriya et al. (2017)).

2.2.3 Materials

E.coli O157:H7 (ATCC 43888) and *UPEC* CFT073 were purchased from Fisher Scientific and ATCC, respectively. Affinity-purified goat anti-E. coli O157:H7 IgG polyclonal antibodies, purchased from Kirkegaard and Perry Laboratory, Inc. (Gaithersburg, MD), were added to 1 mL *PBS* (1×) and stored at -20^{o}C prior to use. *PMB* and ampicillin were purchased from Sigma-Aldrich, dissolved in *PBS* (1×) at stock concentrations of 10 mg/mL and 2 mg/mL, respectively, and stored in dark at 2-8^{o}C. 3-Triethoxysilylpropylamine 99% (APTES), N-Hydroxysuccinimide 98% (NHS), N-Ethyl-N'-(3-dimethylaminopropyl) carbodiimide 97% (EDC), and sodium acetate (NaOAc) were also purchased from Sigma-Aldrich.

Bacterial Preparation

All bacterial stocks were maintained in 5% glycerol at - 80^{o} C in small aliquots (20 µL). After overnight incubation at 37°C, E. coli cells were diluted into fresh *LB* and grown for approximately 2 h at 37°C with gentle rotary mixing until the cells reached the mid-exponential growth phase. Bacterial cells were pelleted via centrifugation at 2000 g for 30 min and resuspended in 1 mL of *PBS* (1×).

Surface Preparation

Glass coverslips (22x22 mm; VWR) were cleaned with deionized water (DW) and ethanol and then dried with nitrogen gas. A small aliquot of 1% APTES in 5% ethanol was applied to the glass slides and allowed to dry at room temperature for 50 - 60 min. After the slides were cleaned and dried, a mixture of 0.1 M NHS and 0.4 M EDC in 1 mL of DW was applied to the slides to produce NHS ester receptors. After 10 min of incubation, the NHS/EDC slides were again cleaned thoroughly with water

and ethanol. The NHS/EDC-activated surface was blow dried with nitrogen. After addition of 30 µg/mL of antibody in 20 mM sodium acetate, pH 5.5 to the slides for 60 min, the slides were cleaned again thoroughly with water and ethanol followed by blow drying with nitrogen, generating an antibody-activated surface for imaging experiments.

Optical Imaging System

The optical imaging system included an Olympus IX-81 inverted microscope with a 100× oil immersion and a Pike 032B CCD camera (Allied Vision Technologies, Newbuyport, MA) to record videos, typically at 50 frames per second (fps) for the PMB experiments and 11.8 fps for the ampicillin experiments. A fast frame rate was used for the PMB experiments to maximize data collection. Since the ampicillin experiments required long video recording to capture bacterial cell bulge/protrusion events, a slower frame rate was used to reduce the data size.

Bacterial Immobilization

flexiPERM® (Sarstedt Inc.) reusable wells (0.5 mL) were mounted and filled with 1× PBS or LB for the PMB or ampicillin experiments, respectively, and 10 µL of bacterial cells (∼108 cells). After 30 min incubation at 37°C to allow bacterial binding to the surface-attached antibodies, unattached bacteria were removed using the flow setup (described below).

Flow Setup

LB, 1× PBS, and PMB (diluted in PBS) were added to the wells through a gravity-based multichannel drug perfusion system with the excess liquid removed by an air pump. A schematic for the flow setup is shown in Fig. 2.3. The drug perfusion

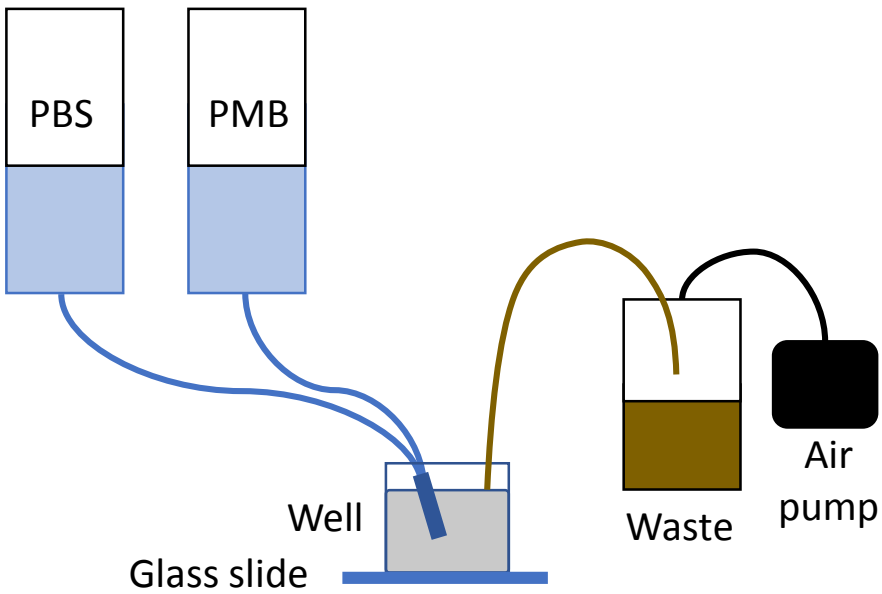


Figure 2.3: Schematic for the Drug Perfusion System. As PBS or PMB Was Injected into The Well, the Suction Pump Concomitantly Removed Excess Liquid from the Well, Thereby Maintaining a Constant Solution Volume. Source - (Iriya et al. (2017)).

system delivered solutions at a flow rate of 330 µL/min with the transition time between different flow solutions ranging from 1 to 2 seconds. For the ampicillin experiment, the antibiotics were manually pipetted into the mounted reusable wells atop the antibody surface with immobilized bacteria.

Image Collection and Processing

All image sequences were collected in transmitted mode at a pixel resolution of 640 x 480. We chose an appropriate exposure time to maximize image intensity and avoid over exposure.

Data Analysis from Images

The images were processed using custom-written MATLAB programs and the methods described previously in the paper. All recorded images were used for analysis, and all displacement plots were smoothed by averaging 20 frames.

2.3 Discussion and Results

2.3.1 Detection Limit

To estimate the detection limit of the method, we performed experiments on dust particles and 1-µm silicon beads on the glass slide (Fig. 2.4). We measured the noise level by using the proposed algorithm and calculating length changes on the dust particles and silicon beads. Since the dust particles were in the camera, not in the chip surface, they measure the pure performance of the algorithm, without external factors. This resulted in a pure noise signal with standard deviation $\sigma =$ 1.66 nm. The 1-µm silicon beads showed some small fluctations and long-term noise, caused by external factors, such as small focus changes due to instabilities of the microscope stage. We defined the detection limit as 3 times the standard deviation in a 10 second window, which is approximately 9 nm. We also tested and measured the system's response to drift changes in the focus plane (Fig. 2.5). For this purpose, we applied a 50 mHz and 500 nm peak-to-peak modulation of the stage position in the z direction (vertical), creating controlled focus changes. The modulation was realized by a piezo microscope stage (Physik Instrumente L.P., Auburn, MA, model P-545.3C7). From this experiment, there was evidence of long-term decay, due to stage drift, and an oscillation that responds nearly linearly to the modulation, with a peak of approximately 25 nm. These results indicated that a 10 nm stage displacement would correspond to a 1 nm (250 / 25 = 10) measured length change. While short-

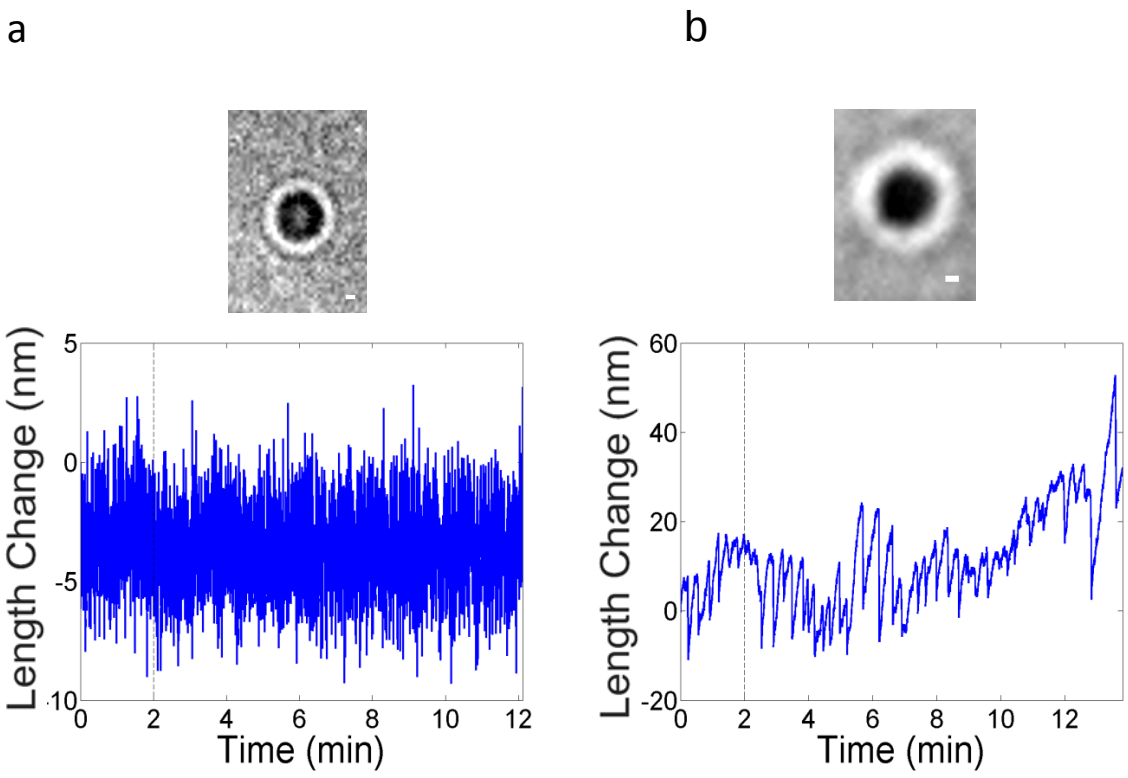


Figure 2.4: Length Change Results for Noise Analysis. a) A Dust Spot in the Camera Was Selected to Assess the Noise of the Algorithm Without External Factors. The Signal Was Pure Noise with Standard Deviation σ = 1.66 nm. b) A Silicon Bead of 1 µm Was Placed on the Chip Surface. The Silicon Bead Showed Some Small Fluctuations and Long-term Noise, Caused by External Factors, such as Small Focus Changes due to Instabilities of the Microscope Stage. The Short-term Noise for a Window of 10 s Showed σ = 3 nm. The Limit of Detection Was Approximately 3σ = 9 nm. Scale Bar: 200 nm. Source - (Iriya et al. (2017)).

term measurement windows would not be significantly affected, stage drift could affect interpretation of long-term measurement results.

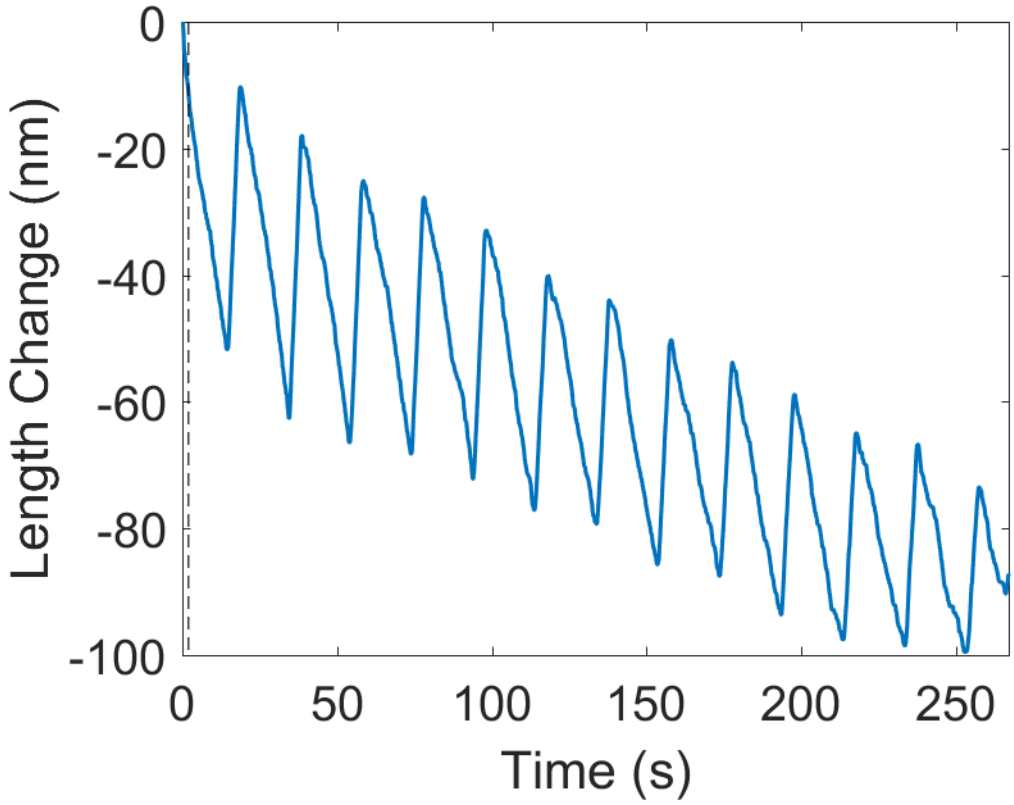


Figure 2.5: Length Change for a Silicon Bead when Submitted to a 50 mHz and 500 nm Peak-to-Peak Modulation of the Stage Position in the Z Direction (Vertical), Creating Controlled Focus Changes. Source - (Iriya et al. (2017)).

2.3.2 Polymyxin B Results

Using the optical tracking technique described in the previous section, we obtained the local displacement vectors of an E. coli O157:H7 cell before and after exposure to PMB from which we determined the corresponding length changes of the bacterial cell (Fig. 2.6a). Before exposure to PMB, the bacterial cell incubated in $1\times$ PBS buffer exhibited minimal changes in cell length (blue curve, Fig. 2.6a). Upon introducing PMB, cell length initially expanded by $\sim$40 nm (arrow, Fig. 2.6a), followed by a large ($\sim$200 nm) shrinkage (red curve, Fig. 2.6a). The

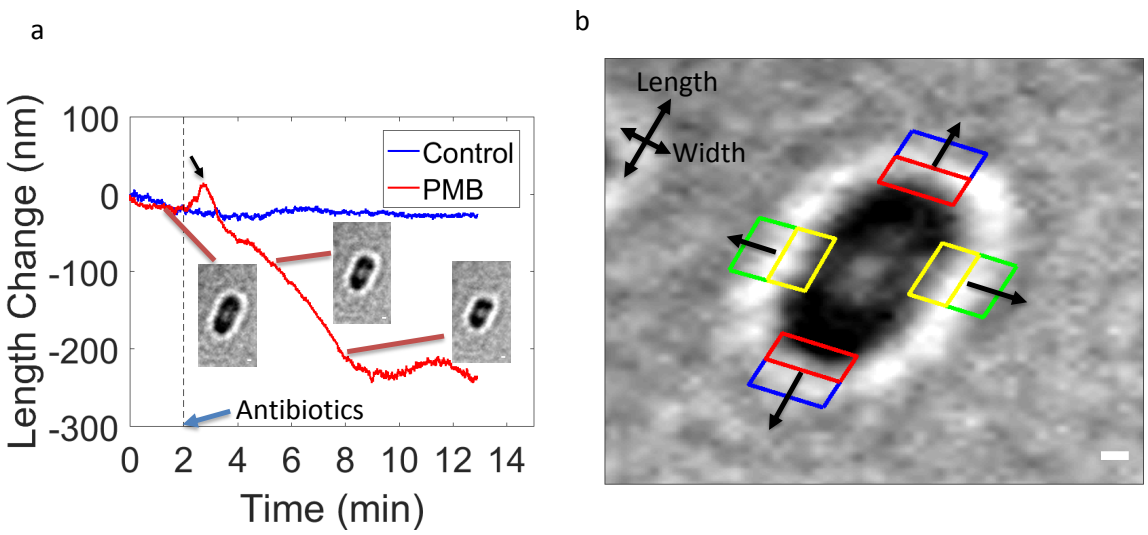


Figure 2.6: a) Cell Length Change of E. coli O157:H7 Exposed to PMB (0.5 µg / mL) (Red Line) Compared to PBS (Blue Line) over Time. The Arrow Indicates the Initial Expansion Shortly After Antibiotic Introduction. b) Examples of ROIs and the Corresponding Displacement Vectors for the ROIs. Length Changes Were Determined by Summing the Two Opposite Vectors of the Red/Blue ROIs, and Width Changes Were Determined by Summing the Opposite Vectors of the Green/Yellow ROIs. Scale Bar: 200 nm. Source - (Iriya et al. (2017)).

PMB antibiotic is a cationic peptide, which elicits bactericidal activity against most Gram-negative bacilli, including E. coli O157:H7 (Daugelavičius et al. (2000)). The observed PMB-induced bacterial cell deformation arises because PMB binds to the negatively-charged lipopolysaccharide layer of the cell and destabilizes the bacterial outer membrane (Daugelavičius et al. (2000)), as the fatty acid portion of PMB dissolves in hydrophobic region of cytoplasmic membrane and disrupts the membrane integrity (Krupovič et al. (2007)). Next, we measured PMB-induced membrane deformation (edge displacement via length and width changes) in 40 E. coli O157:H7 cells exposed to a high concentration of PMB (0.5 mg/mL) (Fig. 2.6b and Fig.

2.7). Length and width changes were calculated by summing opposite displacement vectors, thereby excluding effects caused by changes in cell motion. We intentionally chose a high bactericidal PMB antibiotic concentration, significantly higher than the determined PMB minimum inhibitory concentration (MIC) of 8 µg/mL, to quickly observe deformation in most of the cells, as opposed to using low concentrations where only a few cells showed a significant response. Nearly all cells showed a small, initial expansion in length, followed by a significant decrease in length, which was captured within seconds after PMB addition. Width change in individual cells was less obvious with a few cells displaying decreased width, while other cells increased in width. Although there was also variability in the total length decreases between cells, these variations are expected, given the phenotypic heterogeneity of bacterial cells (Zimmermann et al. (2015)). Bacterial heterogeneity and diversified phenotypic responsiveness underscore the importance of analyzing individual cells with the imaging-based method. Detailed statistical analysis and histograms of length and width responses are provided in Appendix A. Compared to traditional AST methods that measure an averaged feature (e.g., turbidity) of the entire sample, single cell analysis could identify a few antibiotic resistant cells among a large population of susceptible cells by tracking the phenotypic responses of the resistant cells to the antibiotic, which could lead to faster AST. Although the detection limit of the method itself is very small (∼9 nm), external factors, such as the microscope stability (Fig. 2.5) and the attachment of the bacterial cells to the surface, contribute to the accuracy of the measurement. Microscope focus drift can lead to systematic errors in the measurement of the membrane deformation. Micro-motion of cells weakly attached to the surface may also affect the deformation tracking, especially when the cell moves out of the focal plane. Moreover, cells in the solution may occasionally move on top of a cell on the surface, thereby blocking the surface-immobilized cell from the view of

the microscope. These external factors may be reduced by stabilizing the microscope and developing improved cell attachment methods.

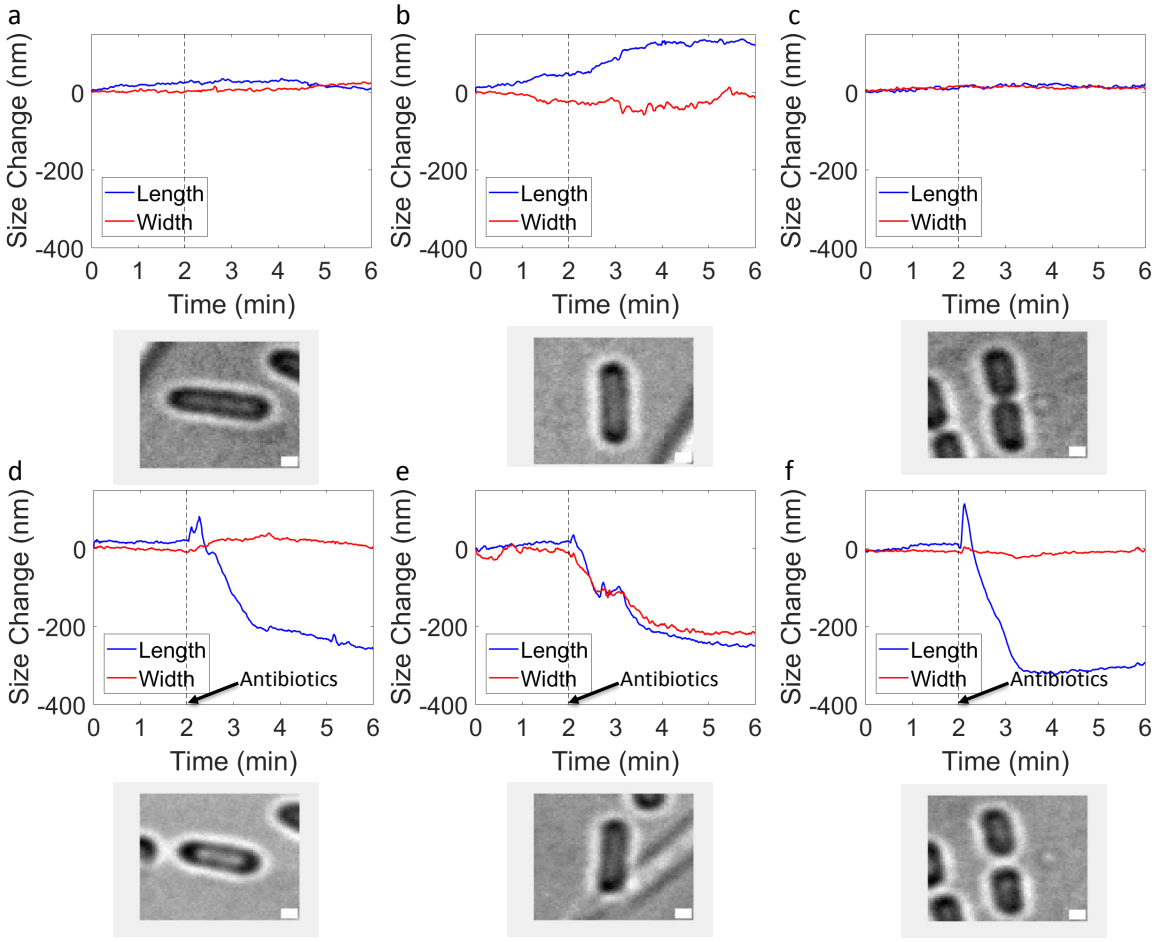


Figure 2.7: Cell Length (Blue) and Width (Red) Changes for Three E. coli O157:H7 Cells. a-c) Three Different Cells Incubated in *PBS* Buffer Only. d-f) Three Different Cells Exposed to *PMB* (0.5 µg / mL). The Vertical Line in Each Plot at 2 Min Marked the Introduction of *PMB*. The Optical Images of Each Cell at the End of the Experiment Are Shown at the Bottom of Each Response Plot (Scale Bar: 500 nm). Source - (Iriya et al. (2017)).

2.3.3 Ampicillin Results

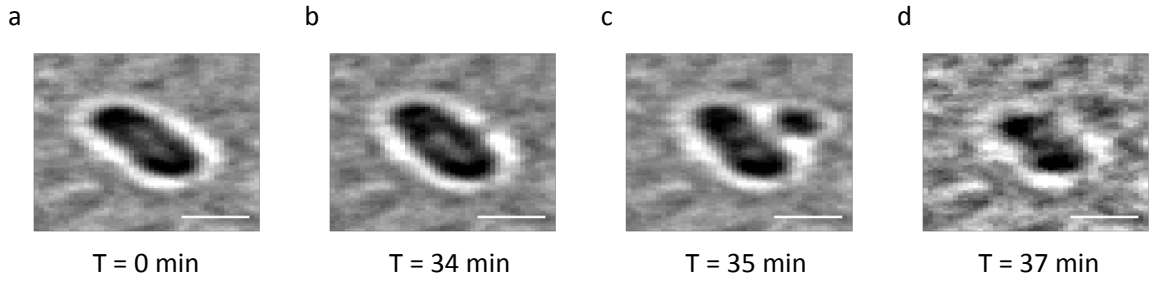


Figure 2.8: Membrane Deformation of a $UPEC$ Cell Exposed to Ampicillin (1 mg / mL). Scale Bar: 200 nm. Source - (Iriya et al. (2017)).

We have also studied $UPEC$ CFT073 exposed to ampicillin (Spratt (1975); Burdett and Murray (1974)), and analyzed the local cellular deformation of individual cells (Fig. 2.8). Unlike PMB-treated E. coli O157:H7, ampicillin causes the $UPEC$ cell to bulge and elongate until cell lysis (Burdett and Murray (1974)). Ampicillin targets enzymes that are critical in forming bacterial peptidoglycan, a thin cell wall layer in gram-negative bacteria composed of long glycan chains, which serve to maintain cell structure and balance turgor pressure (Höltje (1998)). By inhibiting peptidoglycan transpeptidases, ampicillin inhibits cell wall synthesis and bacterial cell division (Spratt (1975); Yao et al. (2012)). Therefore, ampicillin causes the cells to bulge, producing a cytosolic protrusion surrounded by both the cytoplasmic and outer membranes, near the cell septum, and induces expression of autolysins, subsequently leading to cell lysis (Burdett and Murray (1974)). Fig. 2.8 shows different stages of a $UPEC$ cell exposed to ampicillin, with an initial normal appearance, an initial membrane-bound cytoplasmic bulge formed within a few minutes, followed by a large bulge and subsequent lysis (Yao et al. (2012)). Fig. 2.9a shows the image of a $UPEC$ cell captured 20 minutes after exposure to a high concentration of ampi-

cillin (1 mg/mL). Similar to the PMB experiments, we exposed cells to an ampicillin concentration significantly higher than the determined MIC (4 µg/mL) to rapidly induce cellular responses. The local displacements associated with cell membrane deformation at different locations reveal detailed time characteristics linking the formation of a bulge to cell lysis (Fig. 2.9b). The bulge region (magenta, and marked by "1") gradually increases the displacement as the protrusion forms (marked by a circle in the plot). A second location (marked by "2") next to region "1" also shows a displacement increase (cyan curve), indicating that the observed displacement increase in location "1" is not due to noise. The displacements in other locations (e.g., regions 3-5) of the cell display minimal changes. Although the initial bulge formation is small, it can be resolved within ∼9 nm, demonstrating the advantage of the present method over other optical imaging and cell segmentation approaches (Yao et al. (2012)). After the cellular bulge expands over time, cell expansion slows down and is followed by a sudden decrease as cell lysis initiates (marked by thick black arrows). This characteristic cellular response was observed in other $UPEC$ cells (Figs. 2.9c-f), but the magnitude and initiation of cellular deformation vary due to heterogeneity of different cells (Yao et al. (2012)). We have demonstrated a sensitive optical method to track nanometer-scale cell deformation and growth as a phenotypic feature for potential AST using two antibiotics with distinct action mechanisms on the cell membrane and cell wall, PMB and Ampicillin, as examples. Other antibiotics with different mechanisms may not have the same rapid effects on cell deformation. To further develop it into technology for AST, substantial validation experiments will be needed. Examples include testing of other common antibiotics over clinically relevant concentration ranges, both susceptible and resistant strains, and also real clinical samples.

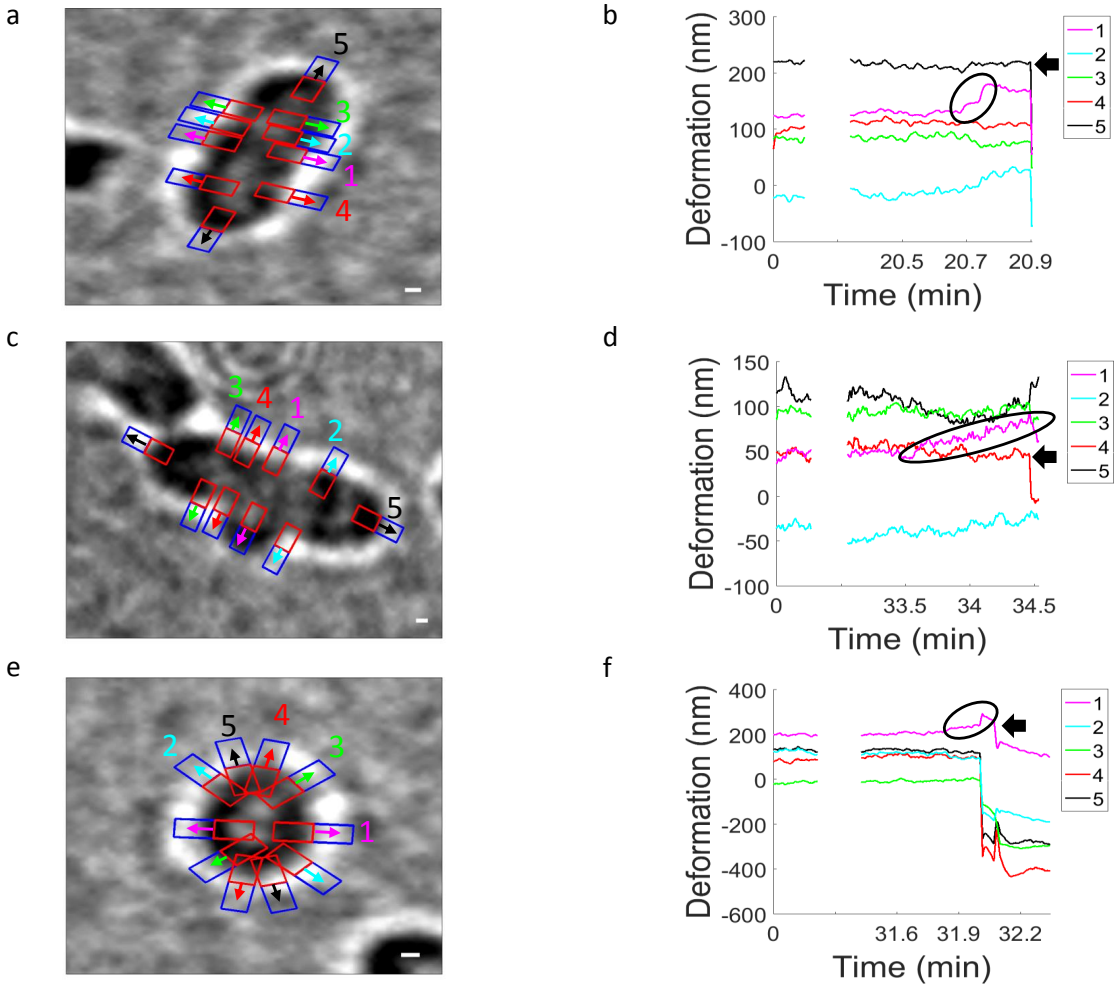


Figure 2.9: Displacement Measurements of *UPEC* Cells Exposed to Ampicillin (1 mg / mL). Displacement Vectors (a, c, e) and Corresponding Cell Plots (b, d, f) Are Shown for Different Regions of Different Cells. The Bulge Region is Shown with Magenta Vectors. The Circled Regions (b, d, f) Indicate the Bulge Membrane Deformation While the Arrows Indicate Cell Lysis. Scale Bar 200: nm. Source - (Iriya et al. (2017)).

2.4 Conclusion

We have developed an optical imaging method to track antibiotic activity on individual bacterial cells in real time. The method measures bacterial cellular deformations with ∼9 nm detection limit, allowing sensitive detection of antibiotic-induced changes in size, shape, and local membrane deformations of single bacterial cells. Using this capability, we have investigated the effects of PMB on E. coli O157:H7 and ampicillin on $UPEC$. PMB caused E. coli O157:H7 to shrink along the cell edge, while ampicillin caused the cellular bulge to form in $UPEC$. Based on tracking membrane deformation changes of single cells, our method will help identify individual cells in a sample that are susceptible to antibiotics in real time. The current detection limit is mainly determined by the stability of the microscope and the attachment of the bacterial cells to the surface. This detection limit may be improved for more accurate tracking of antibiotic-induced bacterial membrane deformations, which may lead to a sensitive AST method. The present work focused on developing a sensitive optical tracking method to detect cell deformation associated with antibiotic activity. Further validation experiments must be performed with additional antibiotics and bacteria, including antibiotic-resistant strains, to establish MIC in conjunction with traditional AST methods. However one of the biggest disadvantages of this method is the requirement of cell immobilization which is complex a procedure with many shortcomings: requires many reagents, requires training, it's time-consuming, has limited effectiveness and limits bacteria concentration (image cannot be too crowded). Another issue is that this method is limited to antibiotics that produce membrane deformations. The next chapter discusses another novel method for AST which attempts to overcome these issues.

Chapter 3

ANTIBIOTICS SUSCEPTIBILITY TESTS BASED ON BACTERIAL MOTION PATTERNS

3.1 Introduction

The method proposed in the previous chapter analyzed drug induced membrane deformations in immobilized E. coli cells as a candidate phenotypic feature to perform AST. However, immobilization is a complex procedure that requires a few hours for reagent action, proper training of staff, has limited efficiency and limits the number of analyzed cells. Moreover, although promising, membrane deformations alone might not be a sufficient phenotypic feature to determine AST, since it is limited to antibiotics that produce membrane deformations. In this context, and motivated by promising results of motion-based approaches (Longo et al. (2013), Syal et al. (2016)), we proposed a new study, published in IEEE Sensors Journal in January 2020 (Iriya et al. (2020)). The method differentiates active and inactive cells captured by optical images using combined phenotypic features: bacterial growth and motion patterns. Also motivated by a previous work from our group (Yu et al. (2018)) which uses convolutional neural networks to perform AST, this approach combines information from both growth and motion using state of the art recurrent neural networks (RNN), providing more robust and faster results. There is no need to rely on genetic testing, thereby avoiding detection limitations caused by incomplete resistance genes. Our method is also capable of performing single cell analysis, like other imaging approaches with the advantages of being label-free and immobilization free and use a simple phase contrast microscope. Experiments performed in free solution

avoid surface modification, so there is no need to consider the efficiency of bacterial capture. Labeling could also affect bacterial activity and thereby affect the accuracy of test results. The detection limit is between 10^6 - 10^8 CFU/mL and the throughput is limited to one sample at a time. In contrast to the CNN approach presented in (Yu et al. (2018)), the new method focuses on single bacterial cell motion patterns and changes of the patterns in the presence of different antibiotics. To extract the motion patterns, we developed a robust segmentation and tracking algorithm to determine the motion pattern of each bacterial cell, and a Long Short-Term Memory ($LSTM$) neural network to analyze the pattern over time. This approach makes full use of time information and the sequence of events, potentially generating more robust and intuitive models than those created with static images. In addition, since this model only uses positions of the bacterial cells, it requires much less data than full image-based CNN, thus enabling easier training and application. The $LSTM$ approach also allows prediction of bacterial motion, which can be useful for robust bacterial tracking. In addition to applying this new method to our previous CNN-analyzed AST data (Yu et al. (2018)), we extended the studies to include additional antibiotics. We validate the method using Escherichia coli (ATCC 43888) and five antibiotics, including polymyxin B, ampicillin, gentamicin, ciprofloxacin and streptomycin. These antibiotics were selected as representative compounds with different mechanistic activities and are inclusive of both bacteriostatic and bactericidal antibiotics. We demonstrate the method's ability to differentiate active and inactive cells and to obtain accurate AST results as fast as 30 minutes.

3.2 Discussion and Results

3.2.1 Image Processing and Deep Learning Algorithms

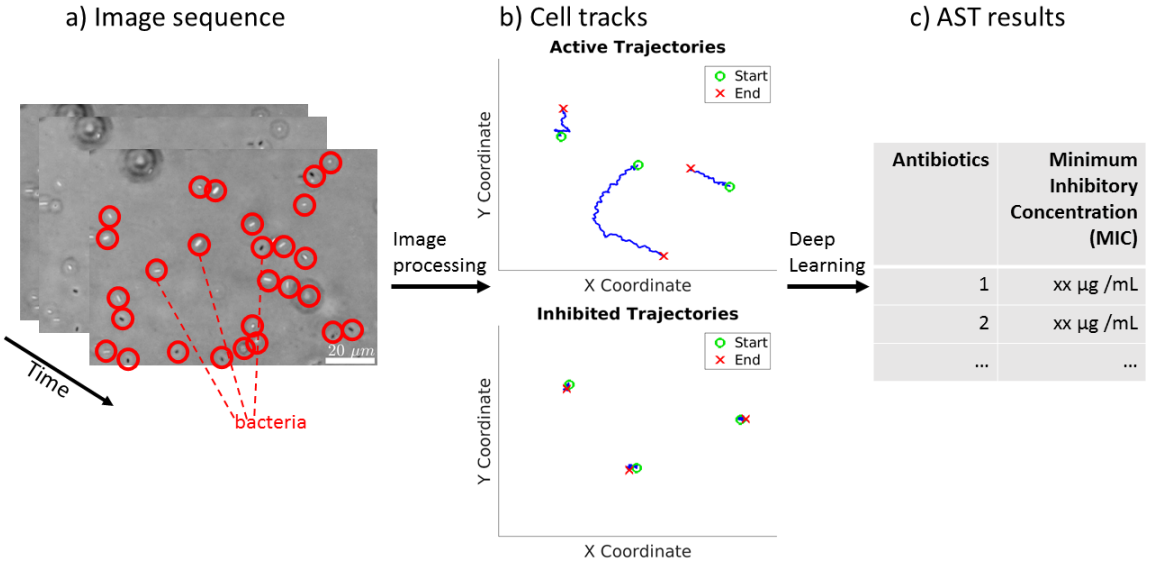


Figure 3.1: a) Single Bacterial Cells Are Imaged in Urine in a Microfluidic Channel Using Phase Contrast Microscopy. The Cells are Revealed Either as Bright or Dark Spots, Depending on Their Relative Positions in the Focal Plane (Each Cell is Marked with a Red Circle). b) Image Sequence Over Time (2 s) Shown in Panel (a) Is Fed into an Algorithm Comprising Two Parts: Image Processing and Deep Learning. The Former Includes Segmentation and Tracking Algorithms to Obtain Individual Bacterial Cell Trajectories (Motion Pattern). The Latter Processes the Trajectories with a Deep Learning Algorithm to Determine if a Cell is Active and Inactive and Records the Number of Active and Inactive Cells. c) *AST* Results Are Generated From the Number of Active Cells Obtained Using the Deep Learning Algorithm, Thereby Extrapolating the (MIC) for Each Tested Antibiotic. Source - (Iriya et al. (2020)).

Phase contrast microscopy reveals individual E. coli cells inside a microfluidic channel in Lysogeny Broth (LB), a rich bacterial growth medium (Fig. 3.1a). Instead of attaching the cells onto a solid support (Gregory and Mello (2005)), the bacterial cells freely move within the microfluidic channel, allowing tracking of single bacterial cell motion as an important phenotypic feature. Because the bacterial cells constantly move in and out of the field of view of the optical microscope, this method also allows analysis of a larger number of different bacterial cells. Tracking and analyzing larger numbers of bacterial cells reduce statistical errors associated with a finite number of bacterial cells. In the presence and absence of different antibiotics and multiple antibiotic concentrations, bacteria are imaged for 30 seconds. Subsequently, the image sequence is modeled to generate cell trajectories, which are processed into a deep learning algorithm to classify the cells as either active or inactive (Fig. 3.1b). From the classified trajectories, the number of active cells is determined and plotted as a function of concentration for each antibiotic, from which the minimum inhibitory concentration (MIC) - the lowest antibiotic concentration at which the bacterial strain does not grow - is obtained (Fig. 3.1c). We applied the model to five antibiotics: polymyxin B (Bonura et al. (2013), De Majumdar et al. (2013), Fernández et al. (2013)), ampicillin (Goodman et al. (2011)), gentamicin (Ginalska et al. (2005), Kohanski et al. (2008), Liou et al. (2006), Thompson et al. (2002), Vaiana and Sanbonmatsu (2009)), ciprofloxacin (Drlica and Zhao (1997)) and streptomycin (Sharma et al. (2007)). Using two-fold increasing concentrations from 0.5 – 16 µg/mL, we visually observed killing activity (bactericidal effects) for polymyxin B, ampicillin, and gentamicin. Inhibitory activity (bacteriostatic effects) was observed for streptomycin and ciprofloxacin with low concentrations (< 0.5 µg/mL).

3.2.2 Image Segmentation and Cell Motion Pattern Determination

For each image frame, bacterial cells are first segmented with a threshold to generate a binary image, where connected objects represent bacterial cells (Fig. 3.2). The threshold and the algorithm are evaluated by visual inspection. Then, the centroid of each cell is identified, representing the position of the cell at a given time (image frame). Position changes over time are tracked from adjacent image frames, which are connected and recorded as the cell trajectory. More details about the algorithm can be found in the Algorithms section.

3.2.3 Overview of $LSTM$ Algorithm and Experimental Setup

Antibiotic	MIC $CLSI$ reference (clinical standards)	MIC Modified broth macrodilution (experimental AST)	MIC Optical $LSTM$ (experimental AST)
polymyxin B	$\leq$ 2 µg/mL	2 µg/mL	1 µg/mL
ampicillin	$\leq$ 8 µg/mL	2 µg/mL	4 µg/mL
gentamicin	$\leq$ 4 µg/mL	4 µg/mL	4 µg/mL
streptomycin	None	4 µg/mL	16 µg/mL
ciprofloxacin	$\leq$ 1 µg/mL	0.03125 µg/mL	0.0625 µg/mL

Table 3.1: Comparison of the Optical $LSTM$ Experimental AST with Modified Broth Macrodilution AST and $CLSI$ AST Interpretive Standards

To utilize the trajectories of bacterial cells tracked with the imaging processing algorithm, a machine learning algorithm that can model time-dependent features is essential. $LSTM$, utilized in this study, is such an algorithm that models long time

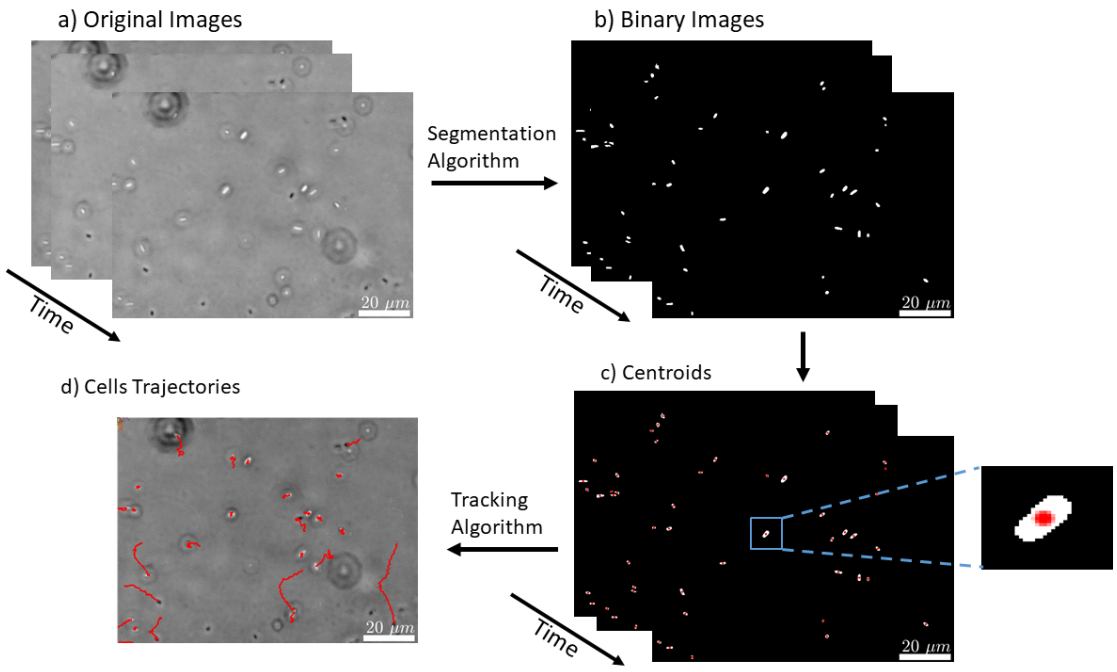


Figure 3.2: Image Processing Algorithm Segments Bacterial Cells From the Optical Images and Extracts the Trajectory of Each Bacterial Cell. a) Phase Contrast Optical Images over Time, Where Bright or Dark Elongated Spots Are Single E. coli Cells. b) After Segmentation, the Optical Images Are Transformed Into Binary Images. c) Centroids (Marked by Red Dots) of the Bacterial Cells in the Binary Are Extracted. d) Tracking Algorithm Connects the Centroid of Each Bacterial Cell over Time to Generate Cell Trajectories (Red Lines). Source - (Iriya et al. (2020)).

sequences and retains critical information and features, enabling robust training of the model (Ordóñez and Roggen (2016)). Because different cells are located at different positions within the image, all cell trajectories are set to start at positions (0,0) by subtracting the first point from the rest in the time sequence and used as the input for the $LSTM$ algorithm. Since the entire trajectory of each bacterial cell is processed into $LSTM$, there is no need to manually extract motion features, such as speed and direction of the motion, and their changes over time (Amsler (1996),

Pottash et al. (2017)). We analyzed several thousand cell trajectories in the presence of each antibiotic with the goal of dividing them into two categories: active cells or inactive cells. Active cell trajectories were obtained from the images of control samples, (healthy human urine spiked with E. coli without antibiotics) captured throughout each experiment (Fig. 3.3). Inactive cell trajectories were captured from the images of samples treated with each antibiotic at its respective highest concentration ($4\times$ MIC obtained from the modified broth macrodilution (MBM) experimental AST), recorded 120 min after the beginning of the experiment. Since there is no standard method for determining single cell activity level, we must assume all the cells in the control videos are active and all the cells in the high drug concentration videos are inactive. Even though this assumption may not be true, the machine learning algorithm should capture the patterns if the majority of the cells follow the assumption. The upper limit on $4\times$ MIC was determined experimentally as we observed it was sufficiently high to inhibit most cells. The proposed algorithm is ultimately evaluated by comparing the obtained MIC to the one obtained using the clinical standard method. To establish an experimental MIC for each antibiotic, we used the MBM AST approach (see Materials and Methods). Table 3.1 compares the results obtained using the optical $LSTM$ AST and with MBM, as well as the expected values from the Clinical and Laboratory Standards Institute ($CLSI$) reference (CLSI (2015a), CLSI (2015b)). With the exception of streptomycin, the optical $LSTM$ MIC results were in good agreement (± 1 dilution) with the MBM method (Table 3.1). The small disagreements could be due to expected sample variability and differences in the setup conditions, for example the usage of room temperature instead of $37^{\underline{o}}$ C, to ensure better bacterial motion.

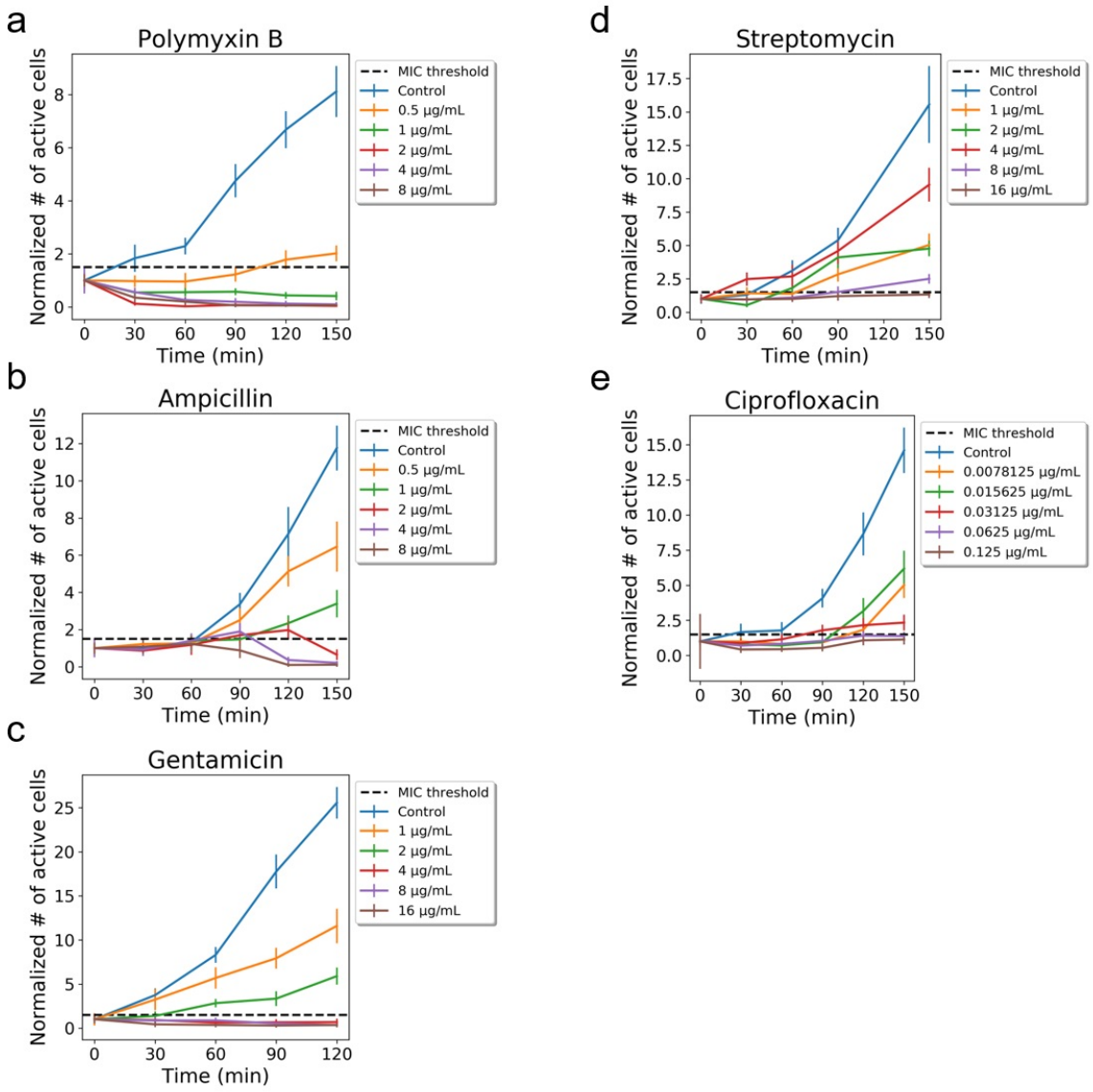


Figure 3.3: E. coli Growth Curves and Determination of Optical *LSTM MIC* Values for a) Polymyxin B, b) Ampicillin, c) Gentamicin, d) Streptomycin, and e) Ciprofloxacin. The Dashed Line for Each Antibiotic Marks the Threshold (1.5×) for Obtaining the Optical *LSTM MIC* Values. E. coli Cells Incubated in Healthy Human Urine Without Antibiotics Were Included as Controls (Blue Line). Replicates for Each Time Point Were Obtained by Recording Non-overlapping, 2 s Windows Throughout a Set of Three 30 s Videos. Source - (Iriya et al. (2020)).

3.2.4 Optical $LSTM$ AST

To determine MIC with the trained $LSTM$ algorithm, the number of active cells, measured every 30 min, was recorded for each antibiotic at different concentrations (Fig. 3.3). For each growth curve, the number of active cells was normalized using the initial number of cells determined at 0 min from the first image frame (Fig. 3.3). This plot contains both motion and general growth information, as the number of active cells is correlated with both features. The slope of each curve decreases with increasing drug concentrations, showing that higher concentrations have a greater effect on the cells. We set a threshold at 1.5× the initial number of the active cells for each antibiotic (horizontal dashed lines in Fig. 3.3). If the cells are inhibited, the number of active cells remains at or below the threshold at each time point. Conversely, if the cells are not inhibited, then the number of active cells increases above the threshold over time. The antibiotic concentration that demonstrated consistent growth inhibition throughout 150 min (Gentamicin only needed 120 min) was defined as the optical $LSTM$ MIC. For all time points when the growth control exceeded the 1.5× threshold, the $LSTM$ MIC values for all antibiotics recorded at 150 min (120 for gentamicin) were similar to earlier time points (Fig. 3.3a-c, e). We randomly selected 80% of the cell trajectories to train the $LSTM$ model for each antibiotic and used the remaining 20% to test the accuracy of the trained $LSTM$ model (Table 3.2). We chose not to separate the test phase into test and validation as we did not perform hyper-parameter selection or best epoch selection, cases where a validation set is required. The $LSTM$ model produced excellent accuracy for polymyxin B, ampicillin, and gentamicin, but was less accurate for streptomycin and ciprofloxacin (Table 3.2). This observation indicates that motion pattern alone is inadequate to determine if there is susceptibility to some antibiotics. However, the $LSTM$ algorithm is capable

Antibiotic	Active			Inactive		
	# of cells		Accuracy (%)	# of cells		Accuracy (%)
	Training	Test		Training	Test	
polymyxin B (8 µg/mL)	2886	722	84.49	2915	729	96.30
ampicillin (8 µg/mL)	2886	722	85.87	2454	614	91.86
gentamicin (16 µg/mL)	2886	722	83.66	2480	621	94.69
streptomycin (16 µg/mL)	2886	722	42.94	2962	741	55.87
ciprofloxacin (0.125 µg/mL)	2886	722	46.81	2956	739	80.11

Table 3.2: $LSTM$ Learning Results for Different Antibiotics.

of determining the total number of active cells in the sample and its change over time. If the bacterial strain is inhibited by an antibiotic at a certain concentration, the cell number will not increase over time, so the number of active cells serves as an additional phenotypic feature for AST.

3.3 Experimental Setup

A polydimethylsiloxane ($PDMS$) microfluidic chip with a channel volume less than 100 nL was fabricated by soft lithography and used for the AST experiments described here (Lee et al. (2005), Jing et al. (2013), Jing et al. (2014)). The chip included two layers of $PDMS$, the upper layer was a pneumatic control layer (RTV

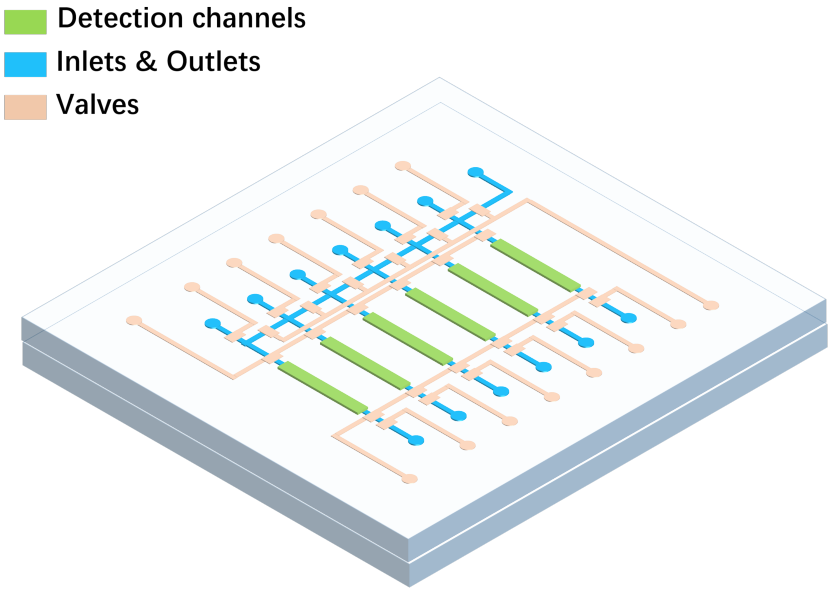


Figure 3.4: Schematic Illustrations of Designed Microfluidic Chip. This Microfluidic Chip Has Six Parallel Detection Channels, Which Allows *AST* Detection with Different Concentration of Antibiotics Simultaneously. Source - (Iriya et al. (2020)).

615, the ratio of A/B is 5:1) and the bottom layer was a fluidic layer (RTV 615, the ratio of A/B is 10: 1). The two layers were aligned by thermopolymerization reaction and bonded on a glass slide with oxygen plasma. The mold of the microfluidic chip was made from photoresist (the positive photoresist AZ-50XT was used for fluidic layer mold and the negative photoresist SU8-2025 was used for control layer mold and the inlet and outlet channels mold). Fig. 3.4 shows the detailed structure of the microfluidic chip. The chip includes six channels, which are controlled by independent valves and main valves. The function of the valve is to allow each channel to perform experiments with different concentrations or different antibiotics in parallel or separately. For one reaction channel (0.5 cm in length, 25 µm in height, 200 µm in width),

the sample solution was injected into the microchannel by a syringe pump. After the injection, the pneumatic valve is closed to stabilize the solution in the channel, which eliminates the effects of the fluid and ensures that all movements are caused by bacterial activity and not by liquid flow. The outlets were connected to a waste bottle by Teflon tubing. The microfluidic chip was placed on an inverted microscope (Olympus IX-81) with a 40× phase contrast objective lens and a CCD camera (Pike-032B, Allied Vision Technologies, Newburyport, MA) to record phase contrast images. The recording process was controlled using software AVT Smart View (Version 1.14.1). All imaging sequences were collected at 100 fps at a pixel resolution of 640 × 480. An appropriate exposure time was chosen to maximize image intensity and avoid over exposure. Images were recorded in raw format and batch-converted to 16-bit tiff format using a MATLAB program. The images were subsequently processed using custom-written MATLAB and Python programs. Since bacterial cells are typically resolved with positive contrast (bright) and negative contrast (dark) in phase contrast imaging, we developed algorithms to process positive and negative contrast bacterial images and to track cells that moved towards and away from the focal plane.

3.4 Materials and Methods

3.4.1 Materials

Photoresist SU-8 2025 and photoresist AZ 50 XT were purchased from Microchem and AZ Electronic Materials USA Corp., respectively. $PDMS$ (RTV-615-044) was purchased from Momentive Specialty Chemicals (NY). The wafer was purchased from Avago Technologies. E. coli ATCC 43888 (Biosafety Level 1 organism that lacks the genes for Shiga-like I and II toxins) was purchased from Fisher Scientific. Unfiltered, pooled human urine specimens from multiple healthy individuals (Lot: BRH1041997)

were purchased from BioreclamationIVT Co and were stored at -80°C immediately after receiving and thawed prior to the experiment. Antibiotics, including polymyxin B, ampicillin, gentamicin, ciprofloxacin and streptomycin and all other reagents were purchased from Sigma-Aldrich.

3.4.2 Antibiotics Preparation

Polymyxin B, ampicillin, gentamicin, and streptomycin were individually prepared as 200 µg/mL stock solutions in ultrapure water. Ciprofloxacin was first dissolved in 0.1 mol/L of HCl (1:60, m/v) prior to generating 200 µg/mL stock solutions in ultrapure water. Antibiotics were stored at -80°C in the dark. Before *AST*, the antibiotic stock solutions were thawed at room temperature and diluted in ultrapure water to a series of different concentrations.

3.4.3 Bacteria Cultivation and Preparation

E. coli ATCC 43888 was stored at -80°C in 5% glycerol. After aerated and agitated growth at 35°C for approximately 16 h, saturated E. coli (20 µL) was diluted into *LB* (5 mL) and cultured for approximately 2 h at 35°C to attain a logarithmic phase of growth. Maeda et al (Maeda et al. (1976)) demonstrated that E. coli K-12 exhibits greater swimming motility (straighter paths) at 20°C and greater tumbling motility (circular paths) at 39°C. In order to maximize the straighter path trajectories for the *LSTM* algorithm and training, the bacteria were maintained at 25°C for 3 h before the beginning of the optical-based *AST* experiments. Bacterial cells were then collected by centrifugation at 450g for 5 min and resuspended in unfiltered healthy human urine (BioreclamationIVT Co.) to a concentration of 2×10^7 cells/mL. The bacteria-spiked urine samples were filtered using a 5 µm syringe filter (EMD Millipore) to remove large particles.

3.4.4 Optical $LSTM$ AST

After dilution to appropriate cell concentrations in urine, antibiotics were added to the E. coli suspensions for optical-based AST. Briefly, the E. coli-spiked urine samples (200 µL) were mixed with an equal volume (200 µL) of antibiotic solution (in ultrapure water) prior to beginning of each optical-based AST experiment. The antibiotic concentrations ranged from 4 – 0.25× MIC as determined via modified broth dilution testing (described below). The upper limit on 4× MIC was determined experimentally as we observed it was sufficiently high to inhibit most cells. The mixtures were simultaneously injected into different microfluidic channels, and the valves were closed after the microfluidic channels were fully filled. Continuing incubation at 25°C, bacterial status was recorded every 30 min at 100 fps for 30 seconds. Using this method, we analyzed the antibiotics previously described by Yu et al (Yu et al. (2018)) and included gentamicin, a more clinically-relevant aminoglycoside antibiotic.

3.4.5 Modified Broth Macrodilution AST

To compare the optical-based AST to more traditional AST, the MBM approach was adopted. After centrifugation at 450g for 5 min (described above), E. coli was resuspended in cation-adjusted Mueller Hinton Broth ($CAMHB$) (Sigma-Aldrich) and adjusted to 1×10^6 cells/mL after UV-Vis spectrophotometer (NanoDrop 2000, Thermo Fisher) readings at $OD600$. Thereafter, the E. coli suspension (1 mL) was mixed with an equal volume (1 mL) of antibiotic solution (in ultrapure water) at a specific concentration, resulting in half-strength $CAMHB$ and initial bacterial concentrations of approximately 5×10^5 cells/mL. As a positive control, the E. coli suspension (1 mL) was mixed with an equal volume (1 mL) of ultrapure water without

antibiotics. After incubation at 37°C for 16h, the tube with the lowest concentration of each antibiotic that lacked visible growth was recorded as the MIC value. All MBM experiments were performed in triplicate.

3.4.6 Growth Curves and MIC Determination

MIC curves were generated in the following manner: 30-second videos were analyzed for each antibiotic, concentration, and time point. Each video was subdivided into fifteen 2-second videos, which were then processed with the $LSTM$ algorithm, generating a count of active cells. The average count over all the sub-videos represented one point in the MIC curve, with the respective standard deviation shown as an error bar.

3.5 ALGORITHMS

3.5.1 Segmentation

We developed a robust segmentation algorithm composed of 4 steps: Initial segmentation, Refined Segmentation, Watershed and Artifact removal. The final segmentation I_{seg} obtained after all steps and is shown in Fig. 3.5e. The used parameters for our experiments were: T_{bright} = 800, T_{dark} = -500, S_F = 10, M_{ph} = 5, M_{pw} = 10,M_{pp} = 0.5, M_{pd} = 5, N_p = 3, N_{st} = 4, E_t = 1, S_t = 0.77, O_t = 70, B_t = 60, A_t = 15. All spatial units are measured in pixels.

Initial Segmentation

1. Initial segmentation is performed by pre-defined global threshold's T_{bright} and T_{dark} (selected through visual inspection), which give a rough estimate of the bacteria locations.

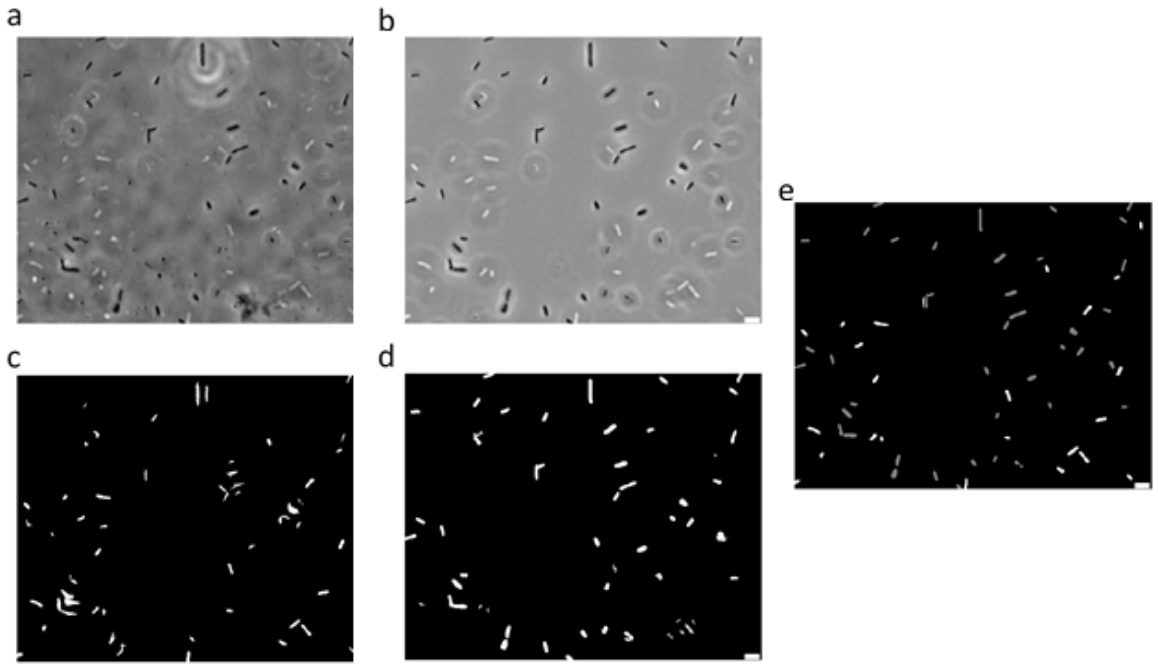


Figure 3.5: a) Original Grayscale Image I. b) Background Subtracted Image I_s. c) Binary Image for Light-colored Cells I_{bright}. d) Binary Image for Dark-colored Cells I_{dark}. e) Final Segmentation Image I_{seg}. Scale Bar: 5 µm. Source - (Iriya et al. (2020)).

2. To reduce background noise, the grayscale image I (Fig. 3.5a) needs to go through background subtraction. The background is computed by averaging all the frames in the entire video. The subtracted image results in image I_s (Fig. 3.5b).

3. I_s is transformed into two binary images for any pixels with intensities higher than T_{bright} and lower than T_{dark}, generating binary images I_{bright} and I_{dark}, respectively (Figs. 3.5c and 3.5d).

Refined Segmentation

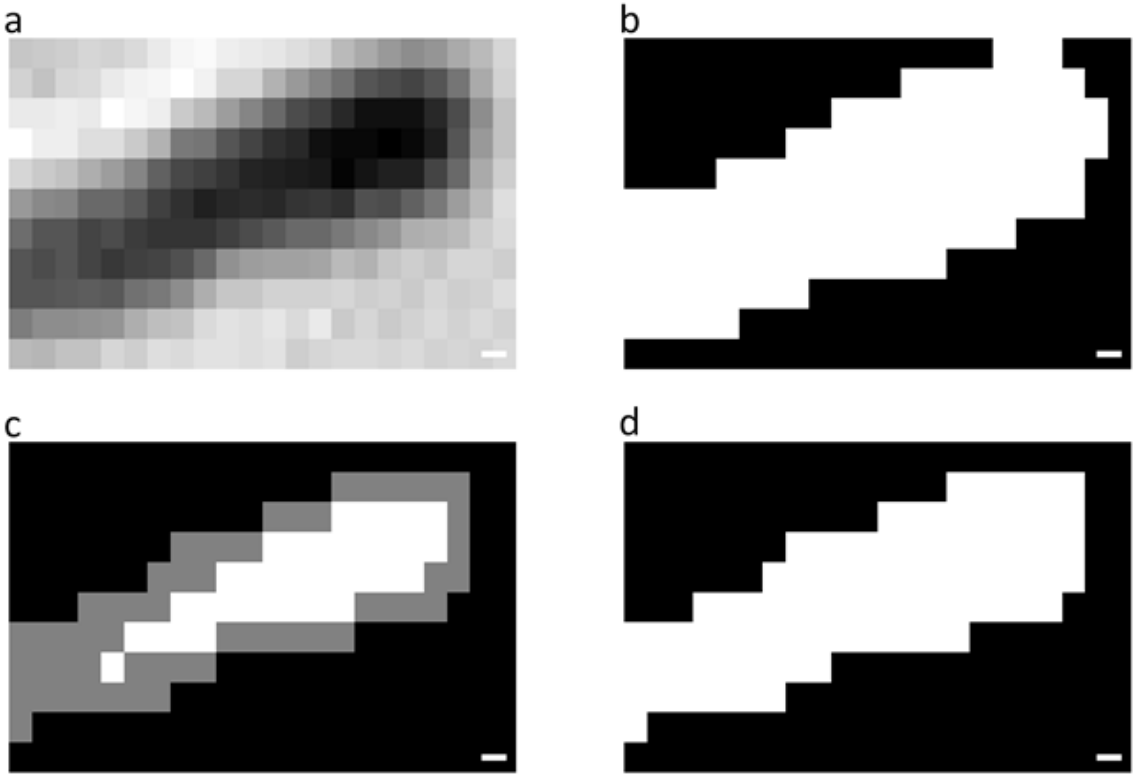


Figure 3.6: a) Original Grayscale Bounding Box Image I_{C1}. b) Segmentation Image I_{C2} with Global Threshold T_{dark}. c) Segmentation with 3 Levels in OTSU Method, I_{C3}. d) Segmentation Image I_{C4} After Selecting Middle Threshold as the Final Threshold. Scale Bar: 200 nm. Source - (Iriya et al. (2020)).

1. The initial segmentation is refined for each connected component in I_{bright} and I_{dark} using the OTSU's method (Otsu (1979)).

2. A bounding box is calculated being the smallest rectangle which encloses the connected component. The bounding box selects an area corresponding to the connected component on the original grayscale image I generating image I_{C1}

(Fig. 3.6a). The corresponding bounding box on image I_{bright} or I_{dark}, is image I_{C2} (Fig. 3.6b).

3. The OTSU algorithm is applied to the bounding box, generating image I_{C3} (Fig. 3.6c), which contains 3 threshold levels.

4. We use the middle threshold to generate the final binary image I_{C4}, for the connected component (Fig. 3.6d).

Watershed

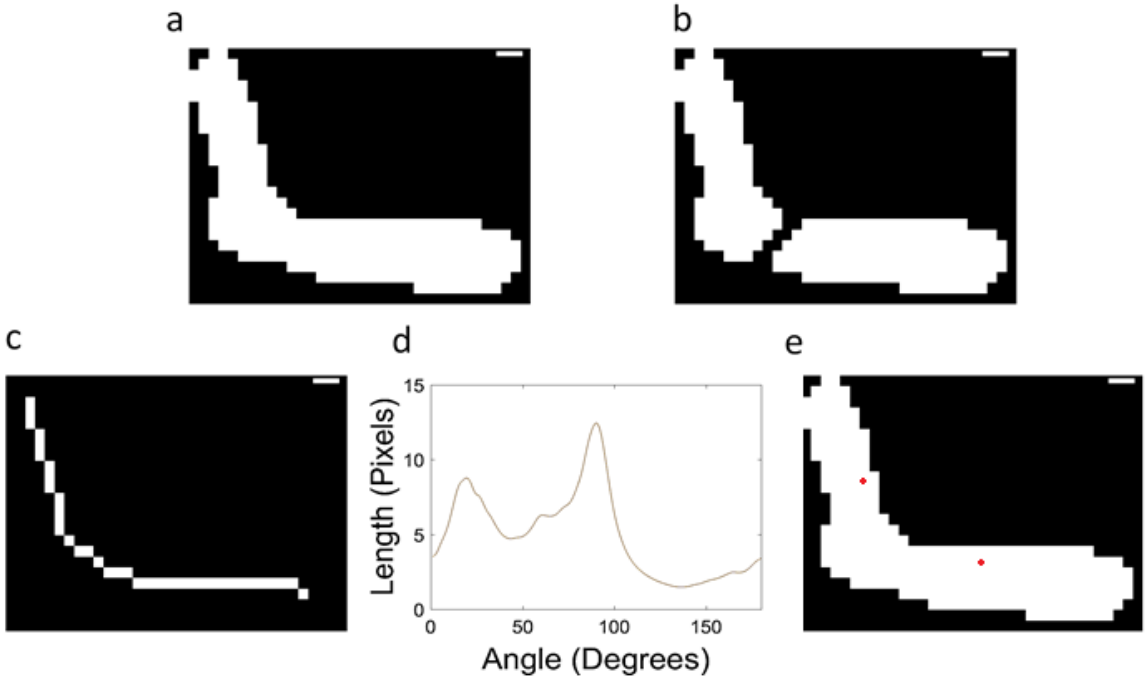


Figure 3.7: a) Original Segmentation. b) Segmentation After Radon Transform Watershed. c) Thinning Operation. d) Length Plot for Different Angles. Peaks Correspond to Watershed Markers. e) Markers Obtained Using the Radon Transform. Scale Bar: 500 nm. Source - (Iriya et al. (2020)).

As overlapping bacteria are frequent, we developed an algorithm to separate overlapping bacteria using a marker-controlled watershed (Beucher (1979)) based on the Radon transform (Radon (1986)). Fig. 3.7a shows an example of two overlapping cells, and Fig S3b shows the result after applying the watershed algorithm. The watershed algorithm is based on the following steps:

1. For each connected component, we perform the thinning operation to transform the cells into lines (Fig. 3.7c). This is convenient since the E. coli cells are rod-shaped.

2. Next, we perform the Radon transform on the thinned object and select the maxima for each angle from 0° to 180°. This generates a length plot for each direction, where the peak represents the bacteria orientation.

3. The length plot is circularly shifted so that the global peak is at the center of the plot. This avoids having two peaks, in case the peak is close to 0° or 180°. Connected components containing two or more bacteria should exhibit two or more local peaks (Fig. 3.7d).

4. The length plot is smoothed by smooth factor S_F to correct noisy peaks.

5. Only peaks that obey certain rules are selected, such as having a minimum peak height M_{ph}, minimum peak width M_{pw} and minimum peak prominence M_{pp}.

6. Peaks that are too close by a distance of M_{pd}, are merged into a single peak with height as the average of the two peaks, and width as the sum of the two widths.

7. The number of obtained peaks per connected component is limited to N_p, to avoid over-segmentation. Priority is given to peaks with greater height.

8. For each peak, a marker is found at the center of the object, along the specified direction, departing from the position where a maxima is found (Fig. 3.7e).



Figure 3.8: a) Radon Transform Watershed. b) Distance Transform Watershed. c) Fast Radial Symmetry Transform Watershed. d) Conditional Erosion Watershed. Scale Bar: 500 nm. Source - (Iriya et al. (2020)).

Since the E coli cells are rod-shaped, this approach showed to be more robust than distance transform (Malpica et al. (1997)) and radial transform-based watershed methods (Zafari et al. (2015)), which would often lead to oversegmentation and to conditional erosion methods (Yang et al. (2006)), complicated schemes with un-

expected results, causing either oversegmentation, undersegmentation, or separating cells at imprecise points. Fig. 3.8 compares the results of all these methods.

Artifact Removal

One of the biggest challenges is eliminating non-bacteria objects originated from artifacts surrounding the bacteria, after background subtraction (Fig. 3.9). Artifacts are removed by post-processing the segmented images according to the following steps:

1. Artifacts usually consist of sharp objects containing lots of spurs and holes inside. Many artifacts can be removed by calculating the number of spur pixels N_{spur} in the connected components, the Euler number E_n (1 - number of holes inside the connected component) and the solidity Sol (Area / Area of bounding convex polygon). This way, objects with $E_n > E_t$, $N_{spur} > N_{st}$ and $Sol < S_t$ are removed.

2. Another indication of an artifact is that after OTSU thresholding, very often the resulting image occupies almost the entire bounding box or more than 2 entire borders. Thus, objects that occupy more than O_t % of the bounding box area or B_t % of the bounding box border are also removed.

3. Small objects resulting from noise are eliminated by area threshold A_t.

Artifacts that are connected to real bacterial cells usually vanish after the OTSU refinement. Most of the remaining objects can be removed during tracking, since they are of intermittent nature, and result in very short trajectories. We also noticed more occurrence of artifacts for the light cells, most likely because our optical setup has its focus adjusted for the dark cells.

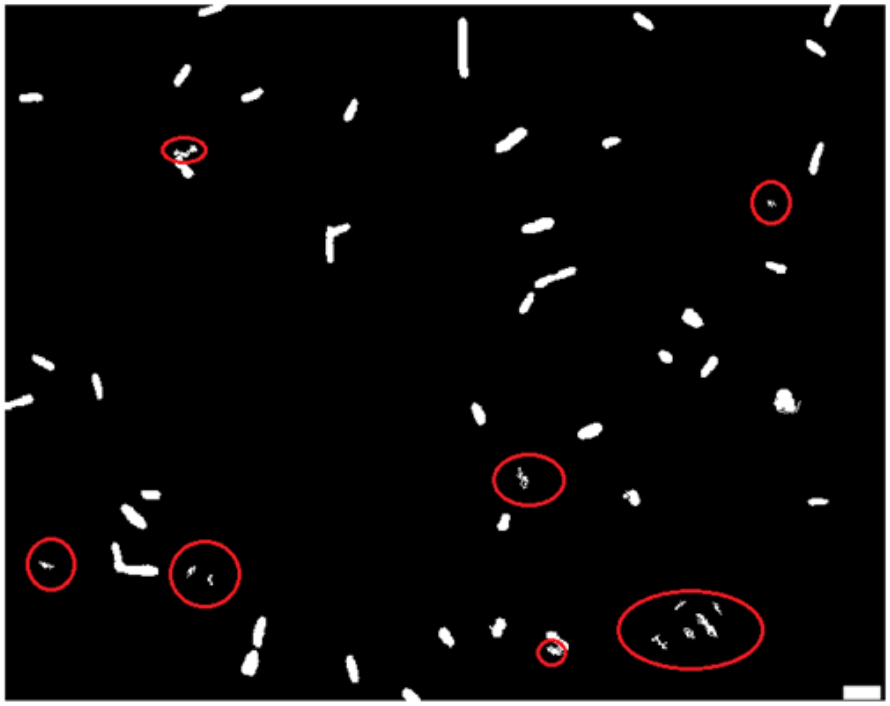


Figure 3.9: Binary Image Containing Real Cells and Artifacts (Circled Objects). Artifact Objects Typically Have Lower solidity, Spurs and Holes. Scale Bar: 5 µm. Source - (Iriya et al. (2020)).

3.5.2 Cell Tracking

Overview

We developed a tracking algorithm based on a linear Kalman Filter, capable of tracking cells under different focal planes, undergoing color changes. Cells are tracked from the first to the last frame over windows of 200 frames (2 seconds) using the centroids of all objects obtained from I_{bright} and I_{dark}. We also keep track of bacteria color in each frame (dark or bright) to improve the robustness of the algorithm. Tracking

is performed by a linear Kalman Filter (Yang et al. (2006), Mendel (1995)) and the system is modeled by the equations:

$$\begin{cases} X_{priori}(t) = AX(t-1) + q(t) \\ Z(t) = CX(t) + r(t) \end{cases} \tag{3.1}$$

$$X(t) = X_{priori}(t) + K\left(Z(t) - CX_{priori}(t)\right) \tag{3.2}$$

, where $X(t)$ is the state vector, $Z(t)$ is the observation vector, A is the state transition matrix and C is the observation matrix, K is the Kalman gain and $q(t)$ and $r(t)$ are Gaussian random variables with distributions $p(q) \sim N(0, Q)$ and $p(r) \sim N(0, R)$. The state vector is described by $X = [x, y, v_x, v_y, a_x, a_y]^T$, where (x, y) denote position and v and a denote velocity and acceleration, respectively. The state transition matrix and observation matrix are:

$$A = \begin{bmatrix} 1 & 0 & 1 & 0 & \frac{1}{2} & 0 \\ 0 & 1 & 0 & 1 & 0 & \frac{1}{2} \\ 0 & 0 & 1 & 0 & 1 & 0 \\ 0 & 0 & 0 & 1 & 0 & 1 \\ 0 & 0 & 0 & 0 & 1 & 0 \\ 0 & 0 & 0 & 0 & 0 & 1 \end{bmatrix} \qquad C = \begin{bmatrix} 1 & 0 & 0 & 0 & 0 & 0 \\ 0 & 1 & 0 & 0 & 0 & 0 \end{bmatrix}$$

To estimate the observation noise matrix R, the transition noise covariance matrix Q and the error covariance matrix P, we manually segmented 10 cells over 200 hundred frames (2000 points) and calculated the error between the automatic segmentation and the manual segmentation, as well as the error between the predicted positions and the real cell positions. Cells were selected from videos with high bacte-

ria concentration (180 minutes after the beginning of a control experiment), to test the algorithm under a stressful scenario. For R, only errors above 0.5 were taken into account. We also found that the maximum cell displacement between two adjacent frames was smaller than 5 pixels (925 nm).

Algorithm

1. At each frame, we compute the distance of each measured centroid to the position of all trajectories in the previous frame. For each measured centroid, only trajectories within the search radius S_r are considered as candidates.

2. The a priori Kalman estimate is used to compute the expected position of each trajectory in the current frame (Eq. 3.1).

3. Candidate trajectories are sorted according to the distance of their expected positions to the measured centroid. Higher priority is given to trajectories that are currently the same color as the measured centroid, even if distances are greater. The first connected centroids are the ones with closest matches and higher priority is also given to those whose closest matches maintain the trajectory color.

4. Each measured centroid determines the observation vector, which is connected to the closest match as long as this match is not already taken by another cell in the current frame. In the latter case, an attempt to connect to the second closest is made and so on. If no matches are left within the search radius, this represents a new trajectory. This case covers new cells coming from the borders, from a different focal plane and bacteria divisions.

5. Once the observation vector is connected to a trajectory, the new state estimate for this trajectory is determined by the a posteriori Kalman estimate (Eq. 3.2). The Kalman filter helps addressing bad segmentations, missed segmentations, and sorting out trajectories that are too close or overlapping.

6. After all measured centroids are connected to different trajectories, some trajectories might be left unconnected. This might happen when two different trajectories converge to the same point, represented by a single measured centroid. In that case, we connect the trajectory to the closest measured centroid to the a priori estimate, as long as this centroid is within S_r and keeps the trajectory color. We found the trajectory color criterion important since artifacts are often mistaken for this case, as they are inherently close to the real cells.

7. If no measurements are found for a determined trajectory, the new state vector is obtained solely from the a priori Kalman estimate. This keeps the trajectory alive if a segmentation fails for that frame, or if the cell momentarily leaves the field of view in the XY plane or is out of focus. However if this trajectory misses a measurement for M_t frames in a row this trajectory is terminated, since the cell has left the field of view for good. All the last M_t estimates are also eliminated since it is more likely that they were not real.

8. It's also common to have two trajectories stuck in the exact same path, either because an artifact managed to blend with a cell trajectory or because the algorithm lost track of two close real trajectories. In that case, if the common points exceed C_t, we determinate a base trajectory, which is either the oldest one or the one which was connected first, if they were created in the same frame. The other trajectory is then terminated, eliminating all the common points in this trajectory.

After visual evaluation of several values for the global parameters, the following parameters were selected: $S_r = 15$ pixels, $M_t = 5$, $C_t = 20$.

3.5.3 Machine Learning

$LSTM$ models were used for two tasks: 1) Creating profiles for active and inactive cells. 2) Bacterial cell motion prediction. The tracks obtained from the tracking algorithm were used as inputs for both neural network models. The Keras library was used with the Theano backend (Chollet et al. (2015)) to generate the $LSTM$ models.

Active / Inactive Cell Classification

Only trajectories with at least 50 frames are utilized for model training or classification. Short trajectories are padded with zeros to a sequence of length 200, to make the network dimensions compatible and masking is applied to consider only the relevant part of the sequence. Models use 1 $LSTM$ layer of dimension 128, batch size of 32, the Adam optimizer (Ruder (2016), Kingma and Ba (2014)),binary cross-entropy as the loss function and were trained over 10 epochs. The network structure is shown in Fig. 3.10.

Bacterial Cell Motion Prediction

We also tested models to predict the bacteria trajectory using $LSTM$ networks and the same manually segmented trajectories used for estimating the Kalman Filter parameters. The aim is to predict the next position from a sequence of previous positions, and we use as entries the sequence of position errors between adjacent frames

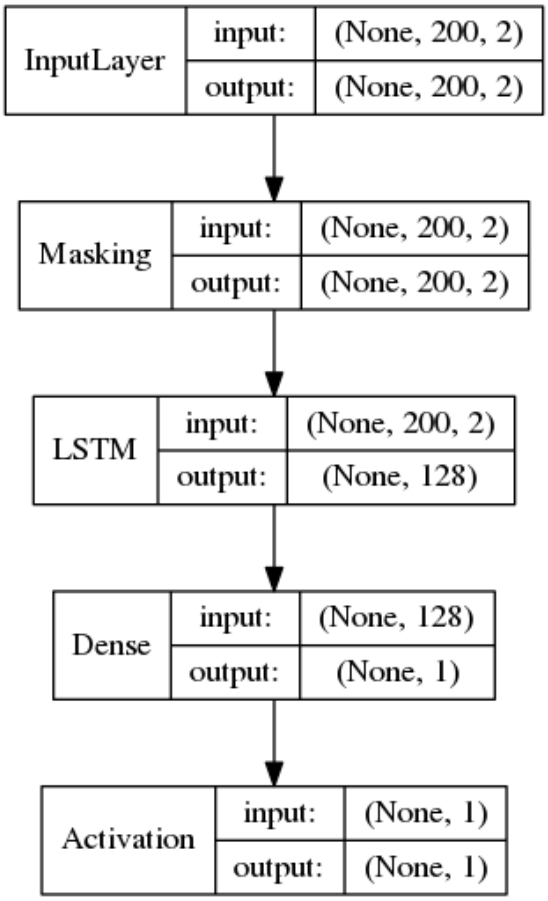


Figure 3.10: *LSTM* Neural Network Structure. Source - (Iriya et al. (2020)).

(i.e. the x and y velocity sequence). We performed leave-one-out cross validation (each trajectory took turns being left out of the model and used for validation), and tried 3 different models:

- Estimating the x and y parameters with 2 independent networks considering x and y random variables with different distributions.
- Estimating the x and y parameters with 2 independent networks considering x and y independent and identically distributed random variables (i.i.d.).

- Estimating x and y jointly in a single network whose output is a vector with two real numbers.

All these networks have a similar structure as those from Fig. 3.10 but use sequence length of 20, 1 $LSTM$ layer of dimension 32, batch size of 8, the RMSprop optimizer (Ruder (2016)), linear activation and mean squared error (MSE) as the loss function. Results on Table 3.3 show the best results were obtained for $LSTM$ with independent X an Y and different distributions. This method presented smaller average MSE over all tested trajectories and smaller maximum error than the physical model that uses Newton's traditional equations (Eq. 3.1). This reveals this approach's potential to be used in the a priori Kalman estimate and other future studies.

3.6 Conclusion

We have developed an optical imaging method to track bacteria, identify changes on motion patterns due to antibiotic activity, and obtain the MIC for different antibiotics. We detected motion differences with four different antibiotic classes and generated MIC values similar to $CLSI$ standards in 30-150 minutes. We also developed image processing algorithms for robust cell segmentation and tracking, integrated the algorithms with state-of-the-art $LSTM$ networks, and designed a $LSTM$ network to predict bacterial trajectories. The present method focuses on tracking active E. coli cells via motion patterns, naturally filtering out inactive cells or impurities in the sample and improving AST accuracy. The $LSTM$ model can also predict bacterial cell trajectories from a sequence of previous positions with accuracy much better than traditional approaches. This capacity could further advance understanding of bacterial physiological responses and environmental adaptation. Future work includes extending the present study to clinical samples, where bacterial concentrations are

Method	MSE	Maximum Error
Physical model - X	0.941	8.882
Physical model - Y	0.950	7.898
Physical model - X and Y iid	0.946	8.883
Physical model - joint X and Y	1.402	9.019
$LSTM$ - X	0.492	3.648
$LSTM$ - Y	0.474	4.377
$LSTM$ - X and Y iid	0.498	7.979
$LSTM$ - joint X and Y	0.896	5.002

Table 3.3: Comparison of Different Methods for Estimating the Next Cell Position From a Sequence of Previous Positions, Showing the Mean Squared Error (MSE) and Maximum Error. Results Show Better Results for $LSTM$ with Independent X and Y with Different Distributions.

low, in the order of $10^3 - 10^5$ colony forming units/mL (Davenport et al. (2017)), and impurities are high. In this scenario, the $LSTM$ algorithm could be modified and also used for bacterial identification to discriminate between bacterial cells and other particles. Finally, it became clear the limitations of the proposed $LSTM$ networks in modeling changes for bacteriostatic antibiotics. In this context, cell counting appears as the most effective feature. The next chapter aims at identification of bacterial cells in low concentration samples, which could boost the cell counting performance in such scenarios.

Chapter 4

DEEP LEARNING LARGE VOLUME MICROSCOPY BACTERIAL IDENTIFICATION

4.1 Introduction

In the last chapter we proposed an optical AST system based on image processing and deep neural networks ($LSTM$). Although the method showed promising results, it still relies on bacteria growth for bacteriostatic antibiotics. This threatens the system performance under low bacterial concentrations, a common scenario in clinical samples ($\sim 10^4$ CFU/mL) (Schoepp et al. (2017)). If bacteria are somewhat rare in the specimen, it becomes important to correctly identify the bacterial cells for an accurate cell count and if the concentration is too low, enrichment or culturing is required, adding up to the total assay time. Moreover, there is always the possibility of contamination or multiple infecting pathogens, which might make the biological sample not suitable for direct analysis without a pure culture. Nevertheless, in the introductory chapter we discussed how diagnostics is composed of two parts (identification and AST) but so far we have only been studying methods for AST and have not yet addressed the identification part. If an infection can be quickly and accurately diagnosed as viral or bacterial at point of care, the use of unnecessary antibiotics can be avoided, preventing resistance development. Furthermore, if the infecting pathogen can be determined to a strain level, choice of antibiotics can also be narrowed down. Like previously stated in the introductory chapter, the gold standard for urinalysis is culturing, and alternative methods are not as robust, often requiring culturing as a preliminary step for sample enrichment to increase the bacterial concentration. The

same goes for strain identification methods. In this chapter we propose a method for bacteria identification in urine samples, targeting samples with low bacterial concentration. This study is focused on urinalysis and we narrow the problem down to a $UPEC$ vs. urine particles classification. However the proposed algorithm could be extended to more labels, including different bacterial strains. The system uses our developed Large Volume Microscopy (LVM) system (Mo et al. (2019)) which allows very low magnification (1 - 2×) and makes it suitable for the analysis of clinical samples, since the whole volume of the specimen can be observed in a single field of view. We feed single particle videos into a state-of-the-art deep learning model (CNN), which is able to label each single particle in the sample. Working at single-cell level brings the possibility to follow each individual cell's patterns and to come up with conclusions based on statistics. Although deep learning has been explored for bacteria identification (Liang et al. (2018), Hay and Parthasarathy (2018), Quinn et al. (2016)), to our knowledge, this is the first attempt to combine video, light scattering microscopy and deep learning, highlighting the novelty of the proposed approach. The main disadvantages of the method are its difficulty for untrained humans to interpret the original LVM videos, and the black-box nature of the deep learning algorithm, which selects features of difficult interpretation, making several rounds necessary for testing the algorithm's generalization capabilities. However, when comparing results with a more traditional machine learning approach with hand-engineered features, the deep learning approach shows a significant performance increase in accuracy.

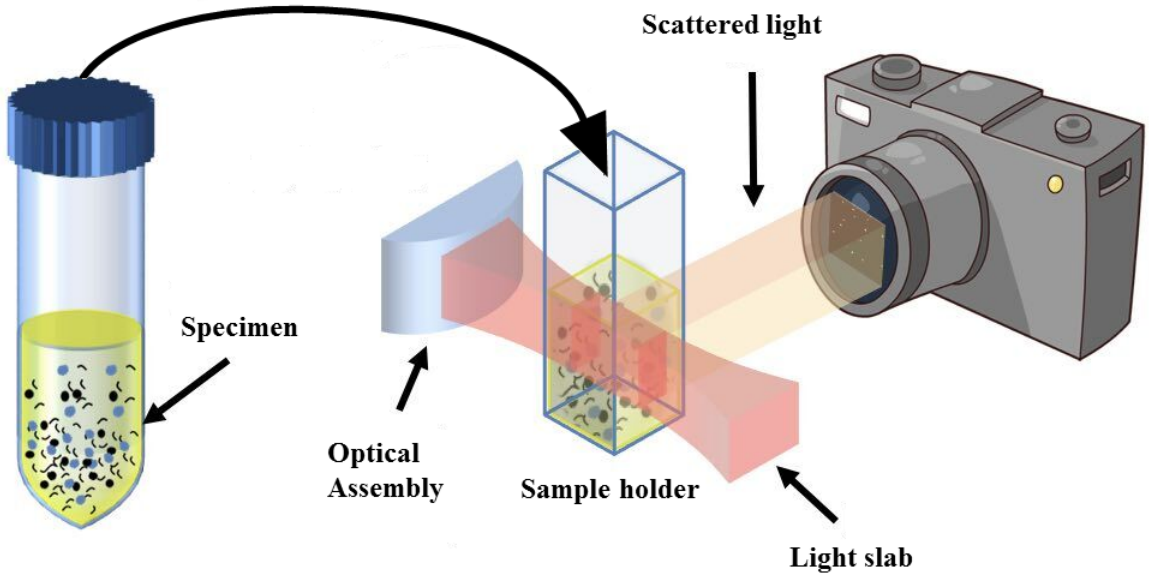


Figure 4.1: Overview of the LVM Setup. A Laser Illuminates the Sample While Side Scattering Images Are Recorded. Source - Modified From (Mo et al. (2019)).

4.2 Discussion

4.2.1 LVM

Fig 4.1 reveals the LVM setup. A cuvette containing a sample specimen is illuminated by a diode laser generating a sequence of side scattering images with wide-view and deep-field depth, which are then recorded with a CMOS camera. Fig 4.2 shows examples of polystyrene beads, E. coli and urine images under the setup. The similarity of the images makes evident the complexity of the problem, as the LVM videos are of difficult interpretation. Particles appear as bright blobs with a 3D Gaussian intensity profile and have a intermittent blinking nature over time, caused by the effect of particle micro-motion on the scattered light. (Fig. 4.3) shows the blinking effect where a particle intensity oscillates between low and high values almost period-

ically while peak and valley values also change over time. The temperature generates a drift in the solution, causing particles to move in a pseudo-circular fashion. The drift slowly varies with space and time, making close particles to move similarly. Fig. (4.4) shows the trajectory of a few bead particles moving by the drift force.

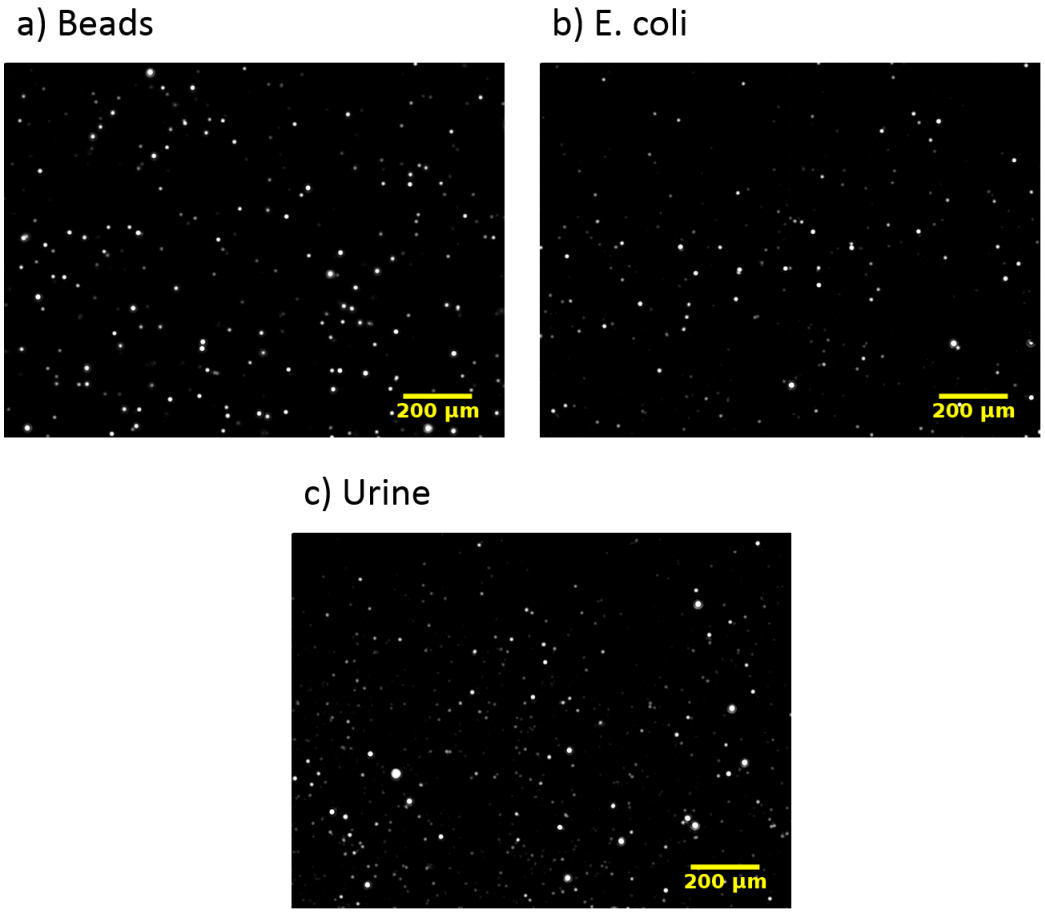


Figure 4.2: Examples of Samples Under the LVM Setup.

4.2.2 Algorithm

The block diagram for the algorithm is depicted on Fig. 4.5. The original LVM video containing a specimen (beads, bacteria, urine) is fed into the particle localization algorithm, generating centroid positions for each frame. The centroids are

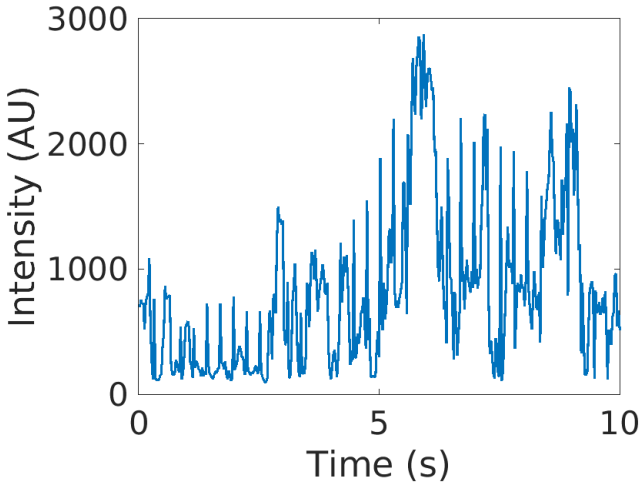


Figure 4.3: Particle Intensity Plot Revealing the Blinking Effect.

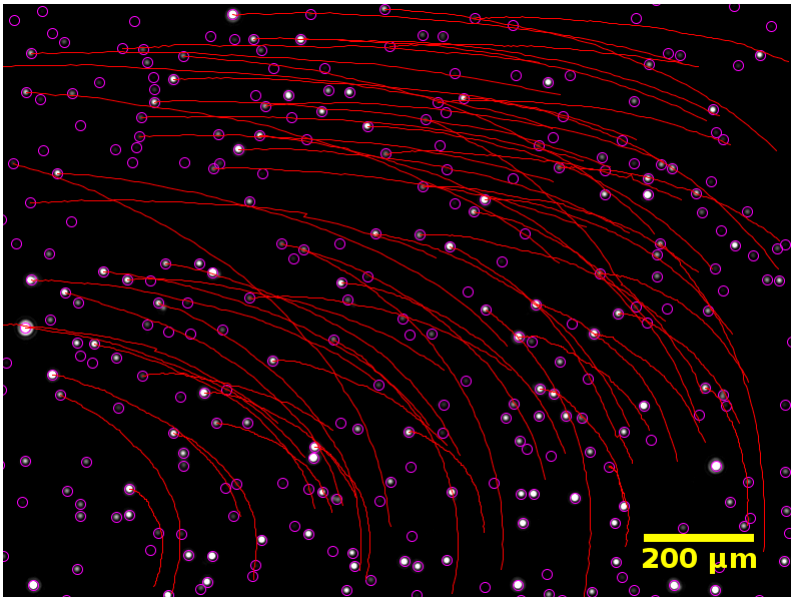


Figure 4.4: Example of Drift Making Particles Move Along Curves. Only a Few Trajectories Are Shown to Avoid Overcrowding the Image.

then connected by the tracking algorithm, to generate particle tracks which are then condensed into new videos, containing single particles. The single particle videos are finally used as inputs to the machine learning algorithm, which will either create a

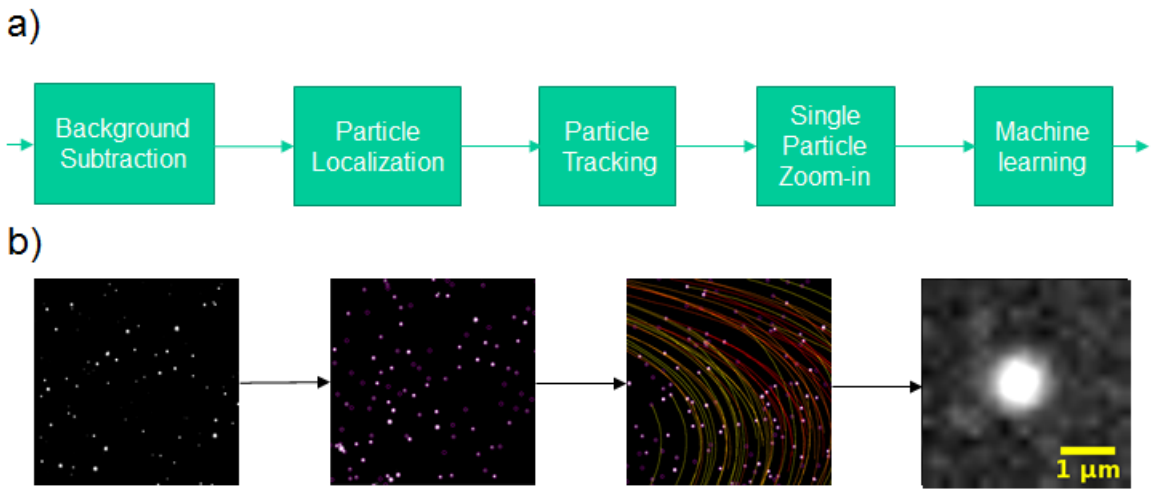


Figure 4.5: a) Block Diagram of the Algorithm Used for Bacterial Identification. After a Localization and Tracking Algorithm, the Original LVM Video Is Transformed and Broken Into Hundreds of Single Particle Videos. The Single Particle Videos Are Used as Inputs for a Machine Learning Classification Model, Which Identifies Particles as Bacteria / Not Bacteria. b) Sequence of Transformations Going from the Original LVM Video to a Single Particle Video.

model from the input data (training phase) or classify the particle into bacteria / not bacteria (validation and test phases). We experimented with separating E. coli from Urine particles as well as from 1 µm polystyrene beads.

Particle Localization

To perform particle localization we used a blob detection algorithm, based on the Scale Invariant Feature Transformation ($SIFT$) (Lowe (2004)). The algorithm works as a form of template matching, since the light scattering setup generates images with particles spatially distributed as Gaussians and the blob detection algorithm computes the convolution of the image with a Laplacian of Gaussian filter. For the

implementation, the software ImageJ (Abràmoff et al. (2004)) was used with the plugin Trackmate (Tinevez et al. (2017)), however we found our own developed tracking algorithm more robust than Trackmate's default algorithms, as we included the drift information to predict the particle motion. Therefore, the particle localization algorithm follows the below steps:

1. Estimate the background and subtracted it from each frame to eliminate residual light scattering. The entire video is divided into long windows containing W_{len} frames. The minimum value for each pixel during this window is used as a background pixel for that window.

2. For each frame, compute particle spots with a base radius R_{pl} by using the blob detection algorithm.

3. Filter out particles with a convolution response (quality on Trackmate) smaller than the threshold Q_t.

   $W_{len} = 600$ frames (15 s at 40 fps), $R_{pl} = 5$ and $Q_t = 10$ were used in this study.

Tracking

To connect the centroids of the blobs detected in the particle localization algorithm, we used a linear Kalman Filter, similar to the one presented on the previous chapter. Most of the details of the previous implementation were kept, including the possibility of missing frames and of tracks to share locations . The parameters $S_r = 6$, $M_t = 50$, $C_t = 100$ were selected in this case. The search radius has been greatly reduced since we are working under a smaller magnification, while M_t and C_t have been boosted due to the blinking nature of spots and the high probability of missing frames. In addition, there are two main differences when comparing the two algorithms:

- Due to the deep-field depth capabilities of the LVM setup, this scenario does not have to handle objects undergoing contrast changes so all of the details regarding contrast changes were removed.

- Particle motion is mainly dominated by drift, so it makes sense to use this information to calculate the particle velocities and predict where a particle should land when moving between adjacent frames.

Since the drift varies slowly in space and time, we estimate the drift by dividing the image into a grid of $g_s \times g_s$ regions, and calculate the drift velocity d_v in each region with a moving average:

$$d_v(t, R) = \alpha d_{avg}(t, R) + (1 - \alpha) d_v(t - 1, R) \tag{4.1}$$

, where R is the index of the current region. To calculate $d_{avg}(t, r)$, we average the difference between the a posteriori position estimates in two adjacent frames (current and previous) over all particles in the same region. Particles in the same region R use the same $d_v(t, R)$ and each particle is assigned the region whose center is the closest (Euclidean distance) to the particle location. In this study we used $g_s = 10$ and $\alpha = 0.2$. Fig. 4.6 shows an example of drift vectors in a frame.

Finally, the a posteriori velocity $v = [v_x, v_y]^T$ estimate for each particle is also updated using a moving average:

$$v(t, p) = \beta d_v(t, R) + (1 - \beta) v(t - 1, p) \tag{4.2}$$

, where p denotes the particle index and R is the region assigned to the particle. We used $\beta = 0.8$ to allow the drift to account for most of the motion.

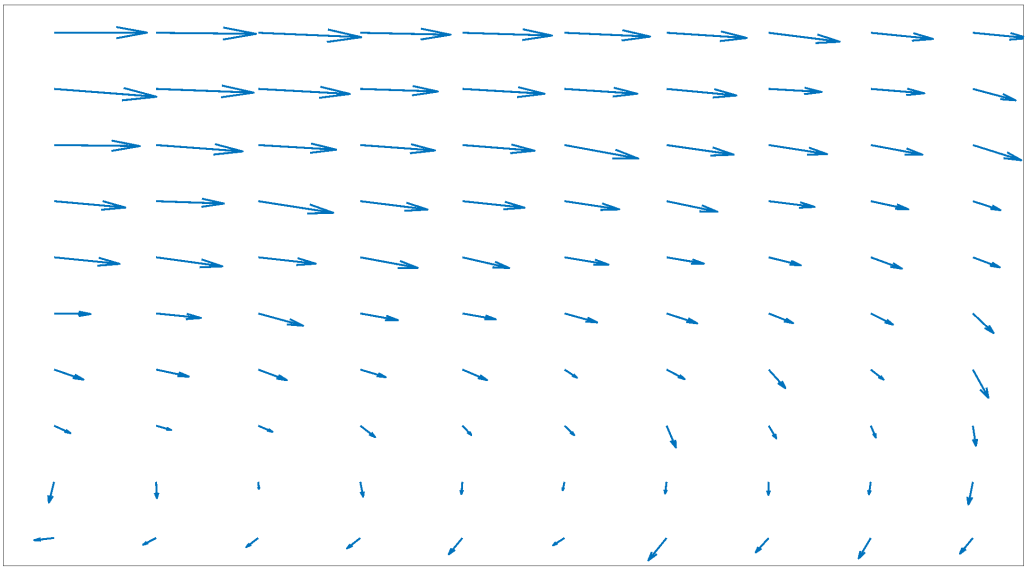


Figure 4.6: Drift Vectors in a Frame Calculated Along a 10 x 10 Grid. Longer Arrows Represent Higher Drift.

Machine Learning

After tracks are built, short tracks with less than M_{dur} frames are eliminated, to discard tracks of faulty tracking, made difficult by intense blinking. Due to the Gaussian nature of the particles, a Full Width at Half Maximum ($FWHM$) filter is also applied to the first frame of all tracks to ignore particles that are out of focus. This way, only particles with $FWHM < T_{FWHM}$ (5 in this study) are kept, to select in focus particles with higher intensities and lower width. Finally, the good tracks that pass both filters are used to reconstruct new videos of single particles, where the particle is centered in each frame. This is done by zooming-in the original (background subtracted) LVM video at the particle centroid in each frame and cropping a region of c_s $\times$ c_s pixels. We used $M_{dur} = 650$ frames to only consider particles that last more than half of the entire LVM video (the total video duration is 1200 frames or 30s at 40

fps) and avoid having the same track generate more than one video, in case it is split due to a faulty tracking. $c_s = 12$ was selected to minimize the background pixels (the blob diameter size was selected as 10 pixels). These videos discard the motion information, which was considered irrelevant since the drift dominates the motion, making it a noisy feature. We frame the machine learning system as a classification problem with two classes: E. coli / not E. coli. We compared results using two different approaches, traditional machine learning and deep learning. The difference between the former and the latter relies mostly on the way features (important characteristics that can distinguish different classes) are extracted. On traditional machine learning, features are hand-engineered using previous knowledge of the problem, so intuitive characteristics like intensity, size, shape, etc, are usually combined with statistics and used as features. On the other hand, deep learning uses artificial neural networks to automatically extract optimal features that can distinguish the classes. The major drawback is that often times the features are hard to interpret and the system ends up working as a black box. However since Alexnet (Krizhevsky et al. (2012)), deep learning systems have gained increased popularity in computer vision tasks due to their superior accuracy performance.

Traditional Machine Learning

For each single particle video, we extracted hand-engineered features that combine both spatial and temporal information, starting with four spatial features:

- Average particle intensity.
- Particle intensity standard deviation.
- Particle area.
- Particle quality ($SIFT$ response).

From these initial spatial features, we obtain time series by concatenating the information from all frames. Temporal information is then added by calculating statistics from the time series, which include mean, standard deviation, kurtosis, skewness, first and third quartiles, for all spatial features. Following common practice in traditional machine learning systems, especially for 1-dimensional signals such as speech (Iriya and Ramírez (2014)), first and second derivatives of all features and their statistics were also included to add more temporal information. In addition, as the blinking behavior is also an important cue related to the shape of the particles, we added some features related to this behavior. Therefore, the percentage of missing frames, the average distance between detections (non-missed frames) and the average intensity peak distance were also added. Table 4.2 shows all 93 hand-engineered features tested in the study.

Many of those features are extremely correlated and some might be irrelevant. For this reason, we apply the Sequential Forward Selection (SFS) algorithm(Kumar and Minz (2014)) a greedy search algorithm that minimizes the number of used features. All models were trained with Support Vector Machines (SVM) (Weston and Watkins (1998)), using radial basis function (RBF) kernels. SVM's were chosen for their ability to find optimal separation hyperplanes in binary classification problems (Weston and Watkins (1998)).

Deep Learning

The deep learning system should also extract both spatial and temporal features from the single particle videos. Our first attempt was to follow the idea proposed in (Donahue et al. (2015)) and use a CNN to extract spatial features and combine those features using a $LSTM$ to extract temporal features (CNN-$LSTM$ model). We also added the attention concept (Wang et al. (2016)) to make sure the network uses

MeanPercentMissingFrames	KurtStdIntensity	1stDerivKurtQuality
MeanPeakDist	KurtQuality	2ndDerivMeanCenterIntensity
MeanDetectionRate	1stDerivMeanCenterIntensity	2ndDerivMeanArea
MeanCenterIntensity	1stDerivMeanArea	2ndDerivMeanAvgIntensity
MeanArea	1stDerivMeanAvgIntensity	2ndDerivMeanStdIntensity
MeanAvgIntensity	1stDerivMeanStdIntensity	2ndDerivMeanQuality
MeanStdIntensity	1stDerivMeanQuality	2ndDerivStdCenterIntensity
MeanQuality	1stDerivStdCenterIntensity	2ndDerivStdArea
StdCenterIntensity	1stDerivStdArea	2ndDerivStdAvgIntensity
StdArea	1stDerivStdAvgIntensity	2ndDerivStdStdIntensity
StdAvgIntensity	1stDerivStdStdIntensity	2ndDerivStdQuality
StdStdIntensity	1stDerivStdQuality	2ndDerivPctl25CenterIntensity
StdQuality	1stDerivPctl25CenterIntensity	2ndDerivPctl25Area
Pctl25CenterIntensity	1stDerivPctl25Area	2ndDerivPctl25AvgIntensity
Pctl25Area	1stDerivPctl25AvgIntensity	2ndDerivPctl25StdIntensity
Pctl25AvgIntensity	1stDerivPctl25StdIntensity	2ndDerivPctl25Quality
Pctl25StdIntensity	1stDerivPctl25Quality	2ndDerivPctl75CenterIntensity
Pctl25Quality	1stDerivPctl75CenterIntensity	2ndDerivPctl75Area
Pctl75CenterIntensity	1stDerivPctl75Area	2ndDerivPctl75AvgIntensity
Pctl75Area	1stDerivPctl75AvgIntensity	2ndDerivPctl75StdIntensity
Pctl75AvgIntensity	1stDerivPctl75StdIntensity	2ndDerivPctl75Quality
Pctl75StdIntensity	1stDerivPctl75Quality	2ndDerivSkewCenterIntensity
Pctl75Quality	1stDerivSkewCenterIntensity	2ndDerivSkewArea
SkewCenterIntensity	1stDerivSkewArea	2ndDerivSkewAvgIntensity
SkewArea	1stDerivSkewAvgIntensity	2ndDerivSkewStdIntensity
SkewAvgIntensity	1stDerivSkewStdIntensity	2ndDerivSkewQuality
SkewStdIntensity	1stDerivSkewQuality	2ndDerivKurtCenterIntensity
SkewQuality	1stDerivKurtCenterIntensity	2ndDerivKurtArea
KurtCenterIntensity	1stDerivKurtArea	2ndDerivKurtAvgIntensity
KurtArea	1stDerivKurtAvgIntensity	2ndDerivKurtStdIntensity
KurtAvgIntensity	1stDerivKurtStdIntensity	2ndDerivKurtQuality

Table 4.2: Hand-engineered Features Tested for the Traditional Machine Learning Approach.

features from different parts of the time series. However we found our $CNN\text{-}LSTM$ model to easily overfit, which is a known problem for RNN's (Zaremba et al. (2014)), leading us to look for a different model. Motivated by the results on the YouTube-8M benchmark (Abu-El-Haija et al. (2016)), we implemented a simpler model, $CNNFA$ (CNN with feature average), which averages the features obtained from the CNN on each frame. The CNN base network is a Resnet-50 (He et al. (2016)) pretrained on imagenet (Deng et al. (2009)), with the classification layer removed. The structure of the network is shown in Fig. 4.7. All models were trained using a cross-entropy loss.

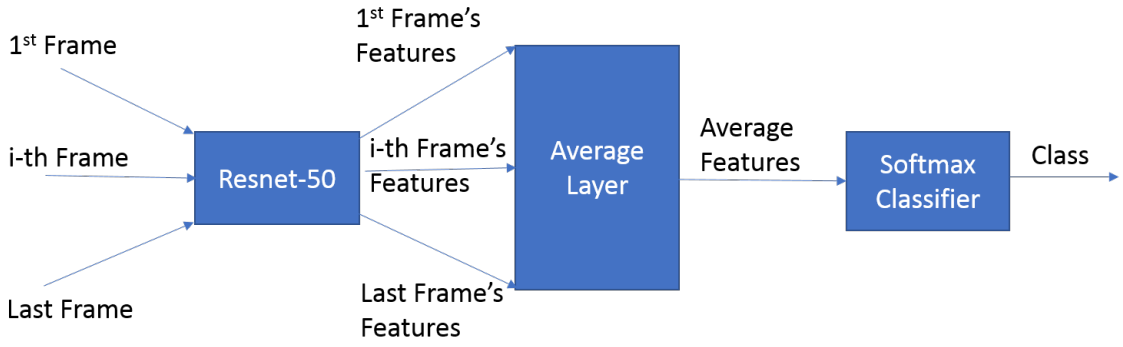


Figure 4.7: Structure of the $CNNFA$ Network.

We found a few implementation details to be extremely important for the robustness of the models:

- We performed mean subtraction on all single particle videos, by calculating a scalar averaged first over all pixels and then over all frames, and then subtracting this scalar from all pixels in the video. This increased the accuracy up to 5% in some cases.

- L2-norm regularization ($\lambda = 0.01$) (Zeng et al. (2018)) and dropout (0.5) (Krizhevsky et al. (2012)) were important to avoid overfitting and guarantee validation loss convergence.

- Due to a huge difference in the average intensity values for the background (close to 0) and the particles (0 - 65535), we found important to place a cap on the maximum value (1000), then normalize all intensity values between 0-1. 0 values were also replaced with the minimum non-0 value throughout each video. This dynamic range adjustment lead to a better loss convergence.

- Small learning rates lead to better validation loss convergence while high learning rates made validation loss quickly start to increase indefinitely and generate oscillating accuracy curves over epochs.

- The length of the input videos has a great effect on the learning capabilities. Short tracks do not present enough information to train robust models.

- Class balancing was enforced by limiting the number of training samples in each class to the maximum number of samples of the class with least samples. Samples were randomized in each epoch, to increase the odds that samples left out of one epoch are used to train the model in different epochs.

4.2.3 Results

Datasets

As mentioned previously, we framed the identification task as a binary classification problem, where we worked with 2 separate classifications:

1. E. coli vs. 1 µm polystyrene beads.

Day	1	2	3	4
Train		x	x	
Val	x			
Test				x

Table 4.3: Dataset for E. coli vs. Beads Classification, Containing Data from 4 Days, Where Each Day Was Once Left Out of Training and Used as Validation (in This Example Day 1 Was Used for Validation). Day 4 Was Used as Test.

2. E. coli vs. urine particles.

We started with E. coli vs. beads since it is a relatively easier problem. Particles are distinct when inspecting the LVM videos by the naked eye, as polystyrene beads appear brighter, bigger and do not present accentuated blinking. We believe this is a consequence of the round nature of the particles. Since no ground truth can be obtained when mixing samples of different types, we work with separate specimens for each class, and we assume all the particles in one video belong to that class. Table 4.4 shows the dataset used to train, test and validate the models. We utilized data from 4 days of experiments. Each day has different samples (specimens) for each class and each sample generated replicates, with multiple videos recorded from different cuvettes. At least 4 different replicates were used for each sample, generating one video per replicate. We performed leave-one-day-out cross validation for the 3 first days, and separated the last day completely for test. In other words, a different model was trained for each day, where all its samples were left out of the training phase and used for validation.

Next, we tried the same leave-one-day-out cross validation approach for the E. coli vs. urine classification problem, however generalization results (validation and

test) were not satisfactory (under 50% accuracy). We then investigated the problem looking for the main reason for the poor performance, which we concluded to be a great data variability from urine sample to urine sample. We created 3 different datasets with different levels of generalization difficulty:

1. Data from a single day and a single sample, leaving the first replicate for validation.

2. Data from the same single day, leaving the first sample for validation.

3. Data from 6 days, leaving the first sample from each day for validation.

Table 4.4 summarizes the datasets created for the E. coli vs. urine problem. Results point the generalization performance to be related to the amount of different samples used for training, as we will see in the next sections.

Accuracy Performance

Results for the E. coli vs 1 µm polystyrene beads classification are shown in Table 4.5. The deep learning method using the $CNNFA$ network shows excellent results, with over 90% accuracy (averaged over the two classes) for training and validation, while test accuracy is slightly lower. Test results were calculated using the median class (most voted) of the classification from all models created on the cross validation. Comparing to the SVM approach, the best result using SFS shows a 20% worse accuracy (averaged over the two classes) for validation, and even the training results show a lower performance. This highlights the difficulty in finding out meaningful features with the traditional approach.

Results for the E. coli vs Urine classification using the $CNNFA$ method are shown in Table 4.6. This task was way more difficult, as the models seem to struggle

a)

Day	3							
Sample	1				2			
Replicate	1	2	3	4	1	2	3	4
Train		x	x	x				
Val	x							
Test					x	x	x	x

b)

Day	1	2	3				4				5				6				7			
Sample	1	1	1	2	3	4	1	2	3	4	1	2	3	4	1	2	3	4	1	2	3	4
Train				x	x	x																
Val			x																			
Test																			x	x	x	x

c)

Day	1	2	3				4				5				6				7			
Sample	1	1	1	2	3	4	1	2	3	4	1	2	3	4	1	2	3	4	1	2	3	4
Train	x	x		x	x	x		x	x	x		x	x	x		x	x	x				
Val			x				x				x				x							
Test																			x	x	x	x

Table 4.4: Datasets for E. coli vs. Urine Classification. a) Dataset 1 Containing Data from a Single Day Where One Replicate Was Used for Validation and a Different Sample Was Used for Test. b) Dataset 2 Containing Data from a Single day Where Sample 1 Was Used for Validation and a Different Day Was Used for Test. c) Dataset 3 Containing Data from 7 Days, Where Sample 1 from Each Day Was Used for Validation and a Different Day Was Used for Test.

Method	E. coli Classification (%)			Beads Accuracy (%)		
	Train	Validation	Test	Train	Validation	Test
SVM	52	53	93	96	90	75
$CNNFA$	97	93	95	94	89	78

Table 4.5: Accuracy Performance of E. coli vs. 1 µm Polystyrene Beads Classification. The $CNNFA$ Method Shows a 20% Validation Accuracy Increase Compared to the SVM Method.

Dataset	E. coli Classification Accuracy (%)			Urine Classification Accuracy (%)		
	Train	Validation	Test	Train	Validation	Test
1	100	93	56	98	92	85
2	89	95	84	62	61	40
3	64	75 (74)*	63	89	82 (82)*	60

Table 4.6: Accuracy Performance of E. coli vs. Urine Classification Using the $CNNFA$ Method for the 3 Datasets. For Dataset 3, the Numbers Marked with "*" Show the Results Using the Same Validation Data from Dataset 2, for Comparison.

in learning patterns from different samples. For dataset 1, with all data from the same sample, training and validation show excellent results, however when a different sample is used for test the performance drops significantly. Similarly, dataset 2 has trouble generalizing as a different sample is used for validation, revealing the model has problems generalizing to a new sample. However, the overall accuracy increases when more data is introduced on dataset 3, reinforcing the conclusion that the sample variability is the biggest challenge in training a robust model.

Method	E. coli Accuracy (%)			Urine Accuracy (%)		
	Train	Validation	Test	Train	Validation	Test
SVM	78	74	79	62	57	50
$CNN\text{-}LSTM$	77	89	80	57	46	21
$CNNFA$	64	75	63	89	82	60

Table 4.7: Comparison of SVM, $CNN\text{-}LSTM$ and $CNNFA$ on Dataset 3. The $CNNFA$ Method Shows a 13% Validation Accuracy Increase Compared to the SVM Method, and Both are Much More Accurate than the $CNN\text{-}LSTM$ Method.

Figure 4.8 shows the training and validation losses for all problems evaluated. The beads dataset and dataset 1 for urine converge very well, as they are easier problems. Comparing datasets 2 and 3, we can see that the loss function converges more properly on the larger dataset, demonstrating how the model learns to represent the sample variability as more data is introduced.

Method Comparison

We used dataset 3 for the E. coli vs urine problem to compare the performance of SVM, $CNN\text{-}LSTM$ and $CNNFA$ models. The overall classification accuracy for $CNNFA$ is much higher than $CNN\text{-}LSTM$, as shown in table 4.7 and the validation loss shows a better learning capacity as it learns faster and reaches a lower minimum (fig. 4.9). When comparing $CNNFA$ and SVM, once again the training capabilities of $CNNFA$ outperforms the SVM method, with a 13% accuracy increase in validation.

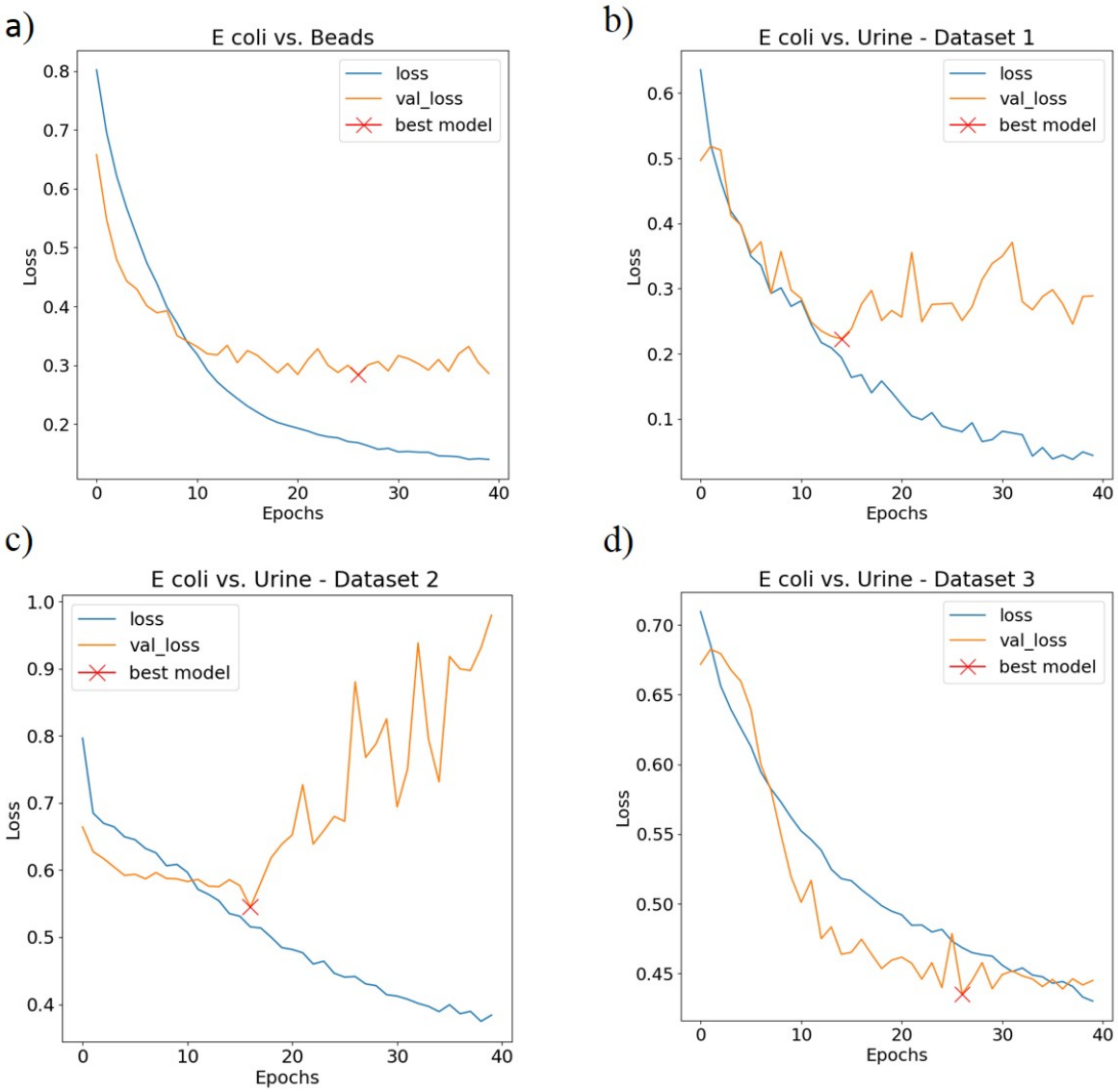


Figure 4.8: Learning Curves for the Trained Datasets. a) Beads Dataset. b) Urine Dataset 1. c) Urine Dataset 2. d) Urine Dataset 3.

Effect of Dynamic Range Adjustment

To show how the dynamic range adjustment affects the results, we compare different intensity caps on Fig. 4.10. The dataset used on this case was a single day E.coli vs Beads. We can see that higher caps result in an unstable validation accuracy

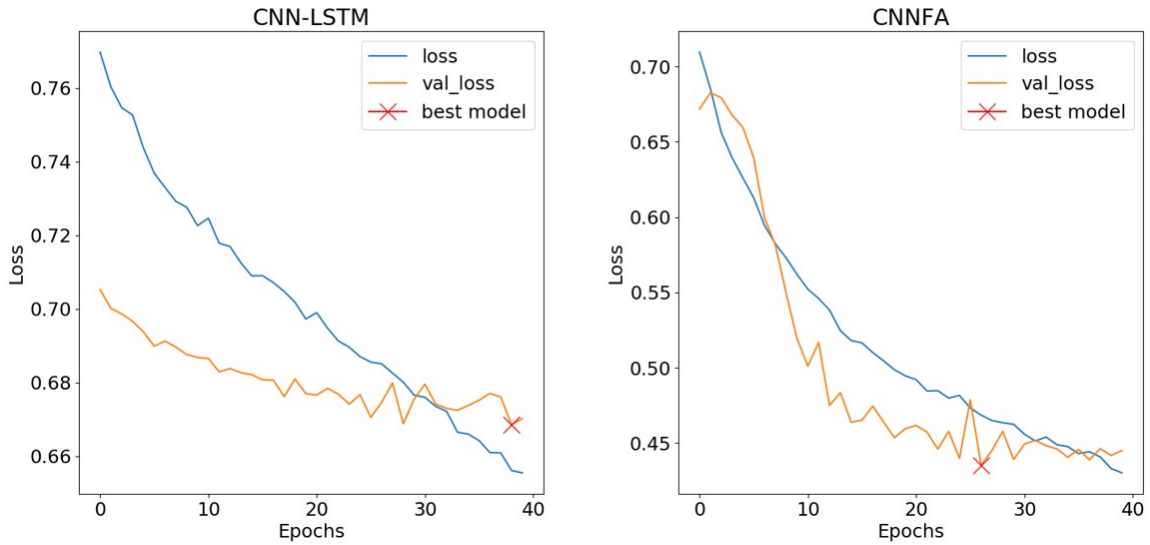


Figure 4.9: Learning Curves for $CNN\text{-}LSTM$ and $CNNFA$ on Dataset 3.

over the epochs which oscillate within a range of $\sim 30\%$. Therefore, dynamic range adjustment can increase accuracy performance up to 30%.

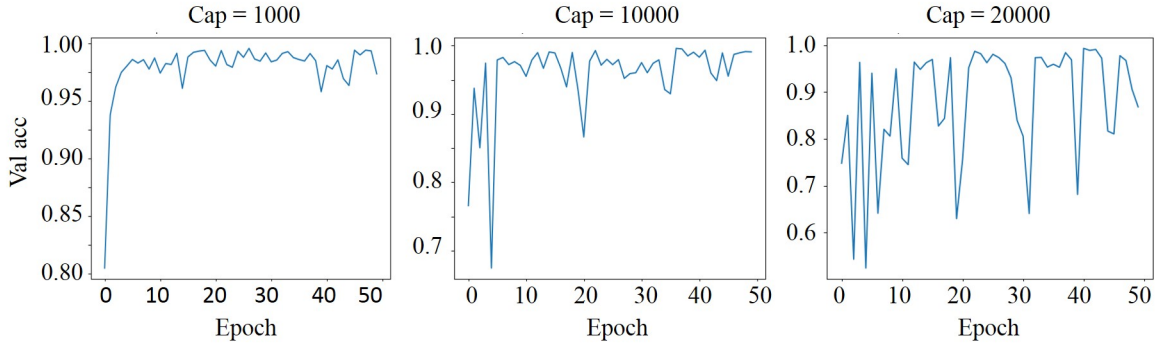


Figure 4.10: Comparison of the Effect of Different Intensity Caps on the Accuracy. Higher Caps Result in an Unstable Validation Accuracy over the Epochs.

Effect of Video Length

We analyzed the effect of the video length on the $CNNFA$ method. As we see on Fig. 4.11, although the best accuracy differs only by 3%, a short duration of 2.5 s resulted in poor learning as the validation loss function oscillates over epochs, while increasing the video duration to 12.5 s ensures a better convergence. This leads to the conclusion that short tracks do not possess enough information to represent the particle's intensity variability. To obtain 12.5 s videos, the first 500 frames from each particle track are time averaged every 5 frames, generating an input sequence of length 100. Time averaging decreases the amount of input data, making training easier.

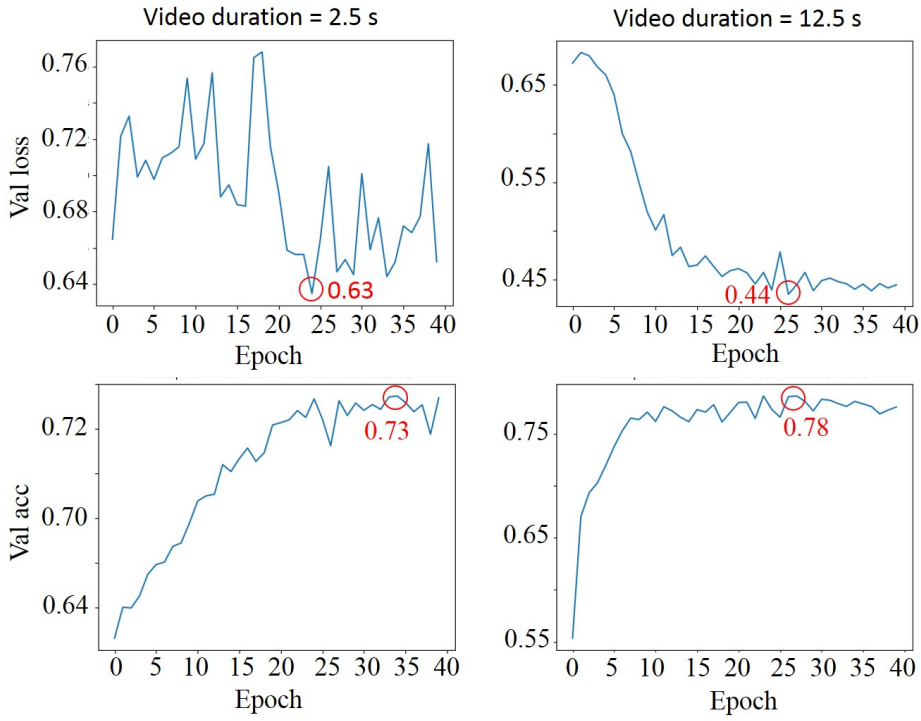


Figure 4.11: Comparison of the Effect of the Video Duration. A Longer Duration Results in a Better Validation Loss Convergence. Minimum and Maximum values are Circled and Shown in Red.

Effect of Setup Configuration

In order to ensure the generalization capabilities of the algorithm, we must assess the effect of the setup configuration on the model. To test the effect of different setup configurations, we trained the model with the default setup configuration, then tested it on different configurations where we modified the following parameters:

1. Camera position in X (focus), Y, Z planes.
2. Laser position in X, Y, Z, planes.
3. Digital controlled field of view (center, top left and bottom right).
4. Turning the lights off.

The same sample was used with 4 replicates (cuvettes / videos) in all configurations. On previous results we observed how training and testing with the same samples should generate similar results for training and test. Thus, we conclude the discrepant results were a consequence of the setup modifications. Table 4.8 shows the results for different setup configurations. We notice most parameters did not significantly affect the results, with the exception of the digital field of view and the camera position in the X plane, which changes the focus of setup. This highlights the importance of keeping those parameters unchanged between experiments, otherwise the trained models will be inconsistent.

4.3 Materials and Methods

4.3.1 LVM Imaging

Fig. 4.12 shows the *LVM* setup an it's components. The setup is composed of a 100 mW, 808 nm fiber-coupled diode laser (OBIS 637-100FP, Coherent Inc., USA)

Condition	E coli Acc (%)	Urine Acc (%)
Default (Training)	81	72
Laser Z (-10)	79	74
Laser Y (+20)	79	73
Laser Y (-10)	81	79
Laser X (+20)	80	74
Laser X (-10)	79	76
Cam Z (+10)	79	77
Cam Z (-10)	76	79
Cam Y (+20)	60	82
Cam Y (-10)	61	84
Lights Off	59	86
Field of view bottom-right	77	76
Cam X (+20)	**44**	**77**
Cam X (+10)	**47**	**53**
Cam X (-10)	**59**	**88**
Field of view top-left	**36**	**90**

Table 4.8: Results of Training the Model with a Default Setup Configuration and Testing Using Different Configurations. Changing the Camera Position on the X Plane (Focus) and the Digital Field of View Significantly Affect the Results.

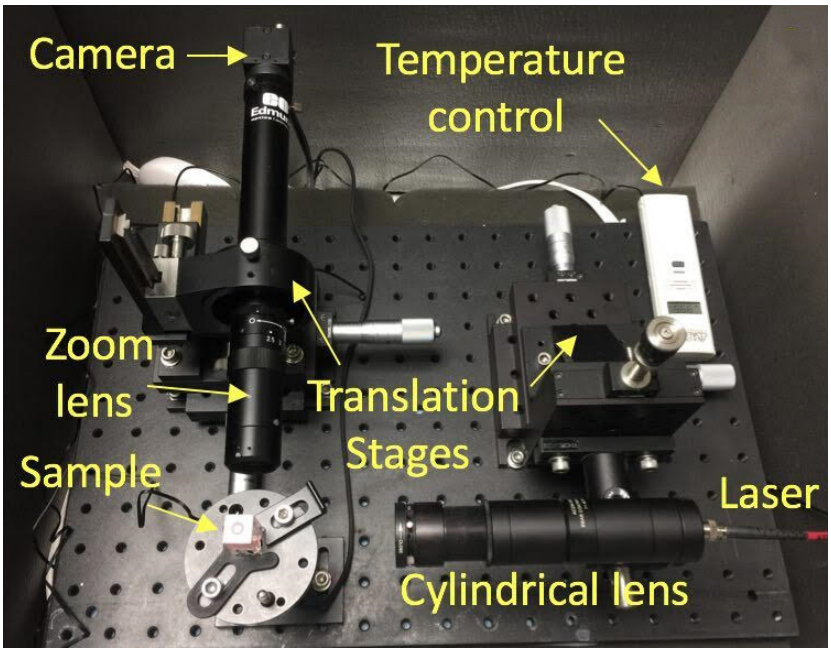


Figure 4.12: LVM Setup and Its Components. The Lens in the Photo Has Been Substituted (See LVM Imaging Description).

with a collimation lens and a cylindrical lens (Thorlabs Inc., USA) to focus the laser beam into a light slab through the sample. Side scattering images were recorded by a CMOS camera (Flea3 FL3-U3-13S2M, Point Gray Research Inc., Canada) for 30 seconds at a 800×600 pixel resolution and 40 fps through a 12× variable zoom lens (NAVITAR 12×, Navitar, USA - different from the one shown in the photo) placed at a 90° angle to the laser light beam. The image volume was determined by the size of the light slab that illuminated the sample and by the viewing size and focal depth of the optics. For the described in this study, the viewing volume of 1.85 mm × 1.4 mm × 0.7 mm was equivalent to 1.81 µL at 2× magnification.

4.3.2 Sample Preparation

Uropathogenic E. coli ATCC25922 were purchased from American Type Culture Collection (ATCC) and stored at -80 °C in 5% glycerol. E. coli were cultured overnight

($\sim$16 h) at 35 °C into LB and then for additional $\sim$ 2 h at 35 °C to an $OD600$ of $\sim$0.7, which corresponded to $(5-6)\times10^8$ cells/mL. After dilution to appropriate cell concentrations, PBS 1$\times$ was added to the E. coli suspensions. 1 µm polystyrene beads were purchased from Bangs Laboratories, Inc and suspended in PBS 1$\times$. Pooled, healthy human urine purchased from BioereclamationIVT (Lot number: BRH1311635) was filtered using 5 µm syringe filters and then diluted 10$\times$. Samples were diluted to a concentration of approximately 10^5 particles/mL or until less than 1000 particles (counted using the particle localization algorithm) were visible in the field of view. Finally, volumes of 1.81 µL from the final dilutions were distributed in the cuvettes for the experiments.

4.3.3 Data Processing

The LVM videos were processed using ImageJ (Trackmate) and custom MATLAB and Python programs, using the methods discussed throughout this chapter.

4.3.4 Deep Learning

The networks described in this chapter were trained using the Keras framework (Chollet et al. (2015)) with the Tensorflow backend (Abadi et al. (2016)). Images were resized to 20×20 pixels and models were trained for 40 epochs, using the Adam optmizer, batch size of 32 and the learning rate was chosen depending on the problem, varying from $10^{-7}-10^{-5}$, as some datasets required a smaller learning rate to converge properly.

4.4 Conclusion

We proposed a deep learning algorithm for classification problems using the LVM system. We evaluated the algorithm on two problems, E.coli vs polystyrene beads

and E. coli vs urine, obtaining promising results. The algorithm outperforms the classification accuracy of an SVM-based traditional machine learning by 13% for urine and by 20% for beads, and we attribute this gain to its potential in extracting good features from videos. Although different architectures and other improvements to prevent overfitting can be implemented, we conclude the main challenge comes from the sample variability, so training with a larger dataset should be the first step in refining the solution. We anticipate that the developed algorithm can also be used for other classification tasks, for example identifying two or more different types of bacteria for strain identification, as long as comprehensive datasets are designed for the task at hand. Finally, when moving from spiked samples to clinical samples, a similar training procedure can be used, however it is expected that even higher variability is encountered, so training with a large dataset of negative samples will be extremely important to create robust models for urine particles. In addition, until the model is robust enough, a secondary validation method (e.g. fluorescent biomarkers) will be necessary to evaluate the performance of the model on mixed samples.

Chapter 5

CONCLUSION

We have developed three projects regarding novel methods for AST and bacteria identification using computer vision methods. The first two projects show potential as novel methods for AST, being able to obtain results within a window of 30 min to 3 hours, a much faster time frame than the gold standard approach based on cell culture. However they were performed under high bacterial concentration and we highlight the importance of cell growth as the main feature for AST and the need for an easy-to-use solution, which does not require cell immobilization, pre-culture or enrichment. The developed LVM system provides a good alternative for POC, as tests can be run directly on biological clinical samples, with the help of a deep learning system to perform bacteria identification, while the ideas from the first two projects could be combined with the method presented on ((Mo et al. (2019))) to detect growth and establish AST. In this scenario the proposed identification system also allows a more robust cell counting. With a powerful computational system composed of a group of fast CPU's and GPU's, going through all image processing algorithms and classifying a new sample only takes a few minutes, being much faster than the current cell culturing methods, which might take days. Even though deep learning algorithms may take a long time to train, this step can be done offline and only needs to be done once, or at least until the model is robust enough, so it does not need any extra training. Although further research is still necessary to implement a robust POC solution, the methods developed in this study bring us one step closer to the goal of establishing more efficient diagnostics, preventing antibiotic misuse and halting the bacteria resistance problem.

REFERENCES

Abadi, M., Barham, P., Chen, J., Chen, Z., Davis, A., Dean, J., Devin, M., Ghemawat, S., Irving, G., Isard, M., et al., 2016. Tensorflow: A system for large-scale machine learning, in: 12th {USENIX} Symposium on Operating Systems Design and Implementation ({OSDI} 16), pp. 265–283.

Abràmoff, M.D., Magalhães, P.J., Ram, S.J., 2004. Image processing with imagej. Biophotonics international 11, 36–42.

Abu-El-Haija, S., Kothari, N., Lee, J., Natsev, P., Toderici, G., Varadarajan, B., Vijayanarasimhan, S., 2016. Youtube-8m: A large-scale video classification benchmark. arXiv preprint arXiv:1609.08675 .

Amsler, C.D., 1996. Use of computer-assisted motion analysis for quantitative measurements of swimming behavior in peritrichously flagellated bacteria. Analytical biochemistry 235, 20–25.

Andreini, P., Bonechi, S., Bianchini, M., Garzelli, A., Mecocci, A., 2016. Automatic image classification for the urinoculture screening. Computers in biology and medicine 70, 12–22.

Angus, D.C., Linde-Zwirble, W.T., Lidicker, J., Clermont, G., Carcillo, J., Pinsky, M.R., et al., 2001. Epidemiology of severe sepsis in the united states: analysis of incidence, outcome, and associated costs of care. Critical Care Medicine-Baltimore-29, 1303–1310.

Beucher, S., 1979. Use of watersheds in contour detection, in: Proceedings of the International Workshop on Image Processing, CCETT.

Bonura, A., Corinti, S., Schiavi, E., Giacomazza, D., Gianguzza, F., Di Felice, G., Colombo, P., 2013. The major allergen of the p arietaria pollen contains an lps-binding region with immuno-modulatory activity. Allergy 68, 297–303.

Boulos, L., Prevost, M., Barbeau, B., Coallier, J., Desjardins, R., 1999. Live/dead® baclight™: application of a new rapid staining method for direct enumeration of viable and total bacteria in drinking water. Journal of microbiological Methods 37, 77–86.

van den Broek, D., Keularts, I.M., Wielders, J.P., Kraaijenhagen, R.J., 2008. Benefits of the iq200 automated urine microscopy analyser in routine urinalysis. Clinical chemistry and laboratory medicine 46, 1635–1640.

Burdett, I., Murray, R., 1974. Electron microscope study of septum formation in escherichia coli strains b and b/r during synchronous growth. Journal of bacteriology 119, 1039–1056.

CDC, 2013. Antibiotic resistance threats in the United States, 2013. Centres for Disease Control and Prevention, US Department of Health and Human Services.

CDC, 2019. Antibiotic resistance threats in the United States, 2019. Centres for Disease Control and Prevention, US Department of Health and Human Services.

Chatzigeorgiou, K.S., Sergentanis, T.N., Tsiodras, S., Hamodrakas, S.J., Bagos, P.G., 2011. Phoenix 100 versus vitek 2 in the identification of gram-positive and gram-negative bacteria: a comprehensive meta-analysis. Journal of clinical microbiology 49, 3284–3291.

Chiang, Y.L., Lin, C.H., Yen, M.Y., Su, Y.D., Chen, S.J., Chen, H.f., 2009. Innovative antimicrobial susceptibility testing method using surface plasmon resonance. Biosensors and Bioelectronics 24, 1905–1910.

Cho, J., Lee, K., Shin, E., Choy, G., Do, S., 2015. How much data is needed to train a medical image deep learning system to achieve necessary high accuracy? arXiv preprint arXiv:1511.06348 .

Choi, J., Jung, Y.G., Kim, J., Kim, S., Jung, Y., Na, H., Kwon, S., 2013. Rapid antibiotic susceptibility testing by tracking single cell growth in a microfluidic agarose channel system. Lab on a Chip 13, 280–287.

Choi, J., Yoo, J., Lee, M., Kim, E.G., Lee, J.S., Lee, S., Joo, S., Song, S.H., Kim, E.C., Lee, J.C., et al., 2014. A rapid antimicrobial susceptibility test based on single-cell morphological analysis. Science translational medicine 6, 267ra174–267ra174.

Chollet, F., et al., 2015. Keras: Deep learning library for theano and tensorflow. URL: https://keras. io/k 7, T1.

Cline, A., Jhaveri, R., Levinson, K., Miller, M., 2017. Rapid detection of pediatric bacteriuria using narrow angle forward laser scattering technology (naflst) with bacterioscan, in: Open forum infectious diseases, Oxford University Press. p. S613.

CLSI, 2015a. Clinical and laboratory standards institute (clsi), performance standards for antimicrobial susceptibility testing, clsi supplement m100s.

CLSI, 2015b. Methods for dilution antimicrobial susceptibility tests for bacteria that grow aerobically: approved standard. CLSI 35.

Dalgaard, P., Ross, T., Kamperman, L., Neumeyer, K., McMeekin, T.A., 1994. Estimation of bacterial growth rates from turbidimetric and viable count data. International journal of food microbiology 23, 391–404.

Daniels, R., 2011. Surviving the first hours in sepsis: getting the basics right (an intensivist's perspective). Journal of antimicrobial chemotherapy 66, ii11–ii23.

Dark, P.M., Dean, P., Warhurst, G., 2009. Bench-to-bedside review: the promise of rapid infection diagnosis during sepsis using polymerase chain reaction-based pathogen detection. Critical care 13, 217.

Daugelavičius, R., Bakiene, E., Bamford, D.H., 2000. Stages of polymyxin b interaction with theescherichia coli cell envelope. Antimicrobial agents and chemotherapy 44, 2969–2978.

Davenport, M., Mach, K.E., Shortliffe, L.M.D., Banaei, N., Wang, T.H., Liao, J.C., 2017. New and developing diagnostic technologies for urinary tract infections. Nature Reviews Urology 14, 296.

De Majumdar, S., Veleba, M., Finn, S., Fanning, S., Schneiders, T., 2013. Elucidating the regulon of multidrug resistance regulator rara in klebsiella pneumoniae. Antimicrobial agents and chemotherapy 57, 1603–1609.

Deng, J., Dong, W., Socher, R., Li, L.J., Li, K., Fei-Fei, L., 2009. Imagenet: A large-scale hierarchical image database, in: 2009 IEEE conference on computer vision and pattern recognition, Ieee. pp. 248–255.

Donahue, J., Anne Hendricks, L., Guadarrama, S., Rohrbach, M., Venugopalan, S., Saenko, K., Darrell, T., 2015. Long-term recurrent convolutional networks for visual recognition and description, in: Proceedings of the IEEE conference on computer vision and pattern recognition, pp. 2625–2634.

Drlica, K., Zhao, X., 1997. Dna gyrase, topoisomerase iv, and the 4-quinolones. Microbiology and Molecular Biology Reviews 61, 377–392. URL: https://mmbr.asm.org/content/61/3/377, arXiv:https://mmbr.asm.org/content/61/3/377.full.pdf.

Fernández, L., Álvarez-Ortega, C., Wiegand, I., Olivares, J., Kocíncová, D., Lam, J.S., Martínez, J.L., Hancock, R.E., 2013. Characterization of the polymyxin b resistome of pseudomonas aeruginosa. Antimicrobial agents and chemotherapy 57, 110–119.

Fredborg, M., Andersen, K.R., Jørgensen, E., Droce, A., Olesen, T., Jensen, B.B., Rosenvinge, F.S., Sondergaard, T.E., 2013. Real-time optical antimicrobial susceptibility testing. Journal of clinical microbiology 51, 2047–2053.

Gherardi, G., Angeletti, S., Panitti, M., Pompilio, A., Di Bonaventura, G., Crea, F., Avola, A., Fico, L., Palazzo, C., Sapia, G.F., et al., 2012. Comparative evaluation of the vitek-2 compact and phoenix systems for rapid identification and antibiotic susceptibility testing directly from blood cultures of gram-negative and gram-positive isolates. Diagnostic microbiology and infectious disease 72, 20–31.

Ginalska, G., Osinska, M., Uryniak, A., Urbanik-Sypniewska, T., Belcarz, A., Rzeski, W., Wolski, A., 2005. Antibacterial activity of gentamicin-bonded gelatin-sealed polyethylene terephthalate vascular prostheses. European journal of vascular and endovascular surgery 29, 419–424.

Goodman, L., et al., 2011. Goodman & gilman's the pharmacological basis of therapeutics. 2001. McGraw-Hill Companies, 1687, 1701–1703.

Gregory, K., Mello, C.M., 2005. Immobilization of escherichia coli cells by use of the antimicrobial peptide cecropin p1. Appl. Environ. Microbiol. 71, 1130–1134.

Guan, Y., Shan, X., Wang, S., Zhang, P., Tao, N., 2014. Detection of molecular binding via charge-induced mechanical response of optical fibers. Chemical science 5, 4375–4381.

Hancock, R.E., 2007. The end of an era? Nature Reviews Drug Discovery 6, 28–28.

Hay, E.A., Parthasarathy, R., 2018. Performance of convolutional neural networks for identification of bacteria in 3d microscopy datasets. PLoS computational biology 14, e1006628.

He, K., Zhang, X., Ren, S., Sun, J., 2016. Deep residual learning for image recognition, in: Proceedings of the IEEE conference on computer vision and pattern recognition, pp. 770–778.

He, Y., Xu, W., Zhi, Y., Tyagi, R., Hu, Z., Cao, G., 2018. Rapid bacteria identification using structured illumination microscopy and machine learning. Journal of Innovative Optical Health Sciences 11, 1850007.

Helm, D., Labischinski, H., Schallehn, G., Naumann, D., 1991. Classification and identification of bacteria by fourier-transform infrared spectroscopy. Microbiology 137, 69–79.

Höltje, J.V., 1995. From growth to autolysis: the murein hydrolases inescherichia coli. Archives of microbiology 164, 243–254.

Höltje, J.V., 1998. Growth of the stress-bearing and shape-maintaining murein sacculus of escherichia coli. Microbiol. Mol. Biol. Rev. 62, 181–203.

Iriya, R., Jing, W., Syal, K., Mo, M., Chen, C., Yu, H., Haydel, S.E., Wang, S., Tao, N., 2020. Rapid antibiotic susceptibility testing based on bacterial motion patterns with long short-term memory neural networks. IEEE Sensors Journal .

Iriya, R., Ramírez, M.A., 2014. Gaussian mixture models with class-dependent features for speech emotion recognition, in: 2014 IEEE Workshop on Statistical Signal Processing (SSP), IEEE. pp. 480–483.

Iriya, R., Syal, K., Jing, W., Mo, M., Yu, H., Haydel, S.E., Wang, S., Tao, N., 2017. Real-time detection of antibiotic activity by measuring nanometer-scale bacterial deformation. Journal of biomedical optics 22, 126002.

Jing, W., Jiang, X., Zhao, W., Liu, S., Cheng, X., Sui, G., 2014. Microfluidic platform for direct capture and analysis of airborne mycobacterium tuberculosis. Analytical Chemistry 86, 5815–5821. URL: https://doi.org/10.1021/ac500578h, doi:10.1021/ac500578h, arXiv:https://doi.org/10.1021/ac500578h. pMID: 24857567.

Jing, W., Zhao, W., Liu, S., Li, L., Tsai, C.T., Fan, X., Wu, W., Li, J., Yang, X., Sui, G., 2013. Microfluidic device for efficient airborne bacteria capture and enrichment. Analytical Chemistry 85, 5255–5262. URL: https://doi.org/10.1021/ac400590c, doi:10.1021/ac400590c, arXiv:https://doi.org/10.1021/ac400590c. pMID: 23590462.

Jo, Y., Jung, J., Kim, M.h., Park, H., Kang, S.J., Park, Y., 2015. Label-free identification of individual bacteria using fourier transform light scattering. Optics express 23, 15792–15805.

Karasinski, J., White, L., Zhang, Y., Wang, E., Andreescu, S., Sadik, O.A., Lavine, B.K., Vora, M., 2007. Detection and identification of bacteria using antibiotic susceptibility and a multi-array electrochemical sensor with pattern recognition. Biosensors and Bioelectronics 22, 2643–2649.

King, A., 2001. Recommendations for susceptibility tests on fastidious organisms and those requiring special handling. Journal of Antimicrobial Chemotherapy 48, 77–80.

Kingma, D.P., Ba, J., 2014. Adam: A method for stochastic optimization. arXiv:1412.6980.

Kohanski, M.A., Dwyer, D.J., Wierzbowski, J., Cottarel, G., Collins, J.J., 2008. Mistranslation of membrane proteins and two-component system activation trigger antibiotic-mediated cell death. Cell 135, 679–690.

Krizhevsky, A., Sutskever, I., Hinton, G.E., 2012. Imagenet classification with deep convolutional neural networks, in: Advances in neural information processing systems, pp. 1097–1105.

Krupovič, M., Daugelavičius, R., Bamford, D.H., 2007. Polymyxin b induces lysis of marine pseudoalteromonads. Antimicrobial agents and chemotherapy 51, 3908–3914.

Kshikhundo, R., Itumhelo, S., 2016. Bacterial species identification. World News of Natural Sciences 3, 26–38.

Kumar, V., Minz, S., 2014. Feature selection: A literature review. Smart CR 4, 211–229.

Lazcka, O., Del Campo, F.J., Munoz, F.X., 2007. Pathogen detection: a perspective of traditional methods and biosensors. Biosensors and bioelectronics 22, 1205–1217.

Lee, C.C., Sui, G., Elizarov, A., Shu, C.J., Shin, Y.S., Dooley, A.N., Huang, J., Daridon, A., Wyatt, P., Stout, D., Kolb, H.C., Witte, O.N., Satyamurthy, N., Heath, J.R., Phelps, M.E., Quake, S.R., Tseng, H.R., 2005. Multistep synthesis of a radiolabeled imaging probe using integrated microfluidics. Science 310, 1793–1796.

Liang, Y., Kang, R., Lian, C., Mao, Y., 2018. An end-to-end system for automatic urinary particle recognition with convolutional neural network. Journal of medical systems 42, 165.

Liou, G.F., Yoshizawa, S., Courvalin, P., Galimand, M., 2006. Aminoglycoside resistance by arma-mediated ribosomal 16 s methylation in human bacterial pathogens. Journal of molecular biology 359, 358–364.

Liu, C., Bayer, A., Cosgrove, S.E., Daum, R.S., Fridkin, S.K., Gorwitz, R.J., Kaplan, S.L., Karchmer, A.W., Levine, D.P., Murray, B.E., et al., 2011. Clinical practice guidelines by the infectious diseases society of america for the treatment of

methicillin-resistant staphylococcus aureus infections in adults and children. Clinical infectious diseases 52, e18–e55.

Longo, G., Alonso-Sarduy, L., Rio, L.M., Bizzini, A., Trampuz, A., Notz, J., Dietler, G., Kasas, S., 2013. Rapid detection of bacterial resistance to antibiotics using afm cantilevers as nanomechanical sensors. Nature nanotechnology 8, 522–526.

Lowe, G., 2004. Sift-the scale invariant feature transform. Int. J 2, 91–110.

Maeda, K., Imae, Y., Shioi, J.I., Oosawa, F., 1976. Effect of temperature on motility and chemotaxis of escherichia coli. Journal of Bacteriology 127, 1039–1046. URL: https://jb.asm.org/content/127/3/1039, arXiv:https://jb.asm.org/content/127/3/1039.full.pdf.

Malpica, N., de Solórzano, C.O., Vaquero, J.J., Santos, A., Vallcorba, I., García-Sagredo, J.M., del Pozo, F., 1997. Applying watershed algorithms to the segmentation of clustered nuclei. Cytometry 28, 289–297.

Mendel, J.M., 1995. Lessons in estimation theory for signal processing, communications, and control. Pearson Education.

Mittman, S.A., Huard, R.C., Della-Latta, P., Whittier, S., 2009. Comparison of bd phoenix to vitek 2, microscan microstrep, and etest for antimicrobial susceptibility testing of streptococcus pneumoniae. Journal of clinical microbiology 47, 3557–3561.

Mo, M., Yang, Y., Zhang, F., Jing, W., Iriya, R., Popovich, J., Wang, S., Grys, T., Haydel, S.E., Tao, N., 2019. Rapid antimicrobial susceptibility testing of patient urine samples using large volume free-solution light scattering microscopy. Analytical chemistry 91, 10164–10171.

Mohamad, N.A., Jusoh, N.A., Htike, Z.Z., Win, S.L., et al., 2014. Bacteria identification from microscopic morphology: a survey. International Journal on Soft Computing, Artificial Intelligence and Applications (IJSCAI) 3, 2319–1015.

Muscedere, J., Dodek, P., Keenan, S., Fowler, R., Cook, D., Heyland, D., Committee, V.G., Group, C.C.C.T., et al., 2008. Comprehensive evidence-based clinical practice guidelines for ventilator-associated pneumonia: diagnosis and treatment. Journal of critical care 23, 138–147.

Najar, M., Saldanha, C., Banday, K., et al., 2009. Approach to urinary tract infections. Indian journal of nephrology 19, 129.

Niemz, A., Ferguson, T.M., Boyle, D.S., 2011. Point-of-care nucleic acid testing for infectious diseases. Trends in biotechnology 29, 240–250.

Noyan, T., Gözlükaya, Ö., Ayyildiz, S.N., Çetinkol, Y., Çakir, F.Ö., Çankaya, S., 2014. Are all small particles parameters in the iq200 auto particle recognition software have any benefit on reduce the urine culture number. Journal of Chemistry and Biochemistry 2, 169–77.

Ordóñez, F.J., Roggen, D., 2016. Deep convolutional and lstm recurrent neural networks for multimodal wearable activity recognition. Sensors 16, 115.

Otsu, N., 1979. A threshold selection method from gray-level histograms. IEEE transactions on systems, man, and cybernetics 9, 62–66.

Pottash, A.E., McKay, R., Virgile, C.R., Ueda, H., Bentley, W.E., 2017. Tumblescore: run and tumble analysis for low frame-rate motility videos. Biotechniques 62, 31–36.

Price, C.S., Kon, S.E., Metzger, S., 2014. Rapid antibiotic susceptibility phenotypic characterization of staphylococcus aureus using automated microscopy of small numbers of cells. Journal of microbiological methods 98, 50–58.

Quinn, J.A., Nakasi, R., Mugagga, P.K., Byanyima, P., Lubega, W., Andama, A., 2016. Deep convolutional neural networks for microscopy-based point of care diagnostics, in: Machine Learning for Healthcare Conference, pp. 271–281.

Radon, J., 1986. On the determination of functions from their integral values along certain manifolds. IEEE transactions on medical imaging 5, 170–176.

Reller, L.B., Weinstein, M., Jorgensen, J.H., Ferraro, M.J., 2009. Antimicrobial susceptibility testing: a review of general principles and contemporary practices. Clinical infectious diseases 49, 1749–1755.

Rösch, P., Harz, M., Schmitt, M., Peschke, K.D., Ronneberger, O., Burkhardt, H., Motzkus, H.W., Lankers, M., Hofer, S., Thiele, H., et al., 2005. Chemotaxonomic identification of single bacteria by micro-raman spectroscopy: application to cleanroom-relevant biological contaminations. Appl. Environ. Microbiol. 71, 1626–1637.

Ruder, S., 2016. An overview of gradient descent optimization algorithms. `arXiv:1609.04747`.

Sands, K.E., Bates, D.W., Lanken, P.N., Graman, P.S., Hibberd, P.L., Kahn, K.L., Parsonnet, J., Panzer, R., Orav, E.J., Snydman, D.R., et al., 1997. Epidemiology of sepsis syndrome in 8 academic medical centers. Jama 278, 234–240.

Schoepp, N.G., Schlappi, T.S., Curtis, M.S., Butkovich, S.S., Miller, S., Humphries, R.M., Ismagilov, R.F., 2017. Rapid pathogen-specific phenotypic antibiotic susceptibility testing using digital lamp quantification in clinical samples. Science Translational Medicine 9, eaal3693.

Sharma, D., Cukras, A.R., Rogers, E.J., Southworth, D.R., Green, R., 2007. Mutational analysis of s12 protein and implications for the accuracy of decoding by the ribosome. Journal of molecular biology 374, 1065–1076.

Shayanfar, N., Tobler, U., von Eckardstein, A., Bestmann, L., 2007. Automated urinalysis: first experiences and a comparison between the iris iq200 urine microscopy system, the sysmex uf-100 flow cytometer and manual microscopic particle counting. Clinical Chemical Laboratory Medicine 45, 1251–1256.

Sinn, I., Albertson, T., Kinnunen, P., Breslauer, D.N., McNaughton, B.H., Burns, M.A., Kopelman, R., 2012. Asynchronous magnetic bead rotation microviscometer for rapid, sensitive, and label-free studies of bacterial growth and drug sensitivity. Analytical chemistry 84, 5250–5256.

Sousa, A.M., Machado, I., Nicolau, A., Pereira, M.O., 2013. Improvements on colony morphology identification towards bacterial profiling. Journal of microbiological methods 95, 327–335.

Spratt, B.G., 1975. Distinct penicillin binding proteins involved in the division, elongation, and shape of escherichia coli k12. Proceedings of the National Academy of Sciences 72, 2999–3003.

Syal, K., Iriya, R., Yang, Y., Yu, H., Wang, S., Haydel, S.E., Chen, H.Y., Tao, N., 2016. Antimicrobial susceptibility test with plasmonic imaging and tracking of single bacterial motions on nanometer scale. ACS nano 10, 845–852.

Syal, K., Mo, M., Yu, H., Iriya, R., Jing, W., Guodong, S., Wang, S., Grys, T.E., Haydel, S.E., Tao, N., 2017. Current and emerging techniques for antibiotic susceptibility tests. Theranostics 7, 1795.

Thompson, J., O'Connor, M., Mills, J.A., Dahlberg, A.E., 2002. The protein synthesis inhibitors, oxazolidinones and chloramphenicol, cause extensive translational inaccuracy in vivo. Journal of molecular biology 322, 273–279.

Tinevez, J.Y., Perry, N., Schindelin, J., Hoopes, G.M., Reynolds, G.D., Laplantine, E., Bednarek, S.Y., Shorte, S.L., Eliceiri, K.W., 2017. Trackmate: An open and extensible platform for single-particle tracking. Methods 115, 80–90.

Vaiana, A.C., Sanbonmatsu, K.Y., 2009. Stochastic gating and drug–ribosome interactions. Journal of molecular biology 386, 648–661.

Wang, Y., Huang, M., Zhu, X., Zhao, L., 2016. Attention-based lstm for aspect-level sentiment classification, in: Proceedings of the 2016 conference on empirical methods in natural language processing, pp. 606–615.

Weston, J., Watkins, C., 1998. Multi-class support vector machines. Technical Report. Citeseer.

White, R.L., Burgess, D.S., Manduru, M., Bosso, J.A., 1996. Comparison of three different in vitro methods of detecting synergy: time-kill, checkerboard, and e test. Antimicrobial Agents and Chemotherapy 40, 1914–1918.

Wiegand, I., Hilpert, K., Hancock, R.E., 2008. Agar and broth dilution methods to determine the minimal inhibitory concentration (mic) of antimicrobial substances. Nature protocols 3, 163–175.

Xie, C., Mace, J., Dinno, M., Li, Y., Tang, W., Newton, R., Gemperline, P., 2005. Identification of single bacterial cells in aqueous solution using confocal laser tweezers raman spectroscopy. Analytical chemistry 77, 4390–4397.

Yang, X., Li, H., Zhou, X., 2006. Nuclei segmentation using marker-controlled watershed, tracking using mean-shift, and kalman filter in time-lapse microscopy. IEEE Transactions on Circuits and Systems I: Regular Papers 53, 2405–2414.

Yao, Z., Kahne, D., Kishony, R., 2012. Distinct single-cell morphological dynamics under beta-lactam antibiotics. Molecular cell 48, 705–712.

Yu, H., Jing, W., Iriya, R., Yang, Y., Syal, K., Mo, M., Grys, T.E., Haydel, S.E., Wang, S., Tao, N., 2018. Phenotypic antimicrobial susceptibility testing with deep learning video microscopy. Analytical chemistry 90, 6314–6322.

Zafari, S., Eerola, T., Sampo, J., Kälviäinen, H., Haario, H., 2015. Segmentation of overlapping elliptical objects in silhouette images. IEEE Transactions on Image Processing 24, 5942–5952.

Zaremba, W., Sutskever, I., Vinyals, O., 2014. Recurrent neural network regularization. arXiv preprint arXiv:1409.2329 .

Zeng, S., Zhang, B., Zhang, Y., Gou, J., 2018. Collaboratively weighting deep and classic representation via l2 regularization for image classification. arXiv:1802.07589.

Zeni, F., Freeman, B., Natanson, C., 1997. Anti-inflammatory therapies to treat sepsis and septic shock: a reassessment. Critical care medicine 25, 1095–1100.

Zhang, C., Chen, W., Liu, W., Chen, C., 2008. An automated bacterial colony counting system, in: 2008 IEEE International Conference on Sensor Networks, Ubiquitous, and Trustworthy Computing (sutc 2008), pp. 233–240.

Zimmermann, M., Escrig, S., Hübschmann, T., Kirf, M.K., Brand, A., Inglis, R.F., Musat, N., Müller, S., Meibom, A., Ackermann, M., et al., 2015. Phenotypic heterogeneity in metabolic traits among single cells of a rare bacterial species in its natural environment quantified with a combination of flow cell sorting and nanosims. Frontiers in microbiology 6, 243.

APPENDIX A

STATISTICAL ANALYSIS OF PMB RESULTS FOR THE BACTERIAL MEMBRANE MORPHOLOGICAL DEFORMATIONS ASSESSMENT

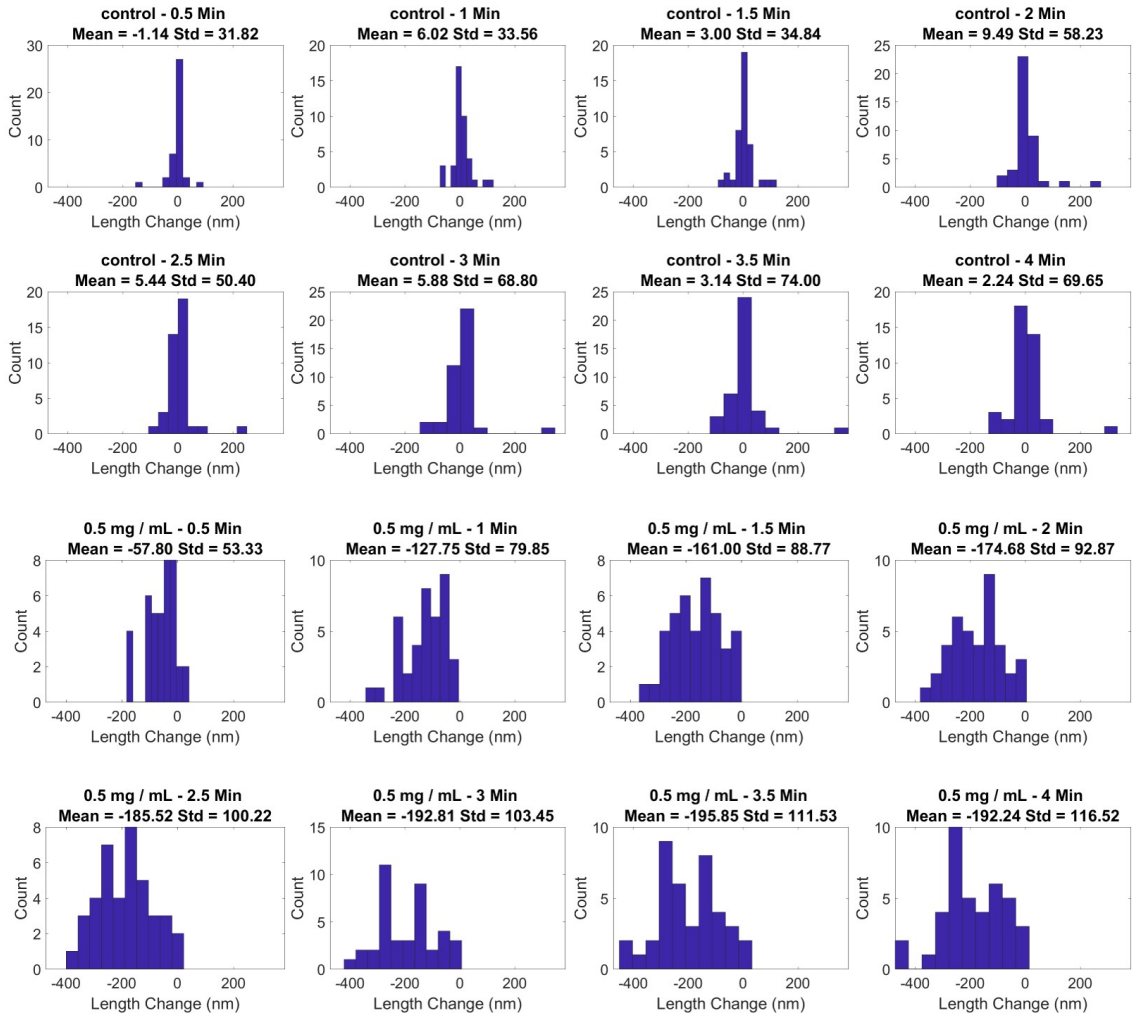


Figure A.1: Histogram Analyses of Length Changes for 40 Cells in PBS Control (a) and PMB (b) Experiments at Different Time Points (After Introduction of Antibiotics for PMB Plots). After Antibiotic Addition, Cell Shrinkage Increased over Time. Comparison of Average Values Between the Control and Antibiotic Experiments for All Time Points Revealed Statistically Significant Differences ($\rho = 3.43 \times 10^{-8}$; Student T-Test). Source - (Iriya et al. (2017))

This appendix shows the statistical analysis of PMB results from the Bacterial membrane morphological deformations assessment. Figs. A.1 and A.2 show histograms comparing the distribution of membrane deformation changes between the control group and the antibiotic affected group, for length and width, respectively. Length histograms show a statistically significant difference between the two groups when performing a student t-test with $\rho = 3.43 \times 10^{-8}$, as we observe a drastic shift of the mean towards negative values. Width results show no statistically significant difference between the two groups when performing a student t-test with $\rho = 0.75$.

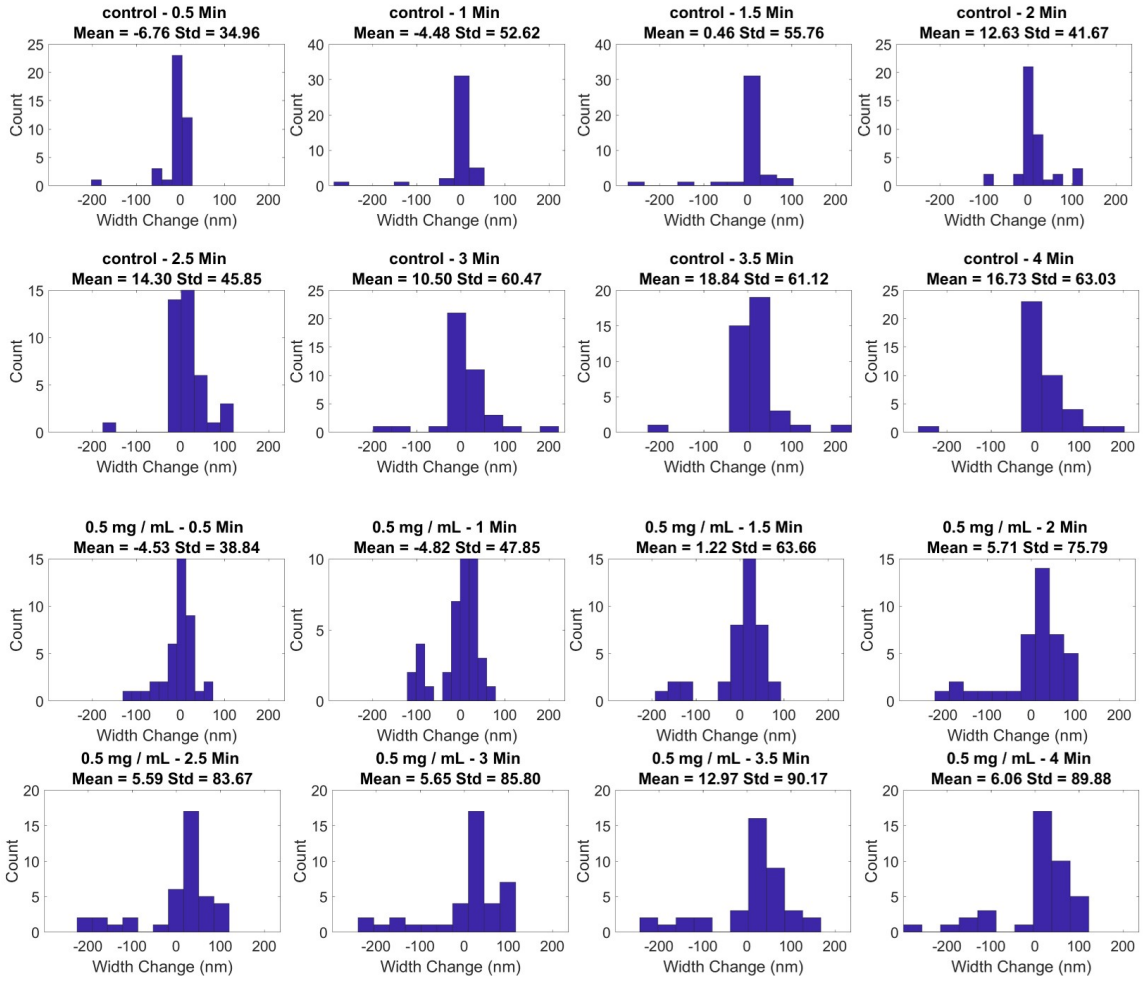


Figure A.2: Histogram Analyses of Width Changes for 40 cells in PBS Control (a) and PMB (b) Experiments at Different Time Points (After Introduction of Antibiotics for PMB Plots). After Antibiotic Addition, Cell Width Did Not Significantly Change over Time. Comparison of Average Values Between the Control and Antibiotic Experiments for All Time Points Revealed no Statistical Differences ($\rho = 0.75$; Student T-Test). Source - (Iriya et al. (2017))

APPENDIX B

PERMISSION TO USE PREVIOUSLY PUBLISHED CONTENT

All co-authors from publications (Iriya et al. (2017)) and (Iriya et al. (2020)) have granted their permissions to include those studies in this work.

BIOGRAPHICAL SKETCH



Rafael Iriya was born in São Paulo, Brazil in July 19, 1987. He received his B.S. degree in electrical engineering in 2009 and his M.S. degree in electrical engineering in 2014, both from University of São Paulo. Coming from a signal processing and machine learning background, his researched focused on speech processing applications including speaker recognition, gender identification and emotion recognition. In 2014, he joined the Biodesign Center for Biosensors and Bioelectronics at Arizona State University, where he worked as a research assistant while pursuing a PhD in Electrical engineering, with a research on computer vision applied to bacterial identification and susceptibility assessment. His current research interest is focused on deep learning algorithms for computer vision, computational photography and general software development.